IOWA STATE UNIVERSITY
Digital Repository

2020

Relativistic bound states on the light front

Shuo Tang
Iowa State University

www.manaraa.com

Relativistic bound states on the light front

by

Shuo Tang

A dissertation submitted to the graduate faculty

in partial fulfillment of the requirements for the degree of

DOCTOR OF PHILOSOPHY

Major: Nuclear Physics

Program of Study Committee:
James P. Vary, Major Professor
Pieter Maris
John Lajoie
Amanda Weinstein
Glenn Luecke

The student author, whose presentation of the scholarship herein was approved by the program of study committee, is solely responsible for the content of this dissertation. The Graduate College will ensure this dissertation is globally accessible and will not permit alterations after a degree is conferred.

Iowa State University

Ames, Iowa

2020

DEDICATION

This dissertation is dedicated to my parents.

TABLE OF CONTENTS

ACKNOWLEDGMENTS

I would like to extend my deep gratitude to all those who have offered me a lot of help and support in the process of my thesis writing.

My special acknowledgment is given to my respectable advisor, Prof. James P. Vary,. whose patient instruction and constructive suggestions are beneficial to me a lot. He encouraged me profoundly throughout my graduate study. I also wish to thank Prof. Pieter Maris. I can always obtain great insights in each of the discussion with him. I would like to thank Dr. Yang Li, whose passion for physics encouraged me all the time. Without their consistent and illuminating instructions, this thesis could not have reached its present form.

I would like to express my appreciations to other committee members Prof. John Lajoie, Prof. Amanda Weinstein, Prof. Gelnn Luecke.

Dr. Shaoyang Jia and Dr. Meijian Li are wonderful colleagues and friends, the office becomes energetic with their presence.

Finally, I would like to thank all those who helped me along the way of my graduate study in Iowa State University.

ABSTRACT

We develop and apply a relativistic and non-perturbative approach to bound states and their properties on the light front in Quantum Chromodynamics (QCD). We investigate a Hamiltonian, derived in part from QCD, which features strongly interacting and confined quarks and apply it to heavy flavored mesons. This effective Hamiltonian is developed based on the light-front holographic QCD and an effective one-gluon-exchange interaction. We solve for the mass eigenstates and light-front wave functions (LFWFs) of this effective Hamiltonian using basis light-front quantization (BLFQ). This effective Hamiltonian was first implemented in the heavy quarkonium system where it provided a successful description of the mass spectrum and other physical observables. In this thesis, we will show that, with the least parameter fitting, we can also produce reasonable results for the unequal-mass heavy flavored mesons: B_c, B, B_s, D, and D_s. In particular, we calculated the mass spectra and corresponding light-front wave functions, illustrate their asymmetric features and employ them to calculate properties of experimental interest such as parton distribution amplitudes and functions.

We further investigate the semileptonic decays of B_c to charmonium. Since the gauge boson involved in the semileptonic decay needs to be in the timelike region, the conventional choice of frame, the Drell-Yan frame, is not suitable for these decays. Instead we adopt a general frame to tackle the kinematics. Due to the complex structure of the hadron current matrix that governs these decays, we employ more than one current component and LFWFs at different magnetic projections. There we also show the frame dependence that is due to the Fock sector truncation, that is our limited treatment of the mesons as quark - antiquark bound states omitting other possible contributions such as gluon excitations. We also report the dependence of calculated observables on parameters of the basis space, which we show how to minimize.

As a further application of this approach, we apply it to the physical electron system in Quantum Electrodynamics (QED), which is treated as a relativistic electron which can emit and absorb a photon on the light front. We calculate the electromagnetic form factors and gravitational form factors of an electron, and compare our results with the light-front perturbation theory. This work provides insights into the challenges and promise of applying this light-front Hamiltonian approach to more complete treatments of QCD in the future.

CHAPTER 1.   QUANTUM FIELD THEORY ON THE LIGHT FRONT

1.1   Quantum Field Theory

Quantum field theory (QFT) is a basic mathematical framework to describe elementary particles. It unites the theory of quantum mechanics with Einstein's special relativity, and serves as the bedrock of modern physics. So far in the history of science, QFT has led to the most reliable agreement between theoretical predictions and experiment, such as the prediction and observation of the Higgs boson [1, 2]. Therefore it provides us with profound insights into the nature of our universe.

Since QFT is the result of combining quantum mechanics with special relativity, the relativistic space-time symmetries, known as Lorentz invariance, emerge. Mathematically, a system is Lorentz invariant if it is symmetric under the Lorentz group of transformations. A Lorentz transformation on a 4-vector $x^\mu = (x^0, x^1, x^2, x^3)$[1] is characterized by,

$$x'^\mu = \Lambda^\mu_\nu x^\nu, \tag{1.1}$$

where repeated indices imply summation, Λ^μ_ν denotes the Lorentz transformation matrix. Λ^μ_ν preserves a metric tensor $g_{\mu\nu}$ in the sense that

$$\Lambda^\mu_\sigma \Lambda^\nu_\rho g_{\mu\nu} = g_{\sigma\rho}, \tag{1.2}$$

where we can adopt the Minkowski metric for this 4-vector in time (x^0) and space (3 additional dimensions), $g_{\mu\nu} = \text{diag}(-1, 1, 1, 1)$. Note that $x_\mu = g_{\mu\nu} x^\nu, x^\mu = g^{\mu\nu} x_\nu$, and $x^2 = x_\mu x^\mu$. The Lorentz group has six generators, three of which describe the rotations, while the other three describe the boosts, the transformations that change the velocity. They correspond to the rotation generators J_i and boost generators K_i with $i = 1, 2, 3$, respectively. A general Lorentz transformation can be

---

[1]Note that we adopt the natural units $\hbar = c = 1$ for this thesis unless otherwise state, as it gives all quantities dimensions of energy to some power.

written uniquely in terms of a linear combination of generators as,

$$\Lambda = \exp\left(-\mathrm{i}\vec{J}\cdot\vec{\theta} - \mathrm{i}\vec{K}\cdot\vec{\eta}\right), \tag{1.3}$$

where $\vec{\theta}$ and $\vec{\eta}$ encode the freely chosen parameters, the rotation angles and the boost magnitudes in each direction. In order to have a more compact form for the Lie algebra and to add space-time translations into the discussion, we introduce an antisymmetric tensor $M^{\mu\nu}$ ($\mu,\nu = 0,1,2,3$), such that

$$J_i = \frac{1}{2}\epsilon_{ijk}M^{jk}, \qquad K_i = M^{0i}, \tag{1.4}$$

with ϵ_{ijk} being the Levi-Civita symbol. We can then introduce four generators P^μ in charge of translation, which together with $M^{\mu\nu}$, compose the Poincaré group, which underlines all symmetries in the Minkowski space. Combining all ten generators gives the Lie algebra of the Poincaré group where

$$\begin{aligned}
[P^\mu, P^\nu] &= 0, \\
[P^\rho, M^{\mu\nu}] &= \mathrm{i}(g^{\rho\mu}P^\nu - g^{\rho\nu}P^\mu), \\
[M^{\mu\nu}, M^{\rho\sigma}] &= \mathrm{i}(g^{\mu\sigma}M^{\nu\rho} - g^{\nu\sigma}M^{\mu\rho} + g^{\nu\rho}M^{\mu\sigma} - g^{\mu\rho}M^{\nu\sigma}).
\end{aligned} \tag{1.5}$$

One of the take-home messages from special relativity is that the contractions such as $p^2 \equiv p^\mu p_\mu$ are "Lorentz scalars" and can correspond to physical observables which are Lorentz invariant.

One of those important Lorentz scalars we investigate is the Lagrangian density $\mathcal{L}$, which we will refer to as the "Lagrangian". In principal, using the Lagrangian, one can determine the S-matrix of scattering that encodes information of the interacting physics through the Lehmann-Symanzik-Zimmermann (LSZ) reduction formula [3]. For instance, the Lagrangian of quantum electrodynamics (QED) is relatively simple due to the fact that the gauge symmetry is governed by the group U(1). In addition, the coupling strength of the electromagnetic field has a value much less than 1 which means that the perturbation approach is applicable.

However quantum chromodynamics (QCD) is a more challenging topic. It is a theory of the strong interaction between quarks and gluons with the SU(3) symmetry group for an internal degree of freedom called "color". The detailed form of the QCD Lagrangian including color results in a

theory which is non-Abelian in character giving rise to, among other phenomena, confinement and asymptotic freedom. The confinement phenomena, which is consistent with experimental evidence but not rigorously proven, means that nature allows only color-singlet composite states made up of quarks and gluons, i.e. quarks and gluons, which carry color, cannot be experimentally isolated. The property of asymptotic freedom is a proven property and consistent with experiments. It states that, although the coupling between quark and gluon is strong and non-perturbative in the low energy region, it becomes perturbative at high energies due to a derivable property called "running coupling".

Overall, QCD is widely believed to be a correct theory but it is not known how to solve QCD for all possible experimental applications. In particular, the domain where it requires non-perturbative approaches is under rapid and intensive development. This thesis adopts and applies a candidate nonperturbative approach, Basis Light-Front Quantization (BLFQ) and derives experimentally relevant results for a number of applications. Before progressing to the specific approach applied in this work, I will mention some other nonperturbative theories.

Lattice QCD   Lattice QCD is a well-established nonperturbative approach to study the interaction between quarks and gluons [4]. It is a gauge field theory formulated based on grids (lattice points) in space-time, that the fields representing the quark and the antiquark are defined at lattice sites, while the fields of the gauge boson are defined on the links that connect neighboring sites. Therefore the analytical path integrals of the theory can be traced through numerical computation. This approximation approaches continuum QCD as the spacing between lattice sites is reduced to zero and the number of lattice sites approaches infinity in each space-time dimension. However the computational cost of numerical simulations can increase dramatically as one attempts to approach the continuum limit. To reduce the computational burden, the "quenched approximation" was often adopted in earlier days, where the fermion fields are treated as non-dynamical variables. As the computational power is sufficient today, the "unquenched" Lattice QCD is now the standard. However the intensive computation cost is still the bottleneck of this approach. Note that the lattice QCD theory is set up in the Euclidean time (imaginary time). Currently, there is no for-

mulation allowing one to simulate the real-time dynamics of a quark-gluon system on a Minkowski space-time lattice.

Dyson-Schwinger and Bethe-Salpeter Equations   Dyson-Schwinger equation (DSE) is an *ab initio* approach based on the Lagrangian formalism in Euclidean space-time [5, 6]. DSEs are coupled integral equations for the Greens functions (i.e. n-point functions) of the theory, while bound states appear as poles in the Greens functions. Therefore the field theory is completely defined when all of its n-point Greens functions are known. One example of DSEs is the Bethe-Salpeter equation (BSE), which is the two-particle (4-point) Dyson equation. BSEs describe the bound states of a two-body system in fully covariant relativistic formalism.

Effective theories   Effective theories are designed for specific problems and can give qualitatively correct results in certain limits. One well-known example is the chiral perturbation theory [7], which is an effective theory constructed with a Lagrangian consistent with the (approximate) chiral symmetry of QCD, as well as other symmetries such as parity and charge conjugation. Chiral perturbation theory is particularly useful to describe the light hadron systems such as pions, kaons, and nucleons, since it assumes chiral symmetry, therefore (quasi-) massless quarks. Another example is the heavy quark effective theory (HQET) [8]. As suggested by the name, HQET works for the systems containing a heavy quark, such as the B meson or the Ξ_c baryon, and it is the limit of QCD with the quark mass taken to infinity while its 4-velocity is fixed. One challenge for effective theories arises from the feature that the effective Lagrangian contains, in principle, an infinite number of terms. To achieve practical applications, a method to achieve a hierarchy of terms is introduced and that choice is not unique.

QCD sum rules   Instead of a model-dependent treatment in terms of constituent quarks, hadrons are represented by their interpolating quark currents in the QCD sum rules approach [9]. It employs the operator product expansion for the correlation functions of two or more quark currents, so that the short and long-distance quark-gluon interactions are separated. The former are

calculated using QCD perturbation theory, whereas the latter are parameterized in terms of universal vacuum condensates or light-cone distribution amplitudes. The result of this QCD calculation is then matched, via dispersion relation, to a sum over hadronic states. The sum rule obtained in this way allows one to calculate observable characteristics of the hadronic ground state but does require any experimental input to fix constants that are not yet derivable from QCD.

1.2 Light-Front Quantization

The light-front quantization of quantum field theory has emerged as one of the promising methods for bound-state problems since it has various unique features which makes it appealing. Reviews presented in Refs. [10, 11] indicate why the light-front quantum field theory is a natural framework for tackling relativistic bound-state problems. We will address this problem in the following sections.

1.2.1 Lorentz Symmetry

According to P. A. Dirac [12], there are three fundamental parameterizations of space-time that differ by the hyperspheres on which the fields are initialized. Specifically, they are:

- *Instant form.* This form is the most familiar one, whose hypersphere is give by ordinary time $t = 0$. The generalized coordinates are usually denoted as $x^\mu = (t, x, y, z)$.

- *Front form.* The hypersphere is a tangent plane of the light cone. Therefore the coordinates take the form $x^\mu = (x^+, x^1, x^2, x^-) = (x^0 + x^3, x^1, x^2, x^0 - x^3) = (t + z, x, y, t - z)$.

- *Point form.* The time-like coordinate in the point form is identified with the eigentime of a physical system, and the hypersphere is a hyperboloid shape. That is, we choose the generalized coordinates as $x^\mu = (\tau, \omega, \theta, \phi)$, hence they are associated the coordinates in the

instant form by

$$
\begin{pmatrix} t \\ x \\ y \\ z \end{pmatrix} = \begin{pmatrix} \tau \cosh \omega \\ \tau \sinh \omega \sin \theta \cos \phi \\ \tau \sinh \omega \sin \theta \sin \phi \\ \tau \sinh \omega \cos \theta \end{pmatrix}. \tag{1.6}
$$

We present the three parameterization forms in Table 1.1 with some of their features. Notice that the front form is favored for having four kinematic components of $M^{\mu\nu}$ while only two dynamical components. Here $J^3 \equiv M^{12}$ rotates the system in the transverse plane (x-y plane) and $K^3 \equiv M^{+-}$ boosts it in the longitudinal direction. Thus there are seven commuting operators in the front form, which are M^{+-}, $M^{+\perp}$, and all P^μ. Note that the "$\perp$" symbol represents the 2-vector in the transverse (x, y)-plane. The other two dynamical operators $M^{\perp -}$ commute with each other, as well as with the relativistic invariant mass $M^2 = P^\mu P_\mu$ [12–14].

Thus one can define the "light-cone (LC) Hamiltonian" as

$$
H_{\mathrm{LC}} = P^\mu P_\mu = P^+ P^- - \boldsymbol{P}_\perp^2, \tag{1.7}
$$

whose eigenvalues correspond to the invariant masses squared of the physical system. The eigenvalues of H_{LC} are boost invariant since the boost operators K^3 and $M^{+\perp}$ are kinematical. Therefore one can always boost the system to an "intrinsic frame" in which the total transverse momentum vanishes, and $H_{\mathrm{LC}} = P^- P^+$. In such a frame the numerical work can be reduced considerably. Some light-cone quantities are manifestly invariant or have simple scaling properties under certain Lorentz transformations [10]:
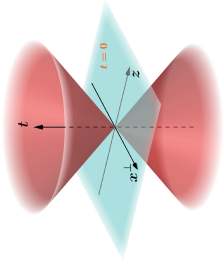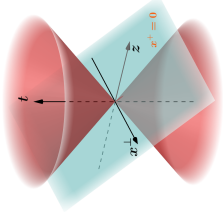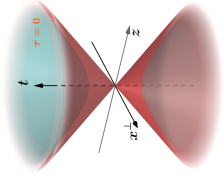
- boost along the longitudinal direction:

$$
p^+ \to C_\| p^+, \qquad \boldsymbol{p}_\perp \to \boldsymbol{p}_\perp, \qquad \boldsymbol{p}_\perp p^- \to C_\|^{-1} p^-; \tag{1.8}
$$

- transverse boost:

$$
p^+ \to p^+, \qquad \boldsymbol{p}_\perp \to \boldsymbol{p}_\perp + p^+ \boldsymbol{C}_\perp, \qquad p^- \to p^- + 2\boldsymbol{p} \cdot \boldsymbol{C}_\perp + p^+ \boldsymbol{C}_\perp^2; \tag{1.9}
$$

Table 1.1: Forms of relativistic dynamics.

	instant form	front form	point form
quantized surface	$t = 0$	$x^+ = t + z = 0$	$x^\mu x_\mu = \tau^2$
metric tensor	$g_{\mu\nu} = \begin{pmatrix} 1 & 0 & 0 & 0 \\ 0 & -1 & 0 & 0 \\ 0 & 0 & -1 & 0 \\ 0 & 0 & 0 & -1 \end{pmatrix}$	$g_{\mu\nu} = \begin{pmatrix} 0 & 0 & 0 & \frac{1}{2} \\ 0 & -1 & 0 & 0 \\ 0 & 0 & -1 & 0 \\ \frac{1}{2} & 0 & 0 & 0 \end{pmatrix}$	$g_{\mu\nu} = \begin{pmatrix} 1 & 0 & 0 & 0 \\ 0 & -\tau^2 & 0 & 0 \\ 0 & 0 & -\tau^2\sinh^2\omega & 0 \\ 0 & 0 & 0 & -\tau^2\sinh^2\omega\sin^2\theta \end{pmatrix}$
kinematic	$\boldsymbol{P},\,\boldsymbol{J}$ (6)	$\boldsymbol{P}^\perp,\,P^+,\,J^3,\,K^3,\,\boldsymbol{M}^{+\perp}$ (7)	$M^{\mu\nu}$ (6)
dynamical	$P^0,\,\boldsymbol{K}$ (4)	$P^-,\,\boldsymbol{M}^{\perp-}$ (3)	P^μ (4)

- rotations in the x-y plane:

$$p^+ \to p^+, \qquad \boldsymbol{p}_\perp^2 \to \boldsymbol{p}_\perp^2. \tag{1.10}$$

These relations are valid for every single particle with momentum p^μ and any longitudinal factor $C_\parallel$ and transverse factor $\boldsymbol{C}_\perp$.

Note that Dirac's three fundamental ways of parameterization cannot be mapped on to one another by any Lorentz transformation. Choosing a certain form is usually based on practical considerations since the physical results should be independent of the parameterization of space-time. The instant form has been studied most extensively, while the front form is the primary focus in this thesis.

1.2.2 Quantum Chromodynamics on the Light Front

The gauge invariant Lagrangian density for QCD is given by [3]

$$\mathcal{L} = -\frac{1}{4}F_a^{\mu\nu}F_{\mu\nu}^a + \overline{\psi}(\mathrm{i}\gamma^\mu D_\mu - m)\psi,^2 \tag{1.11}$$

where $a = 1, 2, .., 8$ stands for the color index. $F_a^{\mu\nu} \equiv \partial^\mu A_a^\nu - \partial^\nu A_a^\mu - g f_{abc} A^{\mu b} A^{\nu c}$ is antisymmetric in the Lorentz indices, with f_{abc} being the structure constant of the SU(3) Lie algebra, and g being the strong interaction constant. $D_\mu \equiv \partial_\mu - \mathrm{i}g A_a^\mu T^a$ is the covariant derivative matrix, where T^a are the color generators whose widely-adopted representation is the Gell-Mann matrices. ψ and A are fields that describe the fermion (quark) and boson (gluon) degrees of freedom, respectively.

In principal, the action and Hamiltonian forms of dynamics are equivalent to each other. The action approach is more suitable for using perturbation theory to derive cross sections, while the Hamiltonian is more convenient in calculating the structure of bound states in atoms, nuclei, and hadrons. The problem of computing spectra and the corresponding wave functions can be reduced to diagonalizing the light-cone Hamiltonian, since a bound state mass M satisfies the eigenvalue equation $H_{\mathrm{LC}}|\Psi\rangle = M^2|\Psi\rangle$.

---

[2]Quark flavor indices have been suppressed for simplicity.

In order to obtain the Hamiltonian, we first derive the canonical momenta $\Pi_i(x)$ in analogy with to the equal-time quantization:

$$\Pi_i(x) \equiv \frac{\delta L}{\delta \partial_+ \Psi^i(x)}, \qquad \partial_+ \Pi_i(x) \equiv \frac{\delta L}{\delta \Psi^i(x)} \tag{1.12}$$

where $\Psi^i(x)$ is a generalized coordinate (represents any of the fields), $\partial_+ \equiv \partial/\partial x^+$, $\delta/\delta f$ represents the functional derivative with respect to a spatial function f, and L is the Lagrangian obtained by integrating the density

$$L(x^+) = \int \mathrm{d}^4 y \delta(x^+ - y^+) \mathcal{L} \left(\Psi^i(y), \partial_+ \Psi^i(y) \right). \tag{1.13}$$

Then the Hamiltonian can be derived from the Legendre transformation,

$$P^-(x^+) = 2 \sum_i \int \mathrm{d}^4 y \delta(x^+ - y^+) \left[\Pi_i(y) \partial_+ \Psi^i(y) - \mathcal{L} \left(\Psi^i(y), \partial_+ \Psi^i(y) \right) \right]. \tag{1.14}$$

Since QED is simpler than QCD, several efforts have used it to test the feasibility of the light-front framework and have made important progress [10, 15–17]. To tackle a QED system, one first needs to write down the light-front Hamiltonian. Since fields that are related by gauge transformations represent the same physical degrees of freedom, one selects a certain gauge to remove that redundancy. In light-front quantization, the preferred choice is the light-cone gauge, i.e. $A^+ \equiv A^0 + A^3 = 0$ [18]. With the light-cone gauge, the QED light-front Hamiltonian is given by

$$\begin{aligned}
P^-_{\mathrm{LFQED}} = \int \mathrm{d}x^- \mathrm{d}x^\perp \Big[&\frac{1}{2} \overline{\psi} \gamma^+ \frac{(\mathrm{i}\partial^\perp)^2 + m^2}{\mathrm{i}\partial^+} \psi - \frac{1}{2} A^i (\mathrm{i}\partial^\perp)^2 A^i + \\
&+ e\overline{\psi} \gamma_\mu A^\mu \psi + \frac{e^2}{2} \overline{\psi} \gamma_\mu A^\mu \frac{\gamma^+}{\mathrm{i}\partial^+} \left(\gamma_\nu A^\nu \psi \right) + \frac{e^2}{2} \overline{\psi} \gamma^+ \psi \frac{1}{(\mathrm{i}\partial^+)^2} \left(\overline{\psi} \gamma^+ \psi \right) \Big],
\end{aligned} \tag{1.15}$$

where $\gamma^+ = \gamma^0 + \gamma^3$. The first two terms stand for the kinetic energies for the electron and photon fields, respectively, while the following terms encode the interactions, which are illustrated with vertex diagrams in Fig. 1.1.
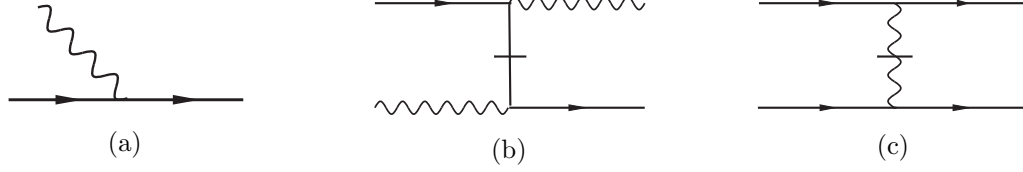
Figure 1.1: Vertex diagrams for the interactions terms in the light-front QED Hamiltonian (1.15). Solid lines represent the fermions, wavy lines represent the photons, and the lines with a bar across denote the instantaneous operators $\frac{1}{\mathrm{i}\partial^+}$ and $\frac{1}{(\mathrm{i}\partial^+)^2}$. Diagrams (a) $-$ (c) correspond to the interaction terms in Eq. (1.15) listed in order.

Our ultimate purpose is to solve bound-state QCD problems. The light-front Hamiltonian of QCD with the corresponding light-cone gauge can be expressed as

$$
\begin{aligned}
P_{\mathrm{LFQCD}}^+ = \int \mathrm{d}x^- \mathrm{d}^2 x^\perp \Big[& \frac{1}{2}\overline{\psi}\gamma^+ \frac{(\mathrm{i}\partial^\perp)^2 + m^2}{\mathrm{i}\partial^+}\psi - \frac{1}{2}A_a^i (\mathrm{i}\partial^\perp)^2 A_a^i \\
& + g\overline{\psi}\gamma_\mu A_a^\mu T^a \psi + \frac{g^2}{2}\overline{\psi}\gamma_\mu A_a^\mu T^a \frac{\gamma^+}{\mathrm{i}\partial^\perp}\left(\gamma_\nu A_b^\nu T^b \psi\right) \\
& - \mathrm{i}g^2 f^{abc}\overline{\psi}\gamma^+ T^c \psi \frac{1}{(\mathrm{i}\partial^+)^2}\left(\mathrm{i}\partial^+ A_a^\mu A_{\mu b}\right) \\
& + \frac{g^2}{2}\overline{\psi}\gamma^+ T^a \psi \frac{1}{(\mathrm{i}\partial^+)^2}\left(\overline{\psi}\gamma^+ T^a \psi\right) + \mathrm{i}g f^{abc}\mathrm{i}\partial^\mu A_a^\nu A_{\mu b}A_{\nu c} \\
& - \frac{g^2}{2}f^{abc}f^{ade}\mathrm{i}\partial^+ A_b^\mu A_{\mu c}\frac{1}{(\mathrm{i}\partial^+)^2}\left(\mathrm{i}\partial^+ A_d^\nu A_{\nu e}\right) + \frac{g^2}{4}f^{abc}f^{ade} A_b^\mu A_c^\nu A_{\mu d}A_{\nu e}\Big].
\end{aligned}
\tag{1.16}
$$

Here the quantized fields of the fermion and boson admit a free field expansion at $x^+ = 0$ [10]:

$$
\begin{aligned}
\psi(x) &= \sum_{s=\pm\frac{1}{2}}\int \frac{\mathrm{d}p^\perp \mathrm{d}p^+}{(2\pi)^3 2p^+}\left(b_s(p)u_s(\boldsymbol{p})\mathrm{e}^{-\mathrm{i}\boldsymbol{p}\cdot\boldsymbol{x}} + d_s^\dagger(p)v_s(\boldsymbol{p})\mathrm{e}^{\mathrm{i}\boldsymbol{p}\cdot\boldsymbol{x}}\right), \\
A_\mu(x) &= \sum_{\lambda=\pm}\int \frac{\mathrm{d}k^\perp \mathrm{d}k^+}{(2\pi)^3 2k^+}\left(a_\lambda(k)\varepsilon_\lambda^\mu(\boldsymbol{k})\mathrm{e}^{-\mathrm{i}\boldsymbol{k}\cdot\boldsymbol{x}} + a_\lambda^\dagger(k)\varepsilon_\lambda^{\mu*}(\boldsymbol{k})\mathrm{e}^{\mathrm{i}\boldsymbol{k}\cdot\boldsymbol{x}}\right).
\end{aligned}
\tag{1.17}
$$

The creation and annihilation operators $a_\lambda^{(\dagger)}$, $b_s^{(\dagger)}$, and $d_s^{(\dagger)}$ satisfy the following canonical commutation relation for bosons and canonical anticommutation relation for fermions:

$$
\begin{aligned}
[a_\lambda(\boldsymbol{k}), a_{\lambda'}^\dagger(\boldsymbol{k})] &= 2k^+ (2\pi)^3 \delta^3(\boldsymbol{k} - \boldsymbol{k}')\delta_{\lambda\lambda'}, \\
\{b_s(\boldsymbol{p}), b_{s'}^\dagger(\boldsymbol{p})\} &= \{d_s(\boldsymbol{p}), d_{s'}^\dagger(\boldsymbol{p})\} = 2p^+ (2\pi)^3 \delta^3(\boldsymbol{p} - \boldsymbol{p}')\delta_{ss'},
\end{aligned}
\tag{1.18}
$$

where $\delta^3(\boldsymbol{k}) \equiv \delta^2(\boldsymbol{k}^\perp)\delta(k^+)$. u and v are the covariant spinors which are normalized according to

$$
\sum_{s=\pm\frac{1}{2}} u_s(\boldsymbol{p})\bar{u}_s(\boldsymbol{p}) = \not{p} + m, \qquad \sum_{s=\pm\frac{1}{2}} v_s(\boldsymbol{p})\bar{v}_s(\boldsymbol{p}) = \not{p} - m,
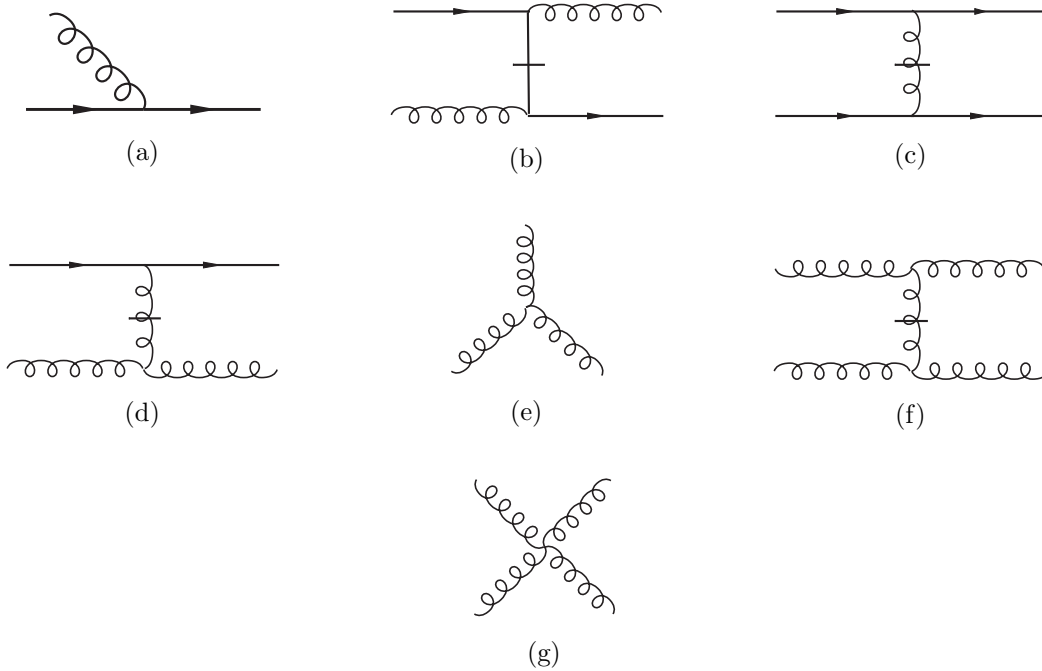\tag{1.19}
$$

Figure 1.2: Vertex diagrams for the interactions terms in the light-front QCD Hamiltonian. Solid lines represent the fermions, curly lines represent the photons, and the lines with a bar across denote the instantaneous operators $\frac{1}{i\partial^+}$ and $\frac{1}{(i\partial^+)^2}$. Diagrams (a) $-$ (g) correspond to the interaction terms in Eq. (1.16) listed in order.

The definitions of u and v and other conventions are listed in Appendix A.2 in detail. ε_λ^μ is the polarization vector that is normalized as (See Appendix A.3)

$$\varepsilon_\lambda^\mu(\boldsymbol{k})\varepsilon_{\lambda'\mu}^*(\boldsymbol{k}) = -\delta_{\lambda\lambda'}. \tag{1.20}$$

1.3   Fock Space Representation

The physical state $|\Psi_h(P,j,m_j)\rangle$ of the hadron h can be expanded in the Fock space as,

$$|\Psi_h(P,j,m_j)\rangle = \sum_{n=0}^\infty \prod_{i=1}^n \sum_{\lambda_i} \int \frac{\mathrm{d}p_i^+ \mathrm{d}^2 p_i^\perp}{2p_i^+(2\pi)^3} 2P^+(2\pi)^3 \delta^3(p_1 + p_2 + ... + p_n - P)$$
$$\times \psi_{h/n}(p_1,\lambda_1,p_2,\lambda_2,...p_n,\lambda_n;P,j,m_j) \times c_{\lambda_1}^\dagger(p_1)...c_{\lambda_n}^\dagger(p_n)|0\rangle \tag{1.21}$$

where $\psi_{h/n}(n=1,2,3,...)$ is the amplitude of the expansion for the n-particle Fock sector, also known as the light-front wave function (LFWF) for the specified Fock space component. $c_{\lambda_i}^\dagger(p_i)$ is the creation operator for the constituent particle, representing the appropriate quark, antiquark, or gluon, with momentum p_i and spin projection λ_i. It should be emphasized that all Fock space particles are on their mass shell, i.e. $p_i^2 = m_i^2$, and the momentum conservation across any vertex does not include energy conservation. Normalization of the LFWFs is

$$\sum_n \prod_i \sum_{\lambda_i} \int \frac{\mathrm{d}p_i^+ \mathrm{d}^2 p_i^\perp}{2p_i^+(2\pi)^3} 2P^+(2\pi)^3 \delta^3(p_1 + p_2 + ... + p_n - P)|\psi_n(p_1,\lambda_1,p_2,\lambda_2,...p_n,\lambda_n;P,\lambda)|^2 = 1. \tag{1.22}$$

This also indicates the normalization of the state vector:

$$\langle\Psi_h(P',j',m_j')|\Psi_h(P,j,m_j)\rangle = 2P^+(2\pi)^3\delta^3(P-P')\delta_{jj'}\delta_{m_j m_j'}. \tag{1.23}$$

As mentioned in the preceding section, the LFWFs are boost-invariant (i.e. frame independent) following the boost invariance of the light-front Hamiltonian and the pure kinematic character of the light-front boost. To make this more explicit, we introduce the boost invariant variables for the Hamiltonian. With p_i being the momentum of the i-th particle, (note that $p_i \geq 0$) we have momentum conservation,

$$\sum_i p_i^+ = P^+; \qquad \sum_i \boldsymbol{p}_i^\perp = \boldsymbol{P}^\perp \qquad (i=1,2,3,...) \tag{1.24}$$

Then we define the longitudinal momentum fraction for the i-th particle as $x_i \equiv p_i^+/P^+ \geq 0$, and transverse momentum $\boldsymbol{k}_i^\perp = \boldsymbol{p}_i^\perp - x_i \boldsymbol{P}^\perp$. This is equivalent to evaluating the LFWFs in a special reference frame where $P^+ = 1$, $P^\perp = 0$. The new conservation of momentum reads,

$$0 \leq x_i \leq 1, \qquad \sum_{i=0}^{n} x_i = 1; \qquad \sum_{i=0}^{n} \boldsymbol{k}_i^\perp = 0. \tag{1.25}$$

Then the LFWFs can be written as boost-invariant amplitudes, i.e. without explicit dependence on P^+ or $\boldsymbol{P}^\perp$:

$$\psi_{h/n}(p_1, \lambda_1, p_2, \lambda_2, ...p_n, \lambda_n; P, j, m_j) \triangleq \psi_{h/n}(\boldsymbol{k}_1^\perp, x_1, \lambda_1, \boldsymbol{k}_2^\perp, x_2, \lambda_2, ...\boldsymbol{k}_n^\perp, x_n, \lambda_n; P^2, j, m_j). \tag{1.26}$$

1.3.1 Fock Sector Dependent Renormalization

The renormalization procedures for perturbative theory are well-established and are implemented order-by-order in an expansion of a physical amplitude. However, in a nonperturbative approach one needs to sum over an infinite number of perturbative diagrams. A number of nonperturbative renormalization schemes have been proposed for light-front dynamics. Among them, the Fock sector dependent renormalization (FSDR) is a very promising approach [19–23]. Since the Fock sector truncation is a convenient approximation within light-front dynamics, FSDR is an appealing renormalization scheme. FSDR is a systematic renormalization scheme that works for general truncated Fock spaces. It provides a system where one can, in principle, systematically add higher Fock sectors to obtain increasingly accurate nonperturbative results [24, 25]. FSDR has been demonstrated to be numerically robust in the scalar Yukawa model with a Fock space that includes up through 4 bosons [24, 26].

FSDR starts with the identification of counterterms, and it allows the counterterms to depend on the truncation of Fock sectors. This dependence on Fock sector ensures the cancellation of the sub-divergence, and is also in analogy to the Forest Formula in the perturbation theory [27]. In Chap. 4, we followed FSDR to address the mass counterterm within Two-body Fock sector in QED. While sector-dependent counterterms are determined recursively, one can nevertheless add sectors systematically to include more constituents.

1.3.2 Light-Front Vacuum

The primary importance in the light-front theory is the existence of a vacuum state that is the eigenstate of zero energy in the full theory with a normal-ordered Hamiltonian. The existence of this state provides a foundation for the investigation of at least some of the complexities that must exist in QCD. In this picture, it is believed that the structures of the vacuum obtained in equal-time formulations are transferred to the zero modes of light-front theory. Zero modes in light-front field theory are usually discussed in two aspects: one is from the long-range physics of spontaneous symmetry breaking [28, 29], the other is the topological structure of the theory [30–32].

When the zero mode operator is associated with the long-range phenomena, it is no longer an independent degree of freedom but obeys the constraint equation [33]. It has been shown that for massive theories, the energy and momentum derived from light-front quantization are conserved and are equivalent to the energy and momentum in equal-time theory [34, 35]. While for the theories allowing spontaneous symmetry breaking there is a degeneracy of light-front vacua, and the true vacuum state differs from the perturbative vacuum through the addition of the zero quanta [36–38]. An analysis of the zero mode constraint equation for $(1+1)$-dimensional ϕ^4 field with a Tamm-Dancoff truncation (i.e. Fock sector truncation) suggests that states with a large number of particles or large momentum do not have an important contribution to the zero mode [39, 40].

Overall, zero modes in light-front field theory remain an open problem. It is a fascinating and challenging topic which is beyond the scope of this thesis. For our QCD applications, we assume that the physics of the neglected zero modes can be absorbed into the parameters of our assumed form of confinement and quark masses.

1.4 Light-Front Quantization

1.4.1 Discretized Light-Cone Quantization

The discretized light-cone quantization (DLCQ) approach is known as a method that can combine the light-front vacuum with an appealing treatment of the infrared degrees of freedom [41, 42].

It was first introduced for the $1+1$ dimension case and provided the first light-front numerical solutions to some nontrivial quantum field theories. For $3+1$ dimensions, the discretization is achieved by imposing periodic or anti-periodic boundary conditions in a box in the full coordinate space: $-L \leq x^- \leq L$, $-L_\perp \leq x, y \leq L_\perp$, with the periodic condition applied to bosons and the antiperiodic condition applied to fermions. In particular. the discretized momenta are given by:

$$
k^+ = \frac{2\pi}{L}j, \quad k^\perp = \left(\frac{2\pi}{L_\perp}n_x, \frac{2\pi}{L_\perp}n_y \right); \quad j, n_x, n_y = \begin{cases} 0, 1, 2, ... \text{ boson (periodic condition)} \\ \frac{1}{2}, \frac{3}{2}, ... \text{ fermion (antiperiodic condition)} \end{cases},
$$
(1.27)

and the total longitudinal momentum $P^+ = \sum_i k_i^+ \triangleq \frac{2\pi}{L}K$. Zero modes are neglected so the integer "0" is then omitted from the list of boson modes. Due to the light-front boost invariance, the light-cone Hamiltonian and LFWFs only depend on the longitudinal momentum fraction $x \equiv \frac{k^+}{P^+} = \frac{j}{K}$, that is, they are independent of the box length L. K represents the resolution of the system in the longitudinal direction and also imposes a natural restriction on the number of particles allowed in the basis space. In the transverse direction, a cutoff Λ is introduced so that $m_i^2 + p_i^2 \leq x_i\Lambda^2$. The continuum limit is achieved by taking $L \to \infty$[3] and $\Lambda \to \infty$.

1.4.2 Basis Light-Front Quantization

Among several light-front field theory approaches, basis light-front quantization (BLFQ) is a basis-function representation approach based on the Hamiltonian formalism which can facilitate the implementation of symmetries within light-front dynamics [43, 44]. Similar to DLCQ, it is a matrix diagonalization approach which generalizes the discretized momentum basis subject to continuous variables in both momentum or coordinate space.

In principle, there is freedom to choose any orthonormal and complete set of basis functions. However, for convenience and utility for bound state applications, one often selects the two-dimensional harmonic oscillator basis for the transverse motion. For QCD applications, this basis can be matched with confining interaction from the soft-wall anti-de Sitter/quantum chromodynamics (AdS/QCD) model obtained from light-front holography [45, 46]. One of its appealing

---

[3] For any finite P^+, it also implies $K \to \infty$.

features is that this basis preserves the rotational symmetry in the transverse plane. It allows the factorization of the center-of-mass motion when working in the single-particle basis in combination with the conjugate basis [47]. Specifically, each elementary field in the theory is expanded in terms of two-dimensional harmonic oscillator modes defined by

$$\phi_{nm}(\rho,\theta) = \frac{b}{\sqrt{\pi}}\sqrt{\frac{n!}{(n+|m|)!}}\mathrm{e}^{-b^2\rho^2/2}(b\rho)^{|m|}L_n^{|m|}(b^2\rho^2)\mathrm{e}^{im\theta}, \tag{1.28}$$

where ρ is the conventional radial variable in the dimension of length, n and m characterize the principal and orbital quantum numbers, respectively, b is the characteristic momentum scale. Note that, for reference, the eigenvalues of the two-dimensional harmonic oscillator are proportional to the total oscillator quanta $(2n+|m|+1)$. The orthonormal relation is given by

$$\langle n'm'|nm\rangle = \int_0^\infty\int_0^{2\pi}\rho\,\mathrm{d}\rho\,\mathrm{d}\theta\,\phi_{n'm'}^*\phi_{nm} = \delta_{n,n'}\delta_{m,m'}. \tag{1.29}$$

For the longitudinal modes, one can, for example, follow DLCQ and adopt the discrete plane wave function $\psi(x^-)$ for $-L \leq x^- \leq L$ with both periodic boundary conditions (PBC) and antiperiodic boundary conditions (APBC):

$$\psi_k(x^-) = \frac{1}{\sqrt{2L}}\exp\left(\mathrm{i}kx^-/L\right), \tag{1.30}$$

where $k = 1, 2, 3...$ (integers) is for the PBC [4], and $k = \frac{1}{2}, \frac{3}{2}, \frac{5}{2}, ...$ (half integers) is for APBC. As the box length reaches infinity, the continuum limit is achieved, and the convention of the integration and δ-function is listed in Table. 1.2.

The full 3-dimensional (3D) single particle basis state is defined as

$$\Psi_{nmk}(\rho,\theta,x^-) = \phi_{nm}(\rho,\theta)\psi_k(x^-) \tag{1.31}$$

With the given basis, we can define the creation operator in a basis representation

$$a_\lambda^\dagger(\alpha) = \int\frac{\mathrm{d}^3p}{2p^+(2\pi)^3}\Psi_\alpha(p)a_\lambda^\dagger(p), \tag{1.32}$$

with quantum numbers $\alpha = \{n, m, k\}$, and it satisfies the canonical commutation relation

$$\left[a_\lambda(\alpha), a_{\lambda'}(\alpha')\right] = \delta_{\alpha\alpha'}\delta_{\lambda\lambda'}. \tag{1.33}$$

---

[4] Zero mode $k = 0$ is again neglected.

Table 1.2: Conversion formula for the box regularization.

box regularization	$\xrightarrow{L\to\infty}$	continuum
$\int_{-L}^{+L} \mathrm{d}x^-$		$\int_{-\infty}^{+\infty} \mathrm{d}x^-$
$\dfrac{1}{L}\displaystyle\sum_{p^+}$	$\xrightarrow{L\to\infty}$	$\int_{-\infty}^{+\infty} \dfrac{\mathrm{d}k^+}{2\pi}$
$L\delta_{k^+,k'^+}$		$2\pi\delta(k^+ - k'^+)$

This choice of basis function was first applied to solve the a cavity-mode QED problem as well as extended to a cavity-mode QCD problem in Ref. [43]. Later, BLFQ was used to solve for specific self-bound systems such as positronium and heavy quarkonium [17, 48, 49]. BLFQ has been extended to time-dependent external field problems such as the non-linear Compton scattering [50–52].

For bound state problems in which longitudinal confinement is introduced, an alternative and convenient basis is introduced [48, 49]. We will discuss that option when we discuss our investigation of mixed-flavor mesons. We now proceed to investigate specific light-front Hamiltonian systems in QED and QCD using the BLFQ approach.

1.5   Practical Considerations and Applications Investigated

Light-front quantum field theory has the advantage of simple dynamics and trivial vacuum structure with the neglect of zero mode, which make it an ideal tool for relativistic bound-state problem. On the other hand, the development of supercomputers provides the capability of performing large-scale computations. Since BLFQ is an appealing computational framework to solve the light-front QCD eigenvalue equation, we will adopt it and study the basis size needed to achieve a specified accuracy in a given application.

The framework of BLFQ with AdS/QCD was successfully applied to investigate the heavy quarkonia system by Li et al. [48, 49] The question naturally arises whether this approach is suc-

cessful when applied to mesons with mixed flavor. We will therefore extend this Hamiltonian to the unequal-mass two-body system, and use the obtained wave functions to compute the intrinsic structures of the mixed-flavor mesons. We first study the heavy mesons with unequal mass constituents in Chap. 2 with BLFQ. They include the B_c meson containing two different heavy quarks, and B, B_s, D, D_s, i.e. the heavy-light mesons. For these systems, we only introduce two new parameters which are the quark masses for up quark m_u and strange quark m_s, yet obtain very promising mass spectra and LFWFs by solving the eigenvalue equations. We also calculate selected observables with the resulting LFWFs, and compare with other theoretical approaches and experimental results where available.

Then we calculate the semileptonic form factors in Chap. 3. We investigate the decay from the B_c ground state to η_c and J/ψ with the LFWFs we obtained in Chap. 2 and previous work [49]. In this part we focus on the issue of the dependence on the choice of frame which is caused by the truncation of Fock sector that results in the violation of Lorentz invariance. We also introduce aspects of high performance computing in this chapter to illustrate the idea of parallel computing we use for our numerical calculations.

So far the meson systems we investigated are all within the leading Fock, quark-antiquark, sector. More complete results could be revealed if we were able to add higher Fock sectors. However this is not an easy task due to extensive challenges in the physics aspects arising from renormalization and in the numerical aspects arising from the growth of computational complexity. Thus we start the path to nonperturbative renormalization with a QED scenario. In Chap. 4 we implement the BLFQ approach to tackle the physical electron system with the Fock sector that includes a dynamical photon in order to illustrate the potential utility of BLFQ. This extension to include a dynamical photon is based, in part, on a former work investigating the g-2 factor of the electron. Our extensions include explorations of the nonzero kinematic region for the electromagnetic form factors, as well as for the gravitational form factors of the electron. We compare our BLFQ result with results from light-front perturbation theory and we find that, as may be expected, they agree with each other reasonably well. We also adopt the conjugate harmonic oscillator basis in this work

which can factorize the center-of-mass motion as well as help accelerate convergence with increasing basis size.

Finally we summarize our conclusions in Chap. 5.

CHAPTER 2. HEAVY MESONS WITH BASIS LIGHT-FRONT QUANTIZATION APPROACH

This chapter follows Refs. [53, 54] which was completed as a component of the PhD research.

Heavy mesons provide multiscale testing ground for both perturbative and nonperturbative QCD [55]. Interests in heavy-flavor quarks[1] have been raised again due to the discoveries of exotic states with a heavy quark [56, 57]. Meanwhile, due to the demand for higher accuracy in experiments, large colliders such as Belle-II have upgraded their facilities and plan to produce extensive data on heavy mesons [58]. In this chapter, we study the two-body bound-state QCD problem with the BLFQ approach. In particular, we investigate the flavored mesons which include the unequal heavy-heavy (both the quark and the antiquark have masses above 1 GeV) meson B_c, and the heavy-light (one of the two constituents has a mass below 1 GeV) mesons B, B_s, D, and D_s.

In the previous work, a light-front holographic model [59] is embedded in the BLFQ formulation to model the heavy quarkonia (charmonium and bottomonium, systems where the masses of the quark and antiquark are equal and above 1 GeV) [48, 49], which shows good agreement with existing experiments and other theoretical models. The successful application to heavy quarkonia inspires us to implement the same form of Hamiltonian to the unequal-mass heavy mesons. To be specific, this model contains the AdS/QCD soft-wall confinement [60] and a longitudinal confinement [48], both of which control the long-distance physics. It also includes the short-distance interaction as an effective one-gluon-exchange potential [49], which embeds the spin structure information.

Extension from equal-mass to unequal-mass systems is in principle straightforward, yet the asymmetry character of the unequal-mass mesons is interesting. Meanwhile, when a light quark is involved in the bound state, one may expect some effects on the mass spectrum of the pseudoscalar and vector due to the chiral effect. We will illustrate those questions in the followings parts.

---

[1]The charm (c), bottom (b) and top (t) are conventionally referred as the "heavy quarks". However, since t quark is too heavy to form a stable bound state, we only discuss systems with c and b in this thesis.

2.1 Hamiltonian Formalism and the Basis Function Representation

A two-body hadron (h) state $|\psi_h\rangle$ can be written as various many-body components in the Fock space:

$$|\psi_h\rangle = |q\bar{q}\rangle + |q\bar{q}g\rangle + |q\bar{q}q\bar{q}\rangle + ... \tag{2.1}$$

Although the full picture of these many-body dynamics is complicated, it is reasonable to take into account only the $|q\bar{q}\rangle$ sector as a first approximations for heavy mesons. Therefore we adopt the effective Hamiltonian for the leading Fock sector $|q\bar{q}\rangle$, which essentially comprises two pieces of interactions: $H_{\text{tot}} = H_0 + V_g^{\text{eff}}$, where

$$H_0 = \frac{\vec{k}_\perp^2 + m_q^2}{x} + \frac{\vec{k}_\perp^2 + m_{\bar{q}}^2}{1-x} + \kappa^4 \vec{\zeta}_\perp^2 - \frac{\kappa^4}{(m_q + m_{\bar{q}})^2} \partial_x \left(x(1-x)\partial_x \right) \tag{2.2}$$

is the holographic QCD Hamiltonian [48, 60] augmented by massive quark kinematics and the longitudinal confinement [48, 49]. Here x and $(1-x)$ are the longitudinal momentum fractions of the quark and antiquark, respectively. $\vec{\zeta}_\perp = \sqrt{x(1-x)}\vec{r}_\perp$ is the holographic variable [59] and $\vec{r}_\perp = \vec{r}_{q\perp} - \vec{r}_{\bar{q}\perp}$ denotes the transverse separation of partons.

In addition, the spin structure of the hadrons is generated by the effective one-gluon-exchange potential V_g^{eff}, which governs the short-range physics:

$$V_g^{\text{eff}} = -\frac{C_F 4\pi\alpha_s(Q^2)}{Q^2} \bar{u}_{s'}(k')\gamma_\mu \mu_s(k)\bar{v}_{\bar{s}}(\bar{k})\gamma^\mu v_{\bar{s}'}(\bar{k}'), \tag{2.3}$$

where $C_F = (N_c^2 - 1)/(2N_c) = 4/3$ is the color factor of the $q\bar{q}$ color singlet state. We incorporate a running coupling for the one-gluon-exchange potential. For each $Q^2 = -1/2(k'-k)^2 - 1/2(\bar{k}'-\bar{k})^2$ [2], the average 4-momentum squared transferred by the exchanged gluon, the running coupling constant is modeled as

$$\alpha_s(Q^2) = \frac{1}{\beta_0 \ln(Q^2/\Lambda^2 + \tau)}, \tag{2.4}$$

with $\beta_0 = (33 - 2N_f)/(12\pi)$. The quark flavor number taken as $N_f = 4$ for B, B_s, and B_c, while $N_f = 3$ for D and D_s. We use $\Lambda = 0.13$ GeV, and in order to avoid the perturbative QCD infrared (IR) divergence, we use $\tau = 12.3$ such that $\alpha(0) = 0.6$ [49].

---

[2] Q^2 written in terms of kinematical variables can be found in Appendix B, where we set the gluon mass $\mu_g = 0.02$ GeV to regularize the integrable Coulomb singularity in the energy denominator and to avoid numerical instability.

The light-front Hamiltonian formalism leads to an eigenvalue equation

$$H_{\text{tot}} \left| \Psi_h(P, j, m_j) \right\rangle = M_h^2 \left| \Psi_h(P, j, m_j) \right\rangle, \tag{2.5}$$

where $P = (P^-, P^+, \vec{P}_\perp)$ is the 4-momentum of the hadron bound state; j and m_j are the hadron's total angular momentum and magnetic projection, respectively. Within the Fock space representation limited to $|q\bar{q}\rangle$ sector, the meson eigenstate reads

$$\begin{aligned}
\left| \Psi_h(P, j, m_j) \right\rangle = &\sum_{s, \bar{s}} \int_0^1 \frac{\mathrm{d}x}{2x(1-x)} \int \frac{\mathrm{d}k_\perp}{(2\pi)^3} \psi_{s\bar{s}/h}^{(m_j)}(x, \vec{k}_\perp) \\
&\times \frac{1}{\sqrt{N_c}} \sum_{i=1}^{N_c} b_{si}^\dagger \left(xP^+, \vec{k}_\perp + x\vec{P} \right) d_{\bar{s}i}^\dagger \left((1-x)P^+, -\vec{k}_\perp + (1-x)\vec{P} \right) |0\rangle,
\end{aligned} \tag{2.6}$$

where the coefficient $\psi_{s\bar{s}/h}^{(m_j)}(\vec{k}_\perp, x)$ of the expansion is the valence sector LFWF. In the BLFQ framework, we solve the eigenvalue equation (Eq. (2.5)) with the basis function approach, which provides remarkable advantage since the wavefunctions of H_0 provide a natural orthonormal basis. These wavefunctions can be separated into two basis functions ϕ_{nm} and χ_l. For the transverse direction, we have the 2-dimensional (2D) harmonic oscillator function

$$\phi_{nm}(\vec{q}_\perp) = \frac{1}{b} \sqrt{\frac{4\pi n!}{(n+|m|)!}} \left(\frac{q_\perp}{b} \right)^{|m|} e^{-\frac{1}{2}q_\perp^2/b^2} L_n^{|m|}(q_\perp^2/b^2) e^{im\theta_q}, \tag{2.7}$$

where n and m are the principal and orbital quantum numbers, respectively; $\vec{q}_\perp = \vec{k}_\perp/\sqrt{x(1-x)}$, $q_\perp = |\vec{q}_\perp|$, $\theta_q = \arg \vec{q}_\perp$; b is the oscillator basis energy scale parameter, and $L_n^{|m|}$ is the associated Laguerre polynomial. The longitudinal basis functions are chosen to be

$$\chi_l(x) = \sqrt{4\pi(2l + \alpha + \beta + 1)} \sqrt{\frac{\Gamma(l+1)\Gamma(l+\alpha+\beta+1)}{\Gamma(l+\alpha+1)\Gamma(l+\beta+1)}} x^{\frac{\beta}{2}} (1-x)^{\frac{\alpha}{2}} P_l^{(\alpha,\beta)}(2x-1), \tag{2.8}$$

where $P_l^{(\alpha,\beta)}(2x-1)$ is the Jacobi polynomial with quantum number l. α and β are two dimensionless parameters associated with the constituent (anti-) quark masses [48]

$$\alpha = 2m_{\bar{q}}(m_q + m_{\bar{q}})/\kappa; \qquad \beta = 2m_q(m_q + m_{\bar{q}})/\kappa. \tag{2.9}$$

As such, the longitudinal solutions $\chi_l(x)$ resemble the perturbative QCD asymptotic parton distribution $\sim x^\alpha(1-x)^\beta$ for mesons [61].

The direct product of two basis functions $\psi_{nml} = \phi_{nm}(\vec{k}_\perp/\sqrt{x(1-x)})\chi_l(x)$ gives the analytical solution of the eigenvector of the basis Hamiltonian H_0, with the eigenvalue,

$$M_{nml}^2 = (m_q + m_{\bar{q}})^2 + 2\kappa^2 \left(2n + |m| + l + 1\right) + \frac{\kappa^4}{(m_q + m_{\bar{q}})^2} l(l+1). \tag{2.10}$$

When the effective one-gluon-exchange potential V_g^{eff} is incorporated, the off-diagonal matrix elements of the Hamiltonian become nonzero. Therefore we numerically diagonalize the Hamiltonian matrix H_{tot} to obtain the eigenvalues, which represent the squared mass of the bound states, and the eigenvectors as basis coefficients $\psi_h(n, m, l, s, \bar{s})$. Hence the LFWFs of the system including V_g^{eff} is given by

$$\psi_{s\bar{s}/h}^{(m_j)}\left(x, \vec{k}_\perp\right) = \sum_{nml} \psi_h\left(n, m, l, s, \bar{s}\right) \phi_{nm}\left(\vec{k}_\perp/\sqrt{x(1-x)}\right) \chi_l(x). \tag{2.11}$$

Note that the diagonalization is taken with respect to specific m_j. This conserved total magnetic projection m_j is the sum of the orbital angular momentum projection m and the spin projections, i.e. $m_j = m + s + \bar{s}$. With the orthonormal basis functions, the LFWFs are also normalized to unity

$$\sum_{s\bar{s}} \int_0^1 \frac{\mathrm{d}x}{2x(1-x)} \int \frac{\mathrm{d}k_\perp^2}{(2\pi)^3} \left|\psi_{s\bar{s}/h}^{(m_j)}\left(x, \vec{k}_\perp\right)\right|^2 = 1. \tag{2.12}$$

By performing a 2D Fourier transform, one obtains the LFWFs in the 2D transverse coordinate space:

$$\widetilde{\psi}_{s\bar{s}/h}(x, \vec{r}_\perp) = \sqrt{x(1-x)} \sum_{nml} \psi_h(n, m, l, s, \bar{s}) \widetilde{\phi}_{nm}\left(\sqrt{x(1-x)}\vec{r}_\perp\right) \chi_l(x), \tag{2.13}$$

where $\widetilde{\phi}_{nm}$ is the 2D harmonic oscillator function in coordinate space with characteristic momentum scale b,

$$\widetilde{\phi}_{nm}\left(\vec{\rho}_\perp\right) = b\sqrt{\frac{n!}{\pi(n+|m|)!}} (b\rho_\perp)^{|m|} \exp\left(-b^2\rho_\perp^2/2\right) L_n^{|m|}(b^2\rho_\perp^2) \exp\left[im\theta_\rho + i\pi(n+|m|/2)\right]. \tag{2.14}$$

For practical calculations, we have to truncate the basis by restricting the quanta:

$$2n + |m| + 1 \leq N_{\max}, \qquad 0 \leq l \leq L_{\max}. \tag{2.15}$$

The transverse cutoff parameter $N_{\max}$ is associated with ultraviolet (UV) and infrared (IR) regulators as $\Lambda_{\text{UV}} \approx b\sqrt{N_{\max}}$ and $\lambda_{\text{IR}} \approx b/\sqrt{N_{\max}}$ [62] where the scale parameter for the harmonic

oscillator basis is equal to the confining strength, i.e. $b = \kappa$. $L_{\max}$ controls the resolution of the basis along the longitudinal direction. The complete basis is reached when $N_{\max} \to \infty$, $L_{\max} \to \infty$. We refer the readers to Appendices C, D, and E for additional details on the formalism and computational methods.

2.2 Numerical Results

In the framework of BLFQ, the confining strength κ and constituent (anti-) quark masses m_q ($m_{\bar{q}}$) are typically free parameters that are fitted to experiments. For B_c ($b\bar{c}$) mesons, we adopt the model parameters from the those of the heavy quarkonia without doing further adjustment: the quark masses m_b and m_c are the same as in bottomonium and charmonium, respectively. On the other hand, we implement the confining strength of the flavored mesons as $\kappa_{x\bar{y}} = \sqrt{(\kappa_{x\bar{x}}^2 + \kappa_{y\bar{y}}^2)/2}$ which is in accordance with the heavy quark effective theory [63]. While for the heavy-light systems, we fit the lighter quark masses of up/down ($m_{u/d}$) and strange (m_s) to minimize the r.m.s. mass deviation between experiment and theory for the lowest pseudoscalar and vector states, D^0, $D^*(2007)$, $B^{\pm}$, B^* ($D_s^{\pm}$, $D_s^{*\pm}$, B_s^0, B_s^{*0}). We test our model at both $\kappa_{u\bar{u}/d\bar{d}} = \kappa_{s\bar{s}} = 0.54$ GeV and 0.59 GeV as the confining strength for light mesons [59], and found the overall spectra were not significantly affected. See details in Table 2.1, where all other model parameters are provided.

2.2.1 Mass Spectrum

In order to identify the multiplet of magnetic substates belonging to a single angular momentum j, we diagonalize the Hamiltonian matrix [3] in the basis space with different m_j's. The obtained eigenvalue is the mass squared of the states, which shown an example of B_c meson with respect to m_j in Fig. 2.1. Then one needs to perform the state identification to deduce the full set of quantum numbers $\mathsf{n}^{2S+1}\ell_j$ or j^{P}, where ℓ is the orbital angular momentum and n is the radial quantum

---

[3] The Hamiltonian matrix elements involves a six-dimensional integral.

Table 2.1: Summary of the model parameters with the basis truncation $N_{\max} = L_{\max} = 32$. Among them $m_u = 0.553$ or 0.554 GeV and $m_s = 0.647$ or 0.648 GeV are the only fitted parameters. The former is fitted when $\kappa_{u\bar{u},s\bar{s}} = 0.59$ GeV, while the latter is when $\kappa_{u\bar{u},s\bar{s}} = 0.54$ GeV. The calculated meson masses of the two low-lying states, known as pseudoscalar (PS) and vector (V), are listed in the table. The r.m.s. are the root-mean-square differences of our results from the experimental measured masses; the number of compared states $N_{\exp}$ are shown in the square brackets. The mean spread $\overline{\delta_j M}$ is the spread in the masses over allowed m_j values and the deviation from zero reflects the violation of rotational symmetry. Following the absolute mean spread value, we provide the relative spread with respect to the total mass of constituent (anti-) quarks in the parenthesis.

|	N_f	m_q (GeV)	$m_{\bar{q}}$ (GeV)	κ (GeV)	$\overline{M}$ (GeV) PS	V	r.m.s.(MeV) $[N_{\exp}]$	$\overline{\delta_j M}$ (MeV)
$c\bar{u}$	3	1.603	0.553	0.800	1.842	2.050	78 [5]	30 (1.4%)
			0.554	0.783	1.845	2.047	74 [5]	28 (1.3%)
$c\bar{s}$	3	1.603	0.647	0.800	1.944	2.147	40 [9]	25 (1.1%)
			0.648	0.783	1.947	2.143	43 [9]	24 (1.1%)
$c\bar{c}$	4	1.603	1.603	0.966	3.017	3.139	31 [8]	20 (.62%)
$b\bar{u}$	4	4.902	0.553	1.067	5.291	5.339	21 [4]	6.0 (.11%)
			0.554	1.054	5.290	5.338	26 [4]	5.8 (.11%)
$b\bar{s}$	4	4.902	0.647	1.067	5.379	5.428	37 [4]	5.6 (.10%)
			0.648	1.054	5.379	5.427	42 [4]	5.3 (.10%)
$b\bar{c}$	4	4.902	1.603	1.196	6.258	6.316	37 [2]	5.3 (.08%)
$b\bar{b}$	5	4.902	4.902	1.389	9.475	9.514	38 [14]	5.6 (.06%)
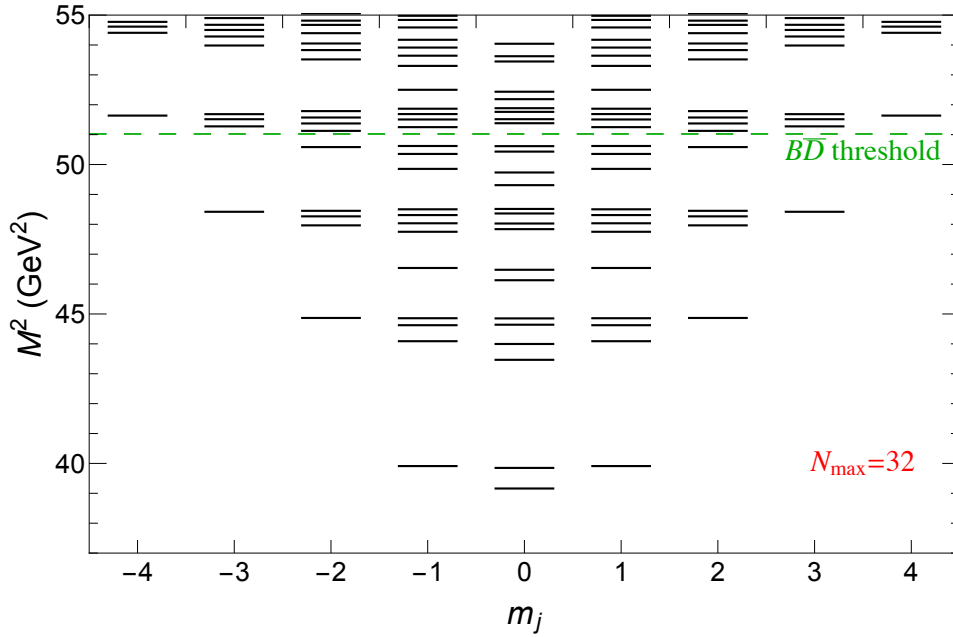
Figure 2.1: A visualized mass spectrum of B_c obtained by diagonalizing the light cone Hamiltonian within various m_j sectors at $N_{\max} = L_{\max} = 32$. The spectrum is symmetric with respect to $\pm m_j$, which is a consequence of the mirror parity symmetry. Even though the rotational symmetry is not exact since the first exited state at different m_j do not line up, the approximate degeneracies are still helpful to extract j.

number. [4] We calculated the discretized mirror parity for states identification $m_P = (-\mathrm{i})^{2j}\mathsf{P}$. Although total spin $\left\langle \vec{s}^2 \right\rangle = s(s+1)$ is an approximate quantum number, it is also exploited to help.

The reconstructed mass spectra of the mesons up to their corresponding open flavor thresholds are presented in Fig. 2.2. For each states, we use the dashed lines for the mean values of invariant masses:

$$\overline{M} \equiv \sqrt{\frac{M_{-j}^2 + M_{1-j}^2 + ... + M_j^2}{2j + 1}}, \tag{2.16}$$

and the boxes indicate the spread of eigenmasses obtained from different m_j's: $\delta_j M \equiv \max(M_{m_j}) - \min(M_{m_j}) =$ box height. In many cases, the box height is small and not visible in the figure. Since rotational symmetry would imply degeneracy (zero box height), we introduce an overall mean spread for hadrons within a fixed flavor to quantify the violation of rotational symmetry from all

---

[4] Note to distinguish them from the basis quantum numbers l and n.

high spin states below their respective dissociation thresholds,

$$\overline{\delta_j M} \equiv \sqrt{\frac{1}{N_h} \sum_h^{j \neq 0} (\delta_j M_h)^2} \qquad \left(N_h \equiv \sum_h^{j \neq 0} 1\right). \tag{2.17}$$

In particular, we calculate the $\overline{\delta_j M}$ for the first 9 states, which includes three $j^P = 1^-$ states, two 1^+, one 2^+, two 2^-, and one 3^-, of the heavy mesons and quarkonia, and list them in the last column of Table 2.1. We observe that the mean spread has the tendency of decreasing with increasing meson mass, which is in agreement with our expectation. Viewed as a percentage deviation, the decrease with increasing meson mass is consistent with a trend found for all the mesons.

The hyperfine splitting of the ground state pseudoscalar and vector is a particularly delicate test of the spin-sensitive component of the Hamiltonian the effective one-gluon exchange interaction. It is well-known that for the light mesons, this mass splitting is driven by chiral symmetry breaking. However, in our approach, the splitting is brought in by the one-gluon exchange interaction and its interplay with the confining strength κ when the basis size is fixed by $N_{\max}$ and $L_{\max}$. Specifically, smaller κ tends to lead a larger mass splitting between the two states. The size of the hyperfine splittings are reasonable for heavy mesons and heavy-light mesons within this model. However, we observe that for BLFQ to reproduce the properties of the light mesons, such as the Goldstone nature of the pions in the chiral limit, the Hamiltonian needs to respect chiral symmetry constraints and exhibit dynamical chiral symmetry breaking.

We compare our mass spectra with experimental values summarized by the Particle Data Group (PDG) [64], and Lattice QCD in Fig. 2.2. Most of our results are within the quoted uncertainties of either experiments or Lattice. Some states, $j^P = 0^+$ or 1^+ for instance, show somewhat larger differences among the states compared. In BLFQ, the accuracy may be enhanced by introducing higher Fock sectors, such as including a dynamical gluon in the Fock sectors. Nevertheless, our work provides the LFWFs that can be used to calculate some hadron observables, which may be tested by ongoing and forthcoming experiments.
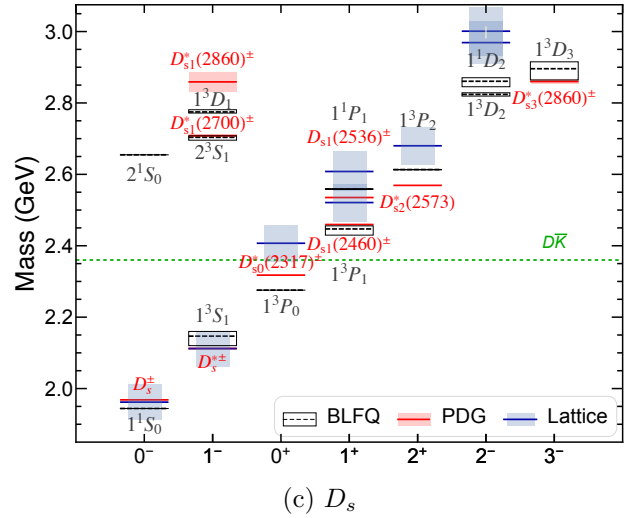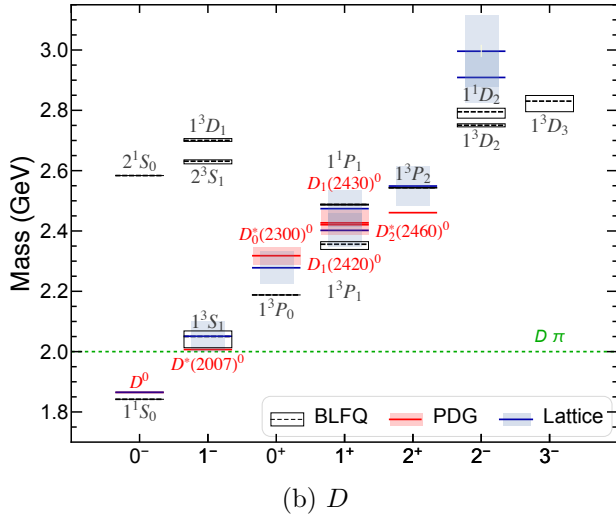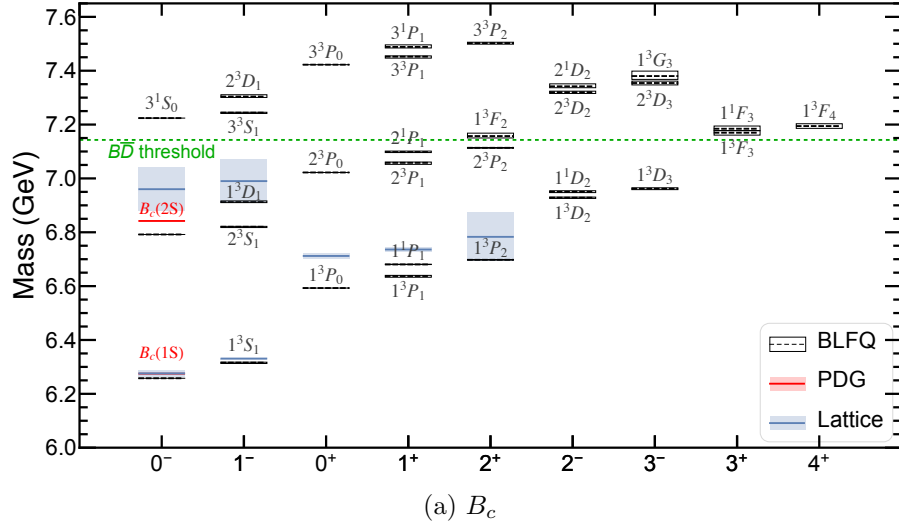
Figure 2.2: Mass spectra of the unequal-mass mesons with $N_{\max} = L_{\max} = 32$. Horizontal axis refers to the j^P values of the states. The green dashed lines indicate the corresponding open flavor threshold. Black boxes are the results of this work, indicating the highest and lowest mass from different m_j's, while the dashed lines in between are the averages $\overline{M}$. Red bars are the experimental masses summarized by PDG [64]. Specifically, we use the values of D^0 ($c\bar{u}$) and $B^\pm$ ($b\bar{u}/b\bar{d}$) from experiments for comparison. Shaded blue bars are the Lattice QCD results from Refs. [65–71]. For both PDG and Lattice, we use the solid lines for the center values, while shaded boxes to indicate the uncertainties.
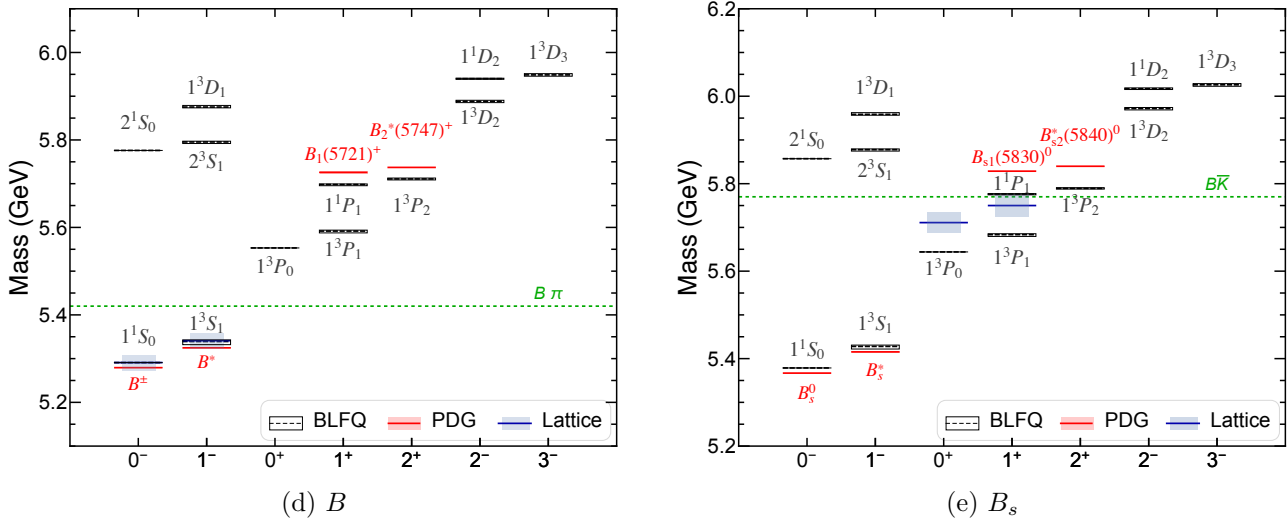
Figure 2.2: (continued)

2.2.2 Light-Front Wave Functions

Obtaining the LFWFs is a major motivation for BLFQ formalism, as they provide direct access to hadron structure observables. We solve the light-front Hamiltonian eigenvalue problem to determine the LFWFs, with the orthonormal condition reads,

$$\sum_{s\bar{s}} \int_0^1 \frac{\mathrm{d}x}{2x(1-x)} \int \frac{\mathrm{d}^2 k_\perp}{(2\pi)^3} \psi^{(m'_j)*}_{s\bar{s}/h'}(x, \vec{k}_\perp) \psi^{(m_j)}_{s\bar{s}/h}(x, \vec{k}_\perp) = \delta_{hh'} \delta_{m_j, m'_j}. \tag{2.18}$$

Here we present some of the valence LFWFs with different polarization and spin alignments for B_c ground states, a pseudoscalar with $j^{\mathsf{P}} = 0^-$, in Fig. 2.3. Specifically, we have the relation $m_j = s + \bar{s} + m$, where m is the orbital angular momentum projection. To visualize the LFWFs, we drop the phase $\exp(im\theta_q)$ in Eq. (2.7), while retaining the relative sign $\exp(im\theta_q) = (-1)^m$ for negative $k_\perp$. Namely,

$$\psi^{m_j}_{s\bar{s}}(x, k_\perp) \triangleq \begin{cases} \psi^{m_j}_{s\bar{s}}(x, k_\perp), & k_\perp \geq 0; \\ \psi^{m_j}_{s\bar{s}}(x, -k_\perp) \times (-1)^m, & k_\perp \leq 0. \end{cases} \tag{2.19}$$

There are two independent components with different spin alignments for the 0^- state: $\psi_{\uparrow\downarrow-\downarrow\uparrow}(x, \vec{k}_\perp) \equiv \frac{1}{\sqrt{2}} \left[\psi_{\uparrow\downarrow}(x, \vec{k}_\perp) - \psi_{\downarrow\uparrow}(x, \vec{k}_\perp) \right]$ and $\psi_{\downarrow\downarrow}(x, \vec{k}_\perp) = \psi^*_{\uparrow\uparrow}(x, \vec{k}_\perp)$. Furthermore, the unequal-mass mesons have another significant feature that is distinguished from the equal-mass systems. For the heavy
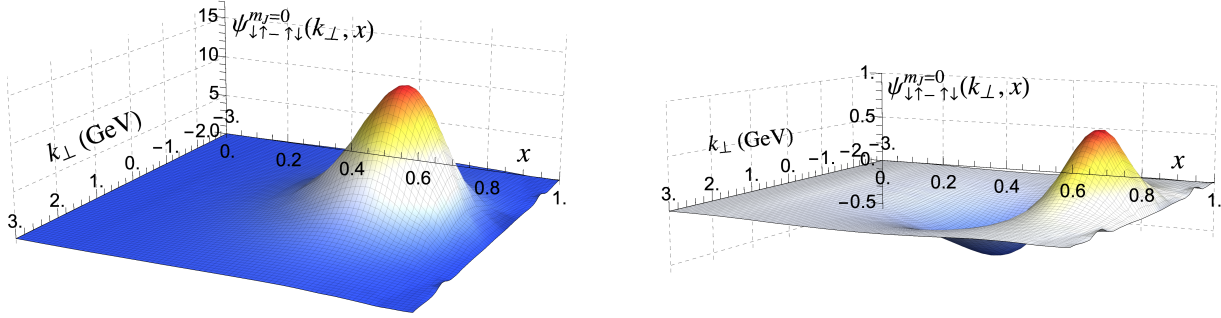
(a) $\psi_{\uparrow\downarrow-\downarrow\uparrow}(k_x, k_y = 0, x)$. **Left** : $(m + l) = $ Even; **Right** : $(m + l) = $ Odd.
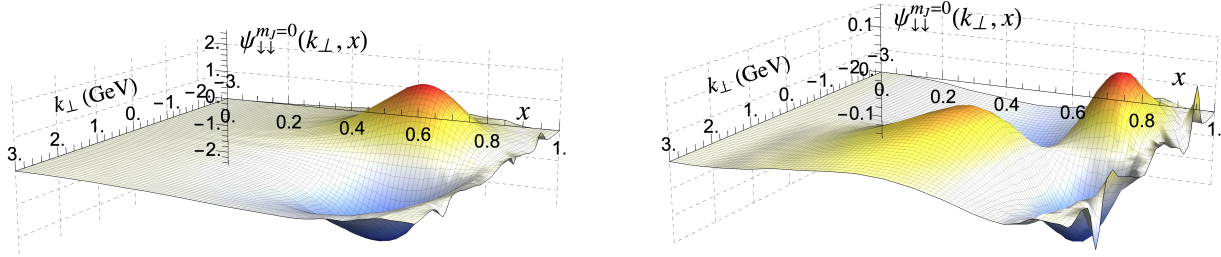
(b) $\psi_{\downarrow\downarrow}(k_x, k_y = 0, x) = \psi_{\uparrow\uparrow}^*(k_x, k_y = 0, x)$. **Left** : $(m + l) = $ Odd; **Right** : $(m + l) = $ Even.

Figure 2.3: LFWFs of the ground state B_c shown as plots of their magnitudes versus x and k_x at $k_y = 0$. In general the spin alignment (a) is dominant and reminiscent of nonrelativistic behavior, while (b) are purely relativistic components.

quarkonia, charge conjugation is a good symmetry and is reflected by states having components either even or odd in $(m+l)$ [48]. There is no charge conjugation symmetry of the flavored mesons, but we do observe that our wavefunctions are dominated by either even or odd $(m + l)$. Table 2.2 exhibits this dominance, along with the comparison with heavy quarkonia of the ground states. In a separate test calculation, we verified that, as the mass difference between quark and antiquark decreases, the contribution from even $(m + l)$ is getting smaller and progresses smoothly to the equal-mass limit.

On the other hand, we investigate the layout of the meson LFWFs which are also of interest. The equal-mass quarkonium LFWFs exhibit symmetry with respect to both the transverse momentum

Table 2.2: The probabilities of finding the specified even or odd $(m + l)$ in the ground state of heavy mesons. The dominant spin alignment listed here are the components that persist in the non-relativistic limit. Note the systematic increase of these dominant components with the increasing meson mass.

	Even/odd $(m + l)$			
System	$\left\|\psi_{\uparrow\downarrow-\downarrow\uparrow}(x, \vec{k}_\perp)\right\|^2$		$\left\|\psi_{\uparrow\uparrow}(x, \vec{k}_\perp)\right\|^2 + \left\|\psi_{\downarrow\downarrow}(x, \vec{k}_\perp)\right\|^2$	
	Even	Odd	Odd	Even
$c\bar{u}/c\bar{d}$	67.36%	0.60%	31.55%	0.49%
$c\bar{s}$	71.47%	0.41%	27.82%	0.30%
$c\bar{c}$	88.01%	0	11.99%	0
$b\bar{u}/b\bar{d}$	74.71%	2.38%	22.08%	0.83%
$b\bar{s}$	79.09%	1.81%	18.54%	0.56%
$b\bar{c}$	91.62%	0.35%	7.98%	0.05%
$b\bar{b}$	96.61%	0	3.39%	0

and longitudinal momentum fraction. We anticipate and observe that asymmetry emerges when the constituent masses differ. In Fig. 2.4, the left panels show the density plot of the dominant component in ground states of all systems, bottomonium, B_c, B, and D. All dominant components of ground state mesons displayed in Fig. 2.4 are symmetric in the transverse direction since we adopt the relative coordinate for the two-body systems. On top of that, the η_b wave function also shows the expected symmetry in the longitudinal direction. While for the unequal-mass mesons, they show the anticipated asymmetry in the longitudinal direction.

In particular, the peak of LFWFs for the quarkonium is located at $x = 1/2$ on the longitudinal direction, which is the same as the quark mass fraction $m_q/(m_q + m_{\bar{q}})$ where $m_q = m_{\bar{q}}$. However the peak location of the unequal-mass systems are nontrivial as shown in the right panels of Fig. 2.4. At $k_\perp = 0$ the asymmetry is maximal, and the peak is located at $x > m_q/(m_q + m_{\bar{q}})$, but as $k_\perp$ increases the peak location (along fixed $k_\perp$) shifts to smaller values of x. In the limit $k_\perp \to \infty$ the peak location approaches $x = 1/2$. This can easily be understood because for $k_\perp \gg m_q + m_{\bar{q}}$, the quark masses become irrelevant, and the wavefunction approaches that of equal-mass constituents. We use the blue dots to indicate the peak of the LFWFs and the red curve is fitted from the dots based on the light-front parton gas model [72, 73]. Explicitly, the obtained peak location in x at
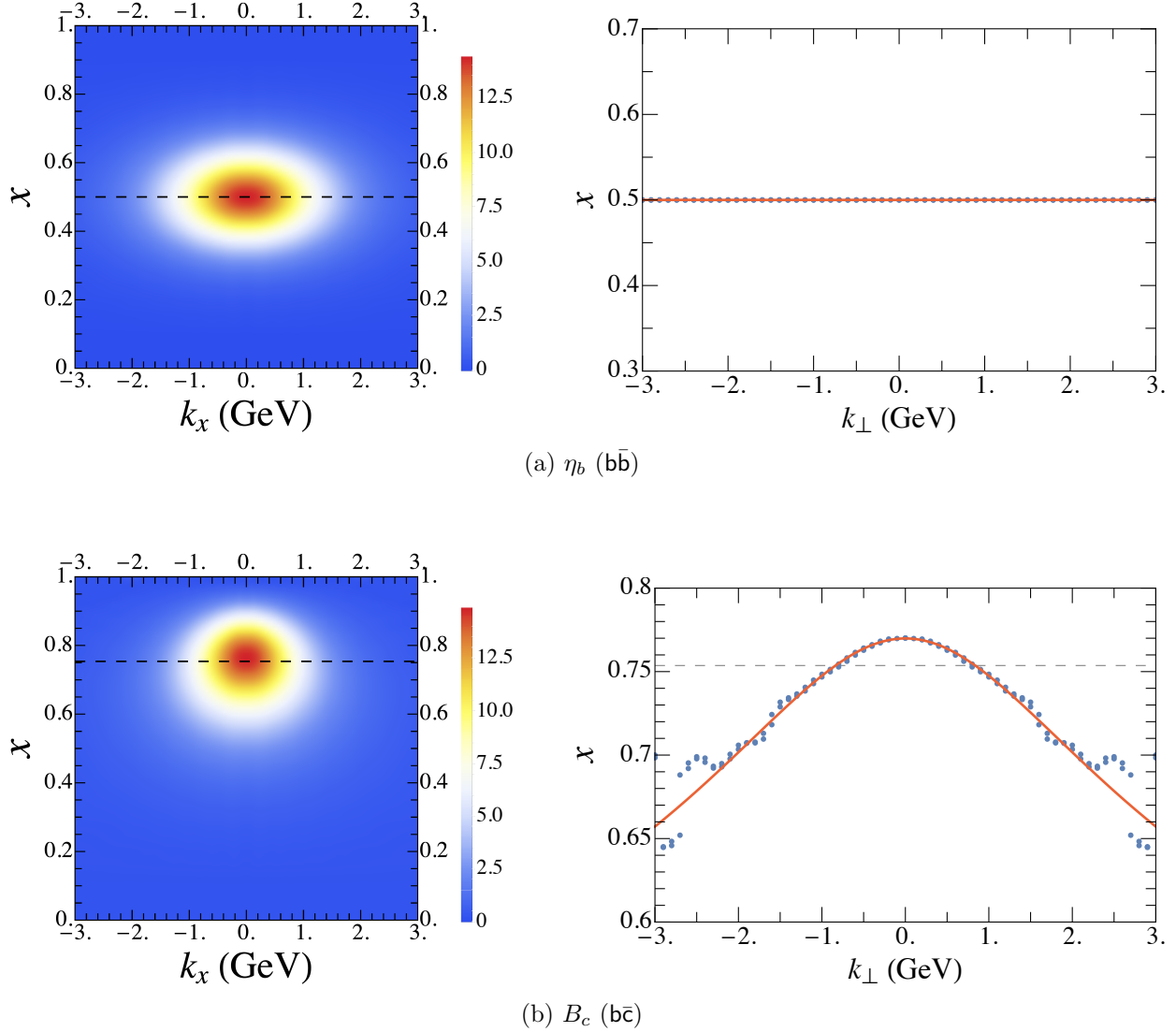
(a) η_b (b$\bar{\text{b}}$)

(b) B_c (b$\bar{\text{c}}$)

Figure 2.4: The density plots and peak distributions of the LFWFs of η_c, B_c, B, and D. The quark mass fraction $m_q/(m_q + m_{\bar{q}})$ is labeled by the horizontal dashed lines. For the equal-mass system, the LFWF is symmetry on x, and the peak of that is always located at $x = 1/2$ for all $k_\perp$'s. While for other unequal-mass systems, the peaks are located at $x > m_q/(m_q + m_{\bar{q}})$ when $k_\perp = 0$. As $k_\perp$ increases the peak shifts to smaller values of x and finally approaches to $x = 1/2$ at the limit $k \to \infty$.
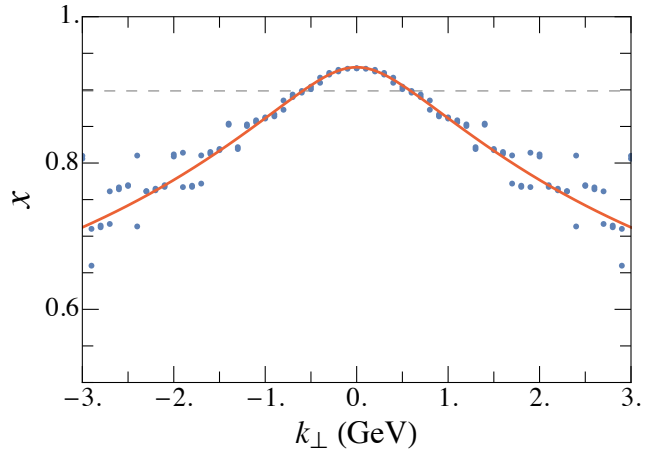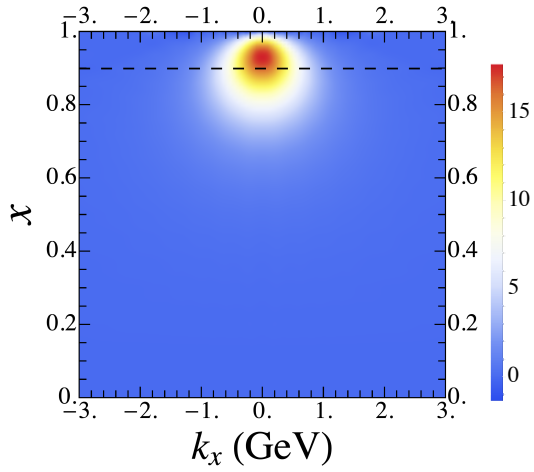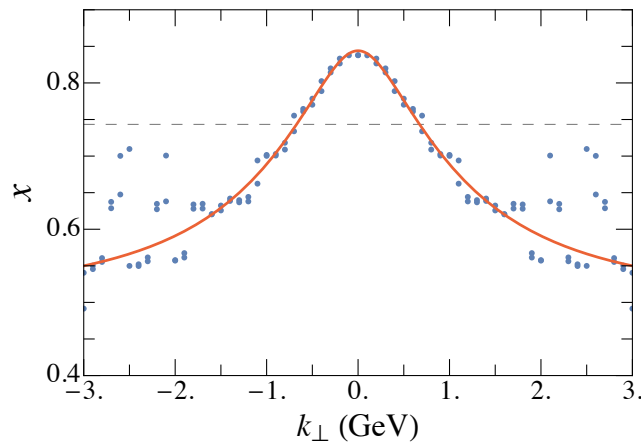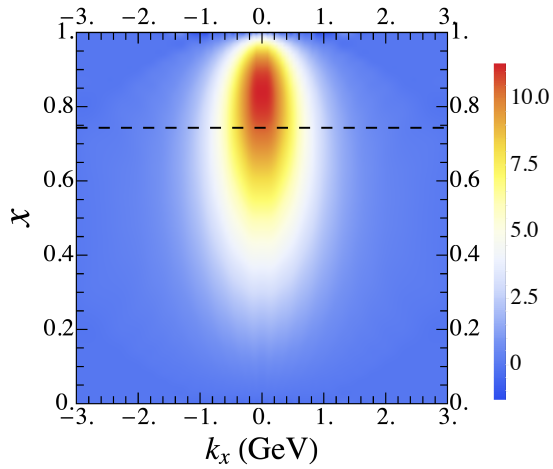
(c) B (b$\bar{\text{u}}$)

(d) D (c$\bar{\text{u}}$)

Figure 2.4: (continued)

fixed $k_\perp$ is given by

$$x = \left(1 + \sqrt{\frac{k_\perp^2 + m_q^2}{k_\perp^2 + m_Q^2}}\right)^{-1}. \tag{2.20}$$

This nontrivial dependence of the LFWF on the quark masses affects light-front observables such as the parton distribution function (PDF) and distribution amplitude (DA) as we will see in the following sections.

2.2.3 Decay Constant

The decay constants provide important information of the internal structure of the mesons. f_P and f_V are the decay constants of the pseudoscalar and vector mesons, which are defined from the matrix elements of the local electroweak current that annihilates the meson:

$$\begin{aligned}
\langle 0|\overline{\psi}\gamma^\mu\gamma_5\psi|P(p)\rangle &= -ip^\mu f_P, \\
\langle 0|\overline{\psi}\gamma^\mu\psi|V(p,m_j)\rangle &= e_{m_j}^\mu M_V f_V,
\end{aligned} \tag{2.21}$$

where p^μ is the four-momentum of the meson, M_V is the mass of the vector meson, and $e_{m_j}^\mu$ is the polarization vector. In this work, we choose the "good current" ($\mu = +$) together with the longitudinal polarization ($m_j = 0$) for the calculation [74]. These decay constants correspond to the LFWFs at the origin in coordinate space, and are expressed in the light-front representation as integral of LFWFs,

$$\frac{f_{P,V}}{2\sqrt{2N_c}} = \int_0^1 \frac{dx}{2\sqrt{x(1-x)}} \int \frac{d^2k_\perp}{(2\pi)^3} \psi_{\uparrow\downarrow\mp\downarrow\uparrow}^{(m_j=0)}(x,\vec{k}_\perp), \tag{2.22}$$

where the "minus" and "plus" signs correspond to pseudoscalar and vector states, respectively.

As mentioned before, the basis cutoff $N_{\max}$ is associated with the UV regulators ($b = \kappa$) by $\Lambda_{UV} \approx \kappa\sqrt{N_{\max}}$. Thus, all the observables that can be calculated through the integral of the LFWFs, including the decay constant, will be effected by the basis size. Fig. 2.5 is the LFWF of B_c that shows how the amplitude is associated with $N_{\max}$.

When calculating the decay constants, we employ different $N_{\max}$ values for different systems so that $\Lambda_{UV} \approx 0.85(m_q + m_{\bar{q}})$ in accordance with our previous work of heavy quarkonia [49]. This choice is motivated by the competition between the needs for both a better resolution on basis and
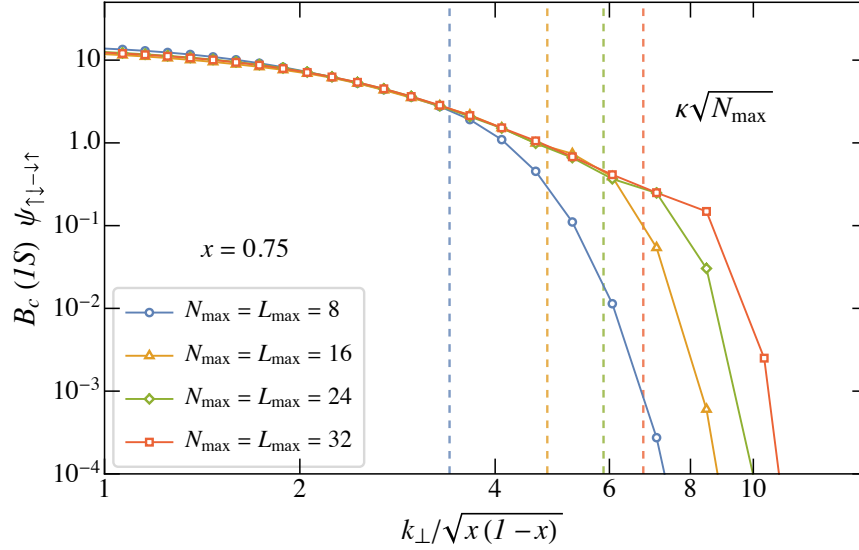
Figure 2.5: The LFWF amplitude of the dominant spin component of B_c, $\psi_{\uparrow\downarrow-\downarrow\uparrow}$ at $x = 0.75$ with respect to $k_\perp/\sqrt{x(1-x)}$. The vertical dashed lines indicate the values of $\kappa\sqrt{N_{\max}}$ for each basis cutoffs.

a lower UV scale since we omit the radiative corrections in our model. The specific choices of basis size for different systems are listed in Table 2.3.

Here we present the decay constants of the ground state pseudoscalar and vector of the unequal-mass mesons in Fig. 2.6, and compare with existing experiments and other published approaches [75–87]. In general our results are comparable with other sources, and the heavier systems seems to have a better agreement. However we notice our decay constants for the relatively lighter mesons, D and D_s, have a higher values than others. The immediate reason might be the excessive $N_{\max}$ basis we employed, which is hopefully to be solved via including higher Fock sectors.

Meanwhile, the difference of the decay constants of pseudoscalar and vector mesons is due to differences in the internal spin structures. In our work, f_P/f_V is greater than one for all the mesons, whereas the other theories such as QCD sum rule (QCDSR) favors a value less than one for heavy-light mesons, while a value greater than one for B_c. Details have been discussed in Refs. [76, 88–90]. As for BLFQ, even though the absence of chiral dynamics seems not to spoil the mass spectra of the heavy-light mesons, one could add an effective chiral potential in the Hamiltonian [91] as a

Table 2.3: In this table we list the values of $\kappa\sqrt{N_{\max}}$ of each system at different basis size. We choose those bases at which the $\kappa\sqrt{N_{\max}}$ values are marked in red for the calculation by comparing with $0.85(m_q + m_{\bar{q}})$ listed in the last row. Here $b\bar{u}$ and $b\bar{s}$, $c\bar{u}$ and $c\bar{s}$ share the same value because the limited difference in the mass between up and strange quark. Note that in $c\bar{u}/c\bar{s}$, one may consider $N_{\max} = 4$ as a better choice since it is closer to $0.85(m_q + m_{\bar{q}})$. However such basis size might be too small to retain reliable results. Therefore we choose $N_{\max} = 8$ for D and D_s mesons in the end as a trade-off.

$\kappa\sqrt{N_{\max}}$	$b\bar{b}$	$c\bar{c}$	$b\bar{c}$	$b\bar{u}/b\bar{s}$	$c\bar{u}/c\bar{s}$
$N_{\max} = 8$	3.92	2.78	3.40	3.02	2.30
$N_{\max} = 16$	5.57	3.92	4.81	4.28	3.23
$N_{\max} = 24$	6.81	4.76	5.88	5.23	3.94
$N_{\max} = 32$	7.86	5.47	6.77	6.04	4.53
$0.85(m_q + m_{\bar{q}})$	8.33	2.70	5.51	4.58	1.77

potential future work, in order to address the decay constant ratio of vector to pseudoscalar more extensively, as well as investigate the role of chiral effect in the heavy-light system.

2.2.4 Parton Distribution Function

The structure of hadrons, as probed in inclusive deep inelastic scattering (DIS) at large momentum transfer, can be described by the PDF $f(x; \mu)$. The PDF within collinear factorization defines the probability for finding a quark carrying a longitudinal momentum fraction x at resolution scale μ. In the LFWF representation, the PDF is calculated simply by integrating out the transverse momentum of the square of the wave function modulus,

$$f(x; \mu) = \frac{1}{4\pi x(1-x)} \sum_{s\bar{s}} \int^{\lesssim \mu^2} \frac{\mathrm{d}^2 k_\perp}{(2\pi)^2} \left| \psi_{s\bar{s}}(x, \vec{k}_\perp) \right|^2. \tag{2.23}$$

Within the two-body Fock sector truncation, the PDF is normalized to unity $\int_0^1 f(x; \mu)\mathrm{d}x = 1$, which relates to the orthonormal condition of the LFWFs (cf. Eq. (2.18)).

We study the PDFs of the heavy-light systems, and present the results of pseudoscalar and vector states in Fig. 2.7. The location of the peak reflects the asymmetry of the quark mass distribution in the heavy-light systems. Note that the peak of the PDFs is not at the quark mass fraction, due to the nontrivial behavior of the maxima in x along fixed $k_\perp$ in the LFWFs. We find
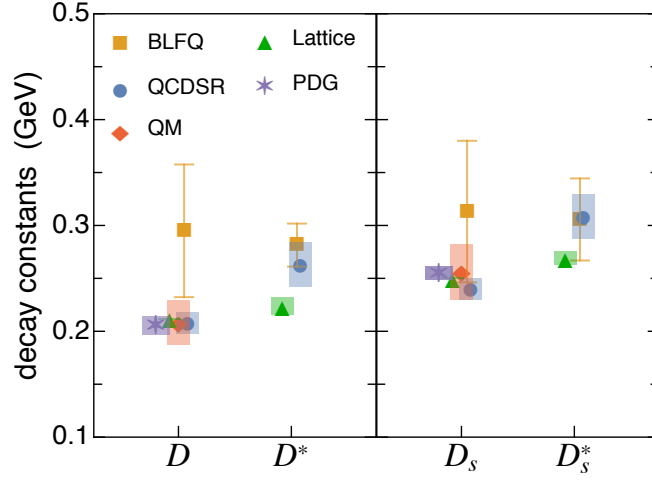
(a) Decay constant of D and D_s. We use $N_{\max} = 8$ as the central value for BLFQ, and the uncertainty bar is taken to be $\Delta_f = |f(N_{\max} = 8) - f(N_{\max} = 16)|$.
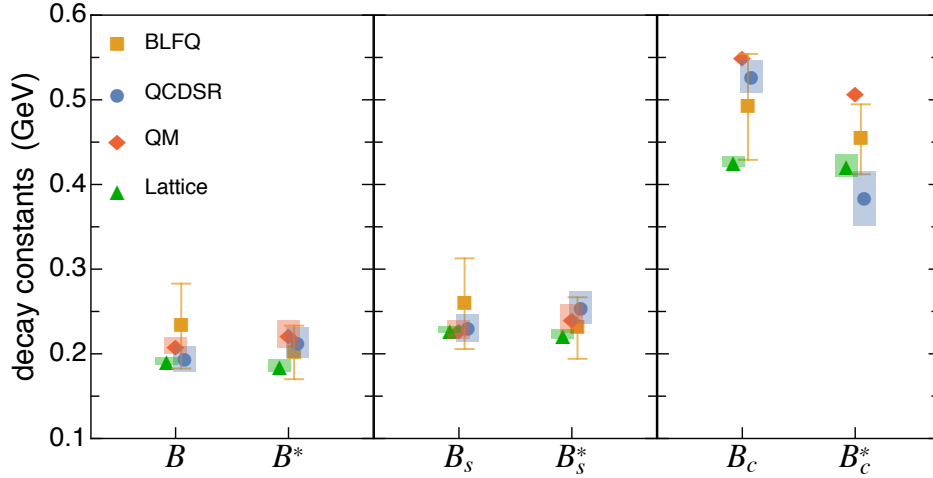
(b) Decay constant of B, B_s, and B_c. We use $N_{\max} = 16$ as the central value for B and B_s, where the uncertainty bar is taken to be $\Delta_f = |f(N_{\max} = 8) - f(N_{\max} = 16)|$; while for B_c, we use $N_{\max} = 24$, and the uncertainty bar $\Delta_f = 2|f(N_{\max} = 24) - f(N_{\max} = 32)|$.

Figure 2.6: Decay constant of pseudoscalar and vector states for the unequal-mass mesons.

that the peak in the PDF for the radial excited states 2^1S_0 and 2^3S_1 is at a significantly smaller value of x than that of 1^1S_0 and 1^3S_1, and in fact it is very close to $x = m_q/(m_q + m_{\bar{q}})$. This latter may be coincidental. The 2^1S_0 and 2^3S_1 states contain bumps on both sides of the peaks incorporating features arising from radial excitations. The difference between solid and dashed curves reveals the spin excitation. Those differences between 1^1S_0 and 1^3S_1 states are larger than between 2^1S_0 and 2^3S_1, that is due to the significant hyperfine splittings in lower excited states.

We use the basis size as $N_{\max} = L_{\max} = 32$ for these calculations, which corresponds to different resolution scales: $\mu_{D/D_s} \approx 4.5$ GeV, $\mu_{B/B_s} \approx 6.0$ GeV, and $\mu_{B_c} \approx 6.8$ GeV. The PDFs obtained here are only for valence partons with a low resolution where the valence Fock sector approximation is reasonable. Ref. [92] shows that combining the low resolution PDFs with the Dokshitzer-Gribov-Lipatov-Altarelli-Parisi (DGLAP) evolution provides access to experiment-relevant PDFs (valence, sea and gluon) at higher scales. We anticipate that DGLAP could also be applied to our results but that is beyond the scope of the present effort.

2.2.5 Distribution Amplitude

We also investigate another light-cone distribution that control the exclusive process at large momentum transfer, distribution amplitude (DA). DAs are defined from the lightlike vacuum-to-meson matrix elements and can be written with LFWFs as [93]

$$\frac{f_{P,V}}{2\sqrt{2N_c}}\phi_{P,V}(x) = \frac{1}{\sqrt{x(1-x)}} \int^{\lesssim \mu^2} \frac{\mathrm{d}^2 k_\perp}{2(2\pi)^3} \psi_{\uparrow\downarrow\mp\downarrow\uparrow}^{(m_j=0)}(x, \vec{k}_\perp), \tag{2.24}$$

with $f_{P(V)}$ the decay constants for pseudoscalars and vectors, respectively. They are associated with the minus and plus signs in the subscript of the wave function. Like in the PDF, we have the UV cutoff μ taken as $\mu \approx \kappa\sqrt{N_{\max}}$ in the basis representation. Note that in these definitions, DAs are normalized to unity. We compare the DAs of five mesons in Fig. 2.8.

Noticeably, DAs share some features with the PDFs: the DA spreads wider along x in the lighter system as it is more relativistic; dips in 2^1S_0 and 2^3S_1 states reflect their character as radial excitations; the discrepancy between pseudoscalar and vector which is caused by the different spin configuration mixing appears more significant in lower exited states; and lastly, the asymmetries
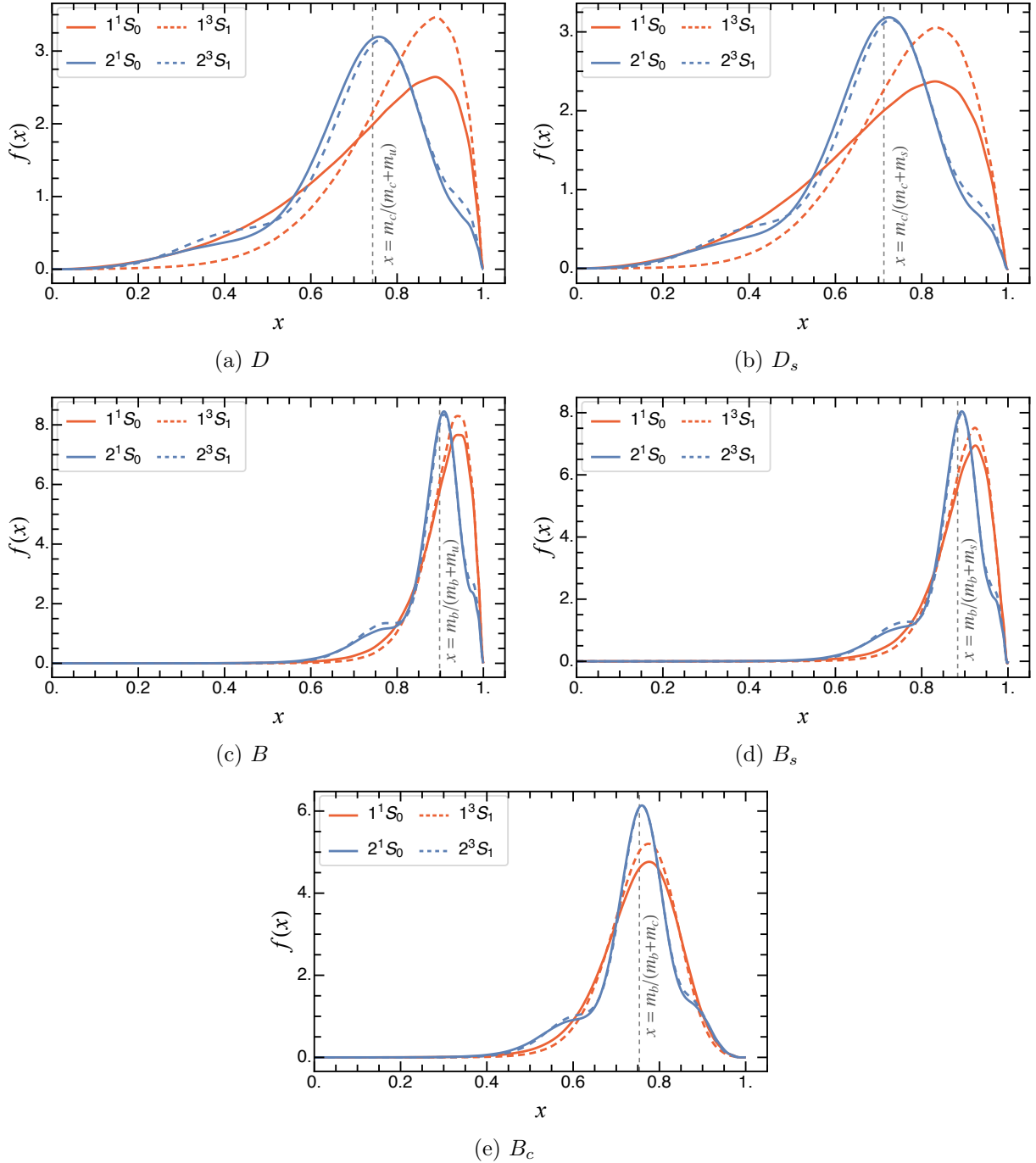
Figure 2.7: PDFs of pseudoscalar (solid curves) and vector (dashed curves) states of the heavy-light systems at $N_{\max} = L_{\max} = 32$, which is equivalent to the UV regulators $\mu_{D/D_s} \approx 4.5$ GeV, $\mu_{B/B_s} \approx 6.0$ GeV, and $\mu_{B_c} \approx 6.8$ GeV. The vertical dashed gray lines indicate the mass fraction of the quark, $x = m_q/(m_q + m_{\bar{q}})$.

shown in the unequal-mass meson DAs. However, different from PDFs, the DAs of the ground state (1^1S_0) peaked approximately at the quark mass fraction $x = m_q/(m_q + m_{\bar{q}})$. Noticeable wiggles that appear in DAs especially of B and B_s are due to the limited range of basis spaces employed. Similar patterns are also found in the light system [91], and are understood to be resolved by increasing the basis size. We find interesting similarities as well as differences of the DAs with the Dyson-Schwinger equation approach [94]. For example, the DAs of our D and D_s ground states are more widely spread in x. On the other hand, the peak heights of our DAs are very similar to the corresponding DAs in Ref. [94].

2.2.6 Charge and Longitudinal Momentum Densities

In this section we study the charge (longitudinal momentum) density in the transverse impact parameter space of the mesons. By definition, they are the two-dimensional Fourier transform of the charge form factor $F_1(q^2)$ and the gravitational form factor $A(q^2)$, respectively [95, 96]

$$
\begin{aligned}
\rho_c(\vec{b}_\perp) &= \int \frac{\mathrm{d}^2\Delta_\perp}{(2\pi)^2} e^{\mathrm{i}\vec{\Delta}_\perp \cdot \vec{b}_\perp} F_1(q^2 = -\vec{\Delta}_\perp^2), \\
\rho_g(\vec{b}_\perp) &= \int \frac{\mathrm{d}^2\Delta_\perp}{(2\pi)^2} e^{\mathrm{i}\vec{\Delta}_\perp \cdot \vec{b}_\perp} A(q^2 = -\vec{\Delta}_\perp^2),
\end{aligned}
\tag{2.25}
$$

where $\vec{\Delta}_\perp$ is the transverse momentum transfer, $\vec{b}_\perp \triangleq (1-x)\vec{r}_\perp$ is Burkardt's impact parameter [97], that can also be interpreted as the conjugated position of $\vec{\Delta}_\perp$ at which the current probes the charge density. The charge form factor $F_1(q^2)$ is associated with the matrix element of the current operator J^μ, while the gravitational form factor $A(q^2)$ corresponds to the stress-energy tensor $T^{\mu\nu}$. In the LFWF representation of the two-body ($q\bar{q}$) approximation, these densities can be expressed as,

$$
\begin{aligned}
\rho_c(\vec{b}_\perp) &= e_q \sum_{s,\bar{s}} \int_0^1 \frac{\mathrm{d}x}{4\pi(1-x)^2} \left|\widetilde{\psi}_{s\bar{s}}\left(x, \frac{-\vec{b}_\perp}{1-x}\right)\right|^2 + e_{\bar{q}} \sum_{s,\bar{s}} \int_0^1 \frac{\mathrm{d}x}{4\pi x^2} \left|\widetilde{\psi}_{s\bar{s}}\left(x, \frac{-\vec{b}_\perp}{1-x}\right)\right|^2, \\
\rho_g(\vec{b}_\perp) &= \sum_{s,\bar{s}} \int_0^1 \frac{\mathrm{d}x}{4\pi} \frac{x}{(1-x)^2} \left|\widetilde{\psi}_{s\bar{s}}\left(x, \frac{-\vec{b}_\perp}{1-x}\right)\right|^2 + \sum_{s,\bar{s}} \int_0^1 \frac{\mathrm{d}x}{4\pi} \frac{1-x}{x^2} \left|\widetilde{\psi}_{s\bar{s}}\left(x, \frac{-\vec{b}_\perp}{1-x}\right)\right|^2,
\end{aligned}
\tag{2.26}
$$

where $\widetilde{\psi}_{s\bar{s}}(x, \vec{r}_\perp)$ is the LFWF in the coordinate space (cf. Eq. (2.13)). Each density is normalized to the unit charge of the system, which is zero or one, and the total longitudinal momentum, which is unity, of the meson, respectively.
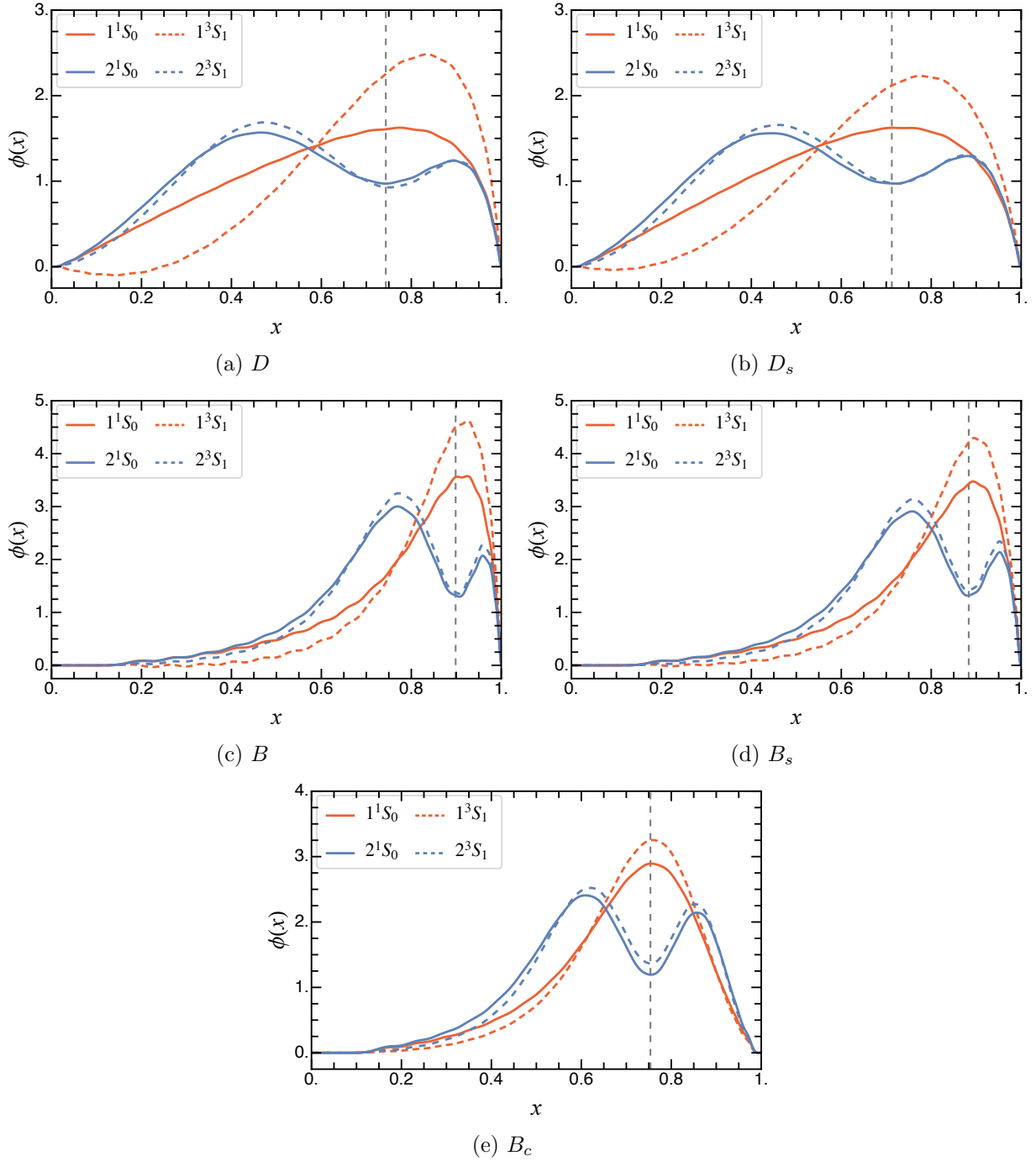
Figure 2.8: DAs of pseudoscalar (solid curves) and vector (dashed curves) states of the heavy-light systems at $N_{\max} = L_{\max} = 32$. The vertical dashed gray lines is at $x = m_q/(m_q + m_{\bar{q}})$.

The momentum density is more concentrated in the center than the charge density, where the difference is a relativistic effect [49]. This pattern can be observed in Fig. 2.9, where we present the results of pseudoscalar and scalar states of the unequal-mass mesons. There are unexpected humps shown in the densities for the P-waves (middle panels) of D and D_s. Similar situations are also noticed at small $N_{\max}$ for other systems, but are resolved by enlarging the basis size. This indicates that to obtain more reliable results for the charge and longitudinal momentum densities of D and D_s, one should apply higher basis cutoffs.

(a) B_c

(b) B_s

(c) B

Figure 2.9: The charge density and longitudinal momentum density on the transverse plane of the pseudoscalar and scalar states.

(d) D_s
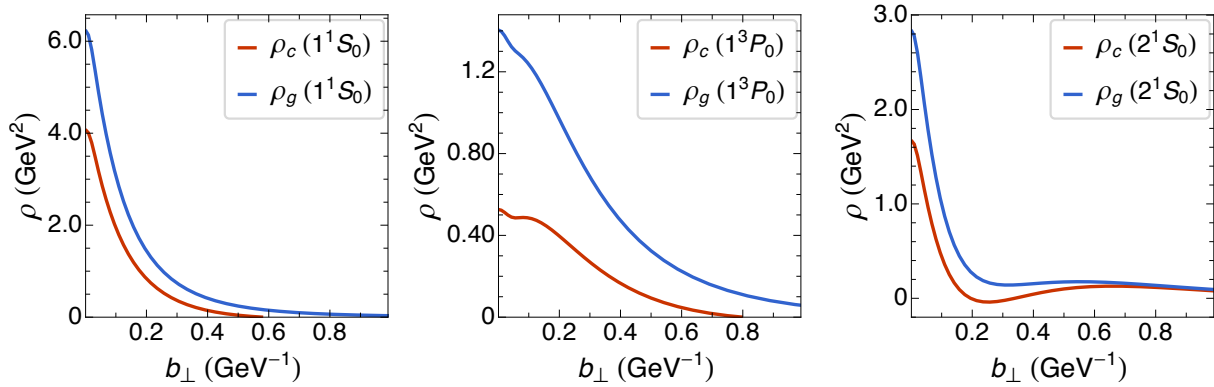
(e) D

Figure 2.9:   (continued)

CHAPTER 3.   WEAK DECAY OF HEAVY MESONS

Paper in preparation

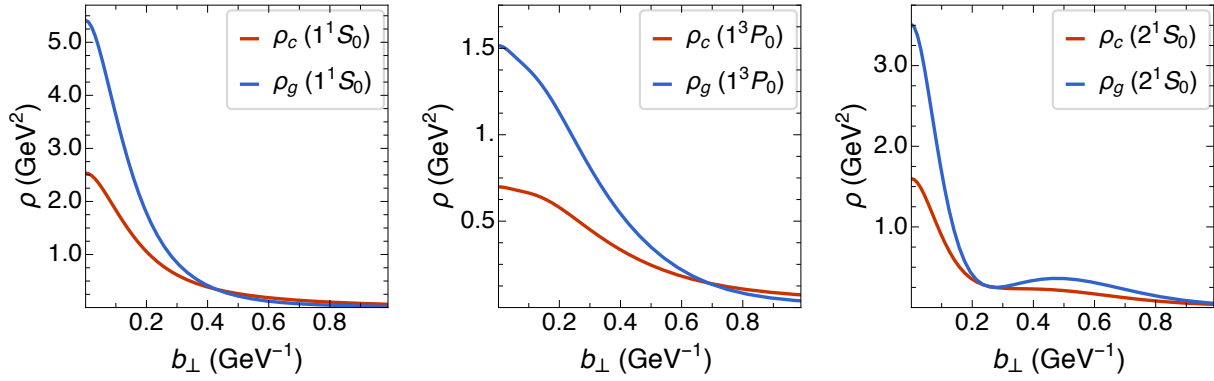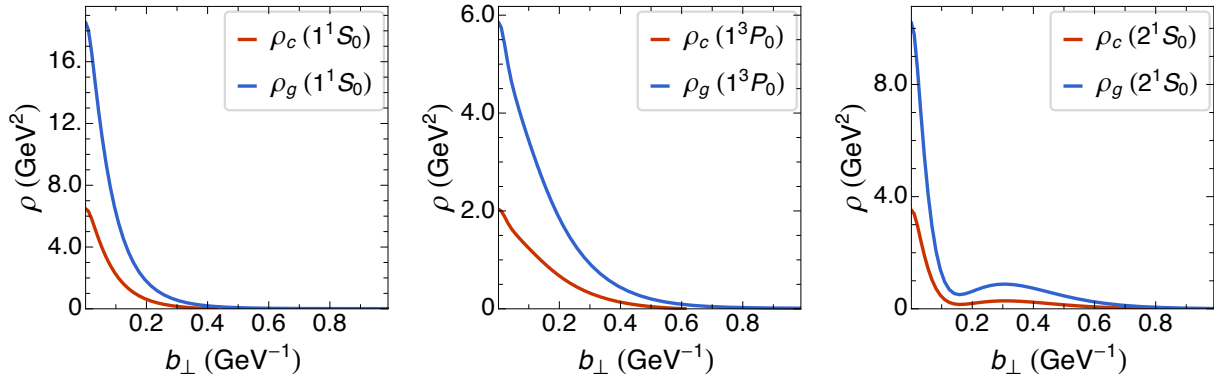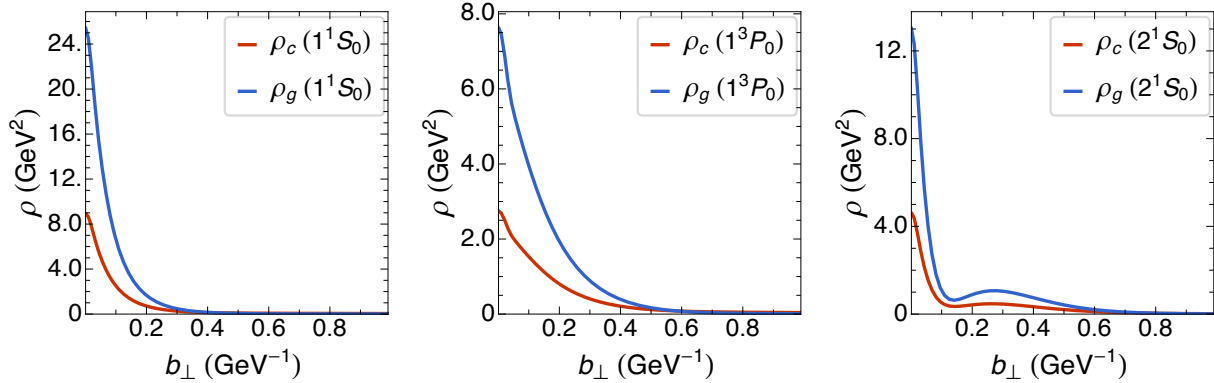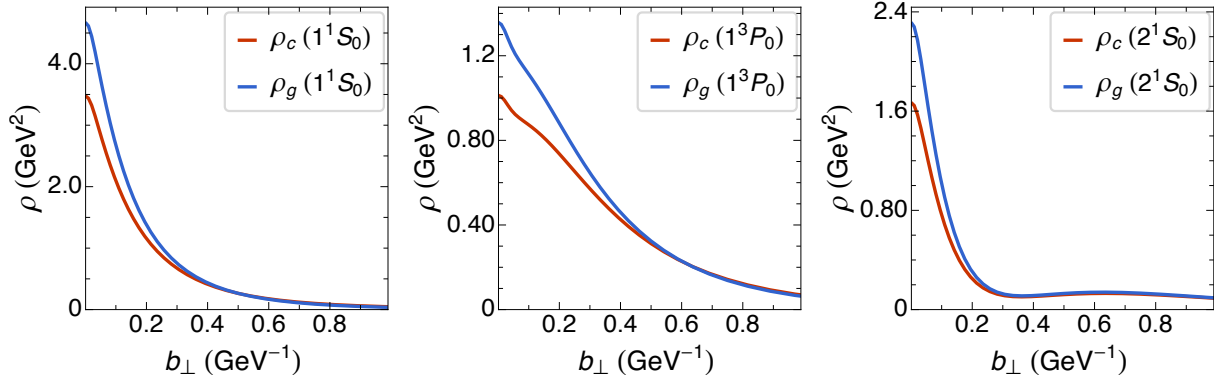Shuo Tang, Shaoyang Jia, Pieter Maris, and James P. Vary

3.1   Abstract

We study the semileptonic decay of the $B_c(0^-)$ to charmonium through the bottom-to-charm-quark electroweak current in the framework of basis light-front quantization (BLFQ). Explicitly, we calculate the differential decay width and the electroweak form factors for processes of B_c decays into η_c or J/ψ using the corresponding initial and final wave functions obtained from BLFQ. We analyze the frame dependence of these observables and conclude with a preference for frames that minimize the sensitivity of the results to sub-dominant components of the light-front amplitudes.

3.2   Introduction

Precise measurement of elements $|V_{q_1 q_2}|$ in the Cabibbo-Kobayashi-Maskawa (CKM) matrix is crucial to our understanding of the electroweak theory. Among these elements the determination of $|V_{ub}|$ and $|V_{cb}|$ lead to a central test of the Standard Model for heavy-flavor physics. Although the pure leptonic decay such as $B_c \to \tau\bar{\nu}$ is theoretically simple, information from this process is not included in the determination of the CKM matrix due to the lack of accuracy in measurements. Instead, the inclusive and exclusive semileptonic decays are employed. Meanwhile, recent experiments observed anomalies in the decays of $\overline{B} \to D^{(*)}\tau\bar{\nu}$ and $B_c \to J/\psi\tau\bar{\nu}$ [98–104], which could be an indication of new physics beyond the standard model. These results stimulate elevated efforts to investigate the process of semileptonic decays of the B and B_c mesons.

Investments have been made in studying the semileptonic decay of B_c with various theoretical approaches. However, one existing difficulty in calculating form factors for the semileptonic decay

(a) conserving particle number: $2 \to 2$ (b) changing particle number: $4 \to 2$
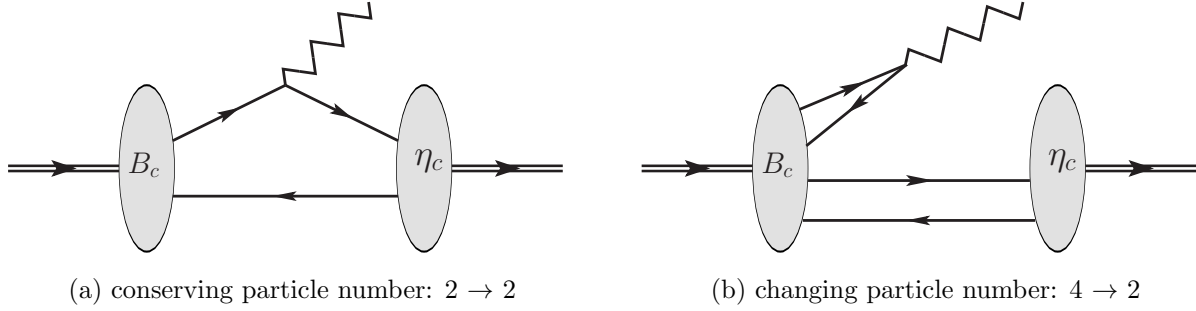
Figure 3.1: Diagrams of two dominant contributions to the transition $B_c \to \eta_c$ in the light-front time order (left to right).

on the light front is that the physically allowed region of the transferred momentum square q^2 is timelike. A traditional choice of the Drell-Yan frame is not applicable since it only grants access to the spacelike region. Therefore, one needs either to apply analytical continuation to reach the timelike region, or use a factorization approach that introduces extra parameters [105–114]. Meanwhile, since the mass difference in $B_c \to \eta_c(J/\psi)\ell\bar{\nu}_\ell$ ($\ell = e$, μ, and τ) is rather large, it is technically difficult for some of the theories to reach the zero-recoil point of $q^2_{\max} = (M_{B_c} - M_{\eta_c(J/\psi)})^2$. In this work, we employ a special kinematic frame on the light front that allows us to compute the form factors in the timelike region up to $q^2_{\max}$.

Previously, we have studied the heavy meson systems [48, 49, 53] in the BLFQ framework, which showed success in predicting the mass spectrum and in producing reasonable light-front wave functions (LFWFs) within the valence quark Fock sector ($|q\bar{q}\rangle$). With the LFWFs in hand, one can calculate the observables of interest, such as the parton distribution functions, charge radii, electromagnetic form factors, by integrating the wave functions properly in the light-front representation. But as mentioned in Refs. [115, 116], the LFWFs of the valence Fock sector only allow us to study the decay process where the particle number is conserved, which is referred to as the leading-order Feynman diagram (Fig. 3.1a). On the other hand, the contribution of the particle-number-changing diagrams, which involves Fock sectors higher than the valence such as Fig. 3.1b, are not yet available in BLFQ.

In principal, form factors are Lorentz invariants and therefore independent of the reference frames. However we observe frame dependence of form factors that has also been discussed in the literature [79, 105], which is ascribed to the Fock space truncation. As more Fock sectors are considered, the frame dependence is expected to be reduced [24, 25]. In this work we retain only the valence Fock sector of mesons and seek a certain frame where errors due to omitting higher Fock sector are minimized.

We organize this paper as follows: in Sec. 3.3 we discuss the semileptonic decay on the light front, and introduce two Lorentz invariants to describe the light-front kinematics. Then we present the calculated results in Sec. 3.4 where we also compare with several other approaches. Sec. 3.6 contains our conclusion with proposed potential future improvements.

3.3   Semileptonic Decays and Light-Front Kinematics

The hadron matrix element describing the electroweak decays of B_c ($b\bar{c}$) ground state is given by

$$\mathcal{M}_h^\mu = \langle P_2, m_j | V^\mu - A^\mu | P_1 \rangle, \tag{3.1}$$

where P_1 and P_2 are the 4-momentum of the initial and final states. Here m_j is the angular momentum projection of the daughter meson. V^μ and A^μ are the vector and axial-vector currents, respectively. In particular, we consider the $b \to c$ decay via the emission of W^- boson. The hadron current defined by Eq. (3.1) can be parameterized by a set of form factors as functions of Lorentz invariant q^2, where $q^\mu = (P_1 - P_2)^\mu$ is the momentum transfer between the initial and final hadrons with $q^\mu = (q^+, \vec{q}_\perp, q^-) = (q^0 + q^3, q^1, q^2, q^0 - q^3)$ on the light front. When the final state is a pseudoscalar meson [117], we have

$$
\begin{aligned}
\langle P_2 | A^\mu | P_1 \rangle &= \langle P_2 | \bar{c} \gamma^\mu \gamma_5 b | P_1 \rangle = 0; \\
\langle P_2 | V^\mu | P_1 \rangle &= \langle P_2 | \bar{c} \gamma^\mu b | P_1 \rangle = f_+(q^2) P^\mu + f_-(q^2) q^\mu,
\end{aligned}
\tag{3.2}
$$

where $P^\mu \triangleq (P_1 + P_2)^\mu$. Alternative to Eq. (3.2), another widely used expression for the matrix element is associated with $f_+(q^2)$ and $f_0(q^2)$, where f_0 is the linear combination of f_+ and f_-:

$$f_0(q^2) = f_+(q^2) + \frac{q^2}{M_1^2 - M_2^2} f_-(q^2), \tag{3.3}$$

with M_1 and M_2 denoting mother and daughter meson masses, respectively. These form factors correspond to the transition amplitude with 1^- and 0^+ spin-parity in the center of mass of the lepton pair. The differential decay width for the exclusive $P \to P\ell\bar{\nu}_\ell$ process is then expanded as [118]

$$\frac{d\Gamma(P \to P\ell\bar{\nu}_\ell)}{dq^2}$$
$$= \frac{G_F^2 |V_{cb}|^2}{24\pi^3} K(q^2) \left(1 - \frac{m_\ell^2}{q^2}\right)^2 \left\{ K^2(q^2) \left(1 + \frac{m_\ell^2}{2q^2}\right) |f_+(q^2)|^2 + M_1^2 \left(1 - \frac{M_2^2}{M_1^2}\right)^2 \frac{3m_\ell^2}{8q^2} |f_0(q^2)|^2 \right\}. \tag{3.4}$$

In the expression above we take into account of the lepton mass m_ℓ. $|V_{cb}|$ is proper element of the CKM mixing matrix, G_F is the Fermi coupling constant, and $K(q^2)$ is the kinematic factor given by

$$K(q^2) = \frac{1}{2M_1} \sqrt{(M_1^2 + M_2^2 - q^2)^2 - 4M_1^2 M_2^2}. \tag{3.5}$$

In the case with the vector state final state, both vector and axial-vector current matrices are nonzero:

$$\langle P_2, m_j | V^\mu | P_1 \rangle = \langle P_2, m_j | \bar{c}\gamma^\mu b | P_1 \rangle = ig(q^2)\varepsilon^{\mu\nu\alpha\beta} \epsilon_\nu^* P_\alpha q_\beta;$$
$$\langle P_2, m_j | A^\mu | P_1 \rangle = \langle P_2, m_j | \bar{c}\gamma^\mu\gamma_5 b | P_1 \rangle = f(q^2)\epsilon^{*\mu} + a_+(q^2)(\epsilon^* \cdot P)P^\mu + a_-(q^2)(\epsilon^* \cdot P)q^\mu, \tag{3.6}$$

where $\epsilon^* = \epsilon^*(P_2, m_j)$ is the polarization vector of the final meson that satisfies the Lorentz condition $\epsilon^*(P_2, m_j) \cdot P_2 = 0$. These form factors defined in Eq. (3.6) are often alternatively given by the Bauer-Stech-Wirbel (BSW) convention [119, 120]

$$V(q^2) = (M_1 + M_2)g(q^2),$$
$$A_1(q^2) = \frac{f(q^2)}{M_1 + M_2},$$
$$A_2(q^2) = -(M_1 + M_2)a_+(q^2), \tag{3.7}$$
$$A_0(q^2) = \frac{1}{2M_2} \left[f(q^2) + (M_1^2 - M_2^2)a_+(q^2) + q^2 a_-(q^2) \right].$$

Then the differential decay width characterizing the $P \to V\ell\bar{\nu}_\ell$ process can be expressed as

$$\frac{\mathrm{d}\Gamma(P \to V\ell\bar{\nu}_\ell)}{\mathrm{d}q^2} = \frac{G_F^2 |V_{cb}|^2}{48\pi^3} K(q^2) \left(1 - \frac{m_\ell^2}{q^2}\right)^2 \left\{ \left(1 + \frac{m_\ell^2}{2q^2}\right) \left[\left(1 + \frac{M_2}{M_1}\right)^2 q^2 |A_1(q^2)|^2 \right.\right.$$

$$+ \frac{1}{2M_1^2 M_2^2} \left| \frac{1}{2}(M_1^2 - M_2^2 - q^2)(M_1 + M_2)A_1(q^2) - \frac{2K^2(q^2)M_1^2}{M_1 + M_2} A_2(q^2) \right|^2 \qquad (3.8)$$

$$\left.\left. + \frac{4q^2 K^2(q^2)}{(M_1 + M_2)^2} |V(q^2)|^2 \right] + \frac{3m_\ell^2}{q^2} K^2(q^2)|A_0(q^2)|^2 \right\}.$$

To describe the kinematics of the decay process, we introduce two boost invariants z and $\vec{\Delta}_\perp$ for the Lorentz invariant momentum transfer squared q^2 [115] such that

$$q^2 = z\left(M_1^2 - \frac{M_2^2}{1-z}\right) - \frac{\Delta_\perp^2}{1-z}. \qquad (3.9)$$

Specifically, z is the relative momentum transfer in the longitudinal direction, and is limited in the kinematical region $0 \le z < 1$. Meanwhile, $\vec{\Delta}_\perp$ denotes the momentum transfer in the transverse direction:

$$z = \frac{q^+}{P_1^+}, \qquad \vec{\Delta}_\perp = \vec{q}_\perp - z\vec{P}_{1\perp}. \qquad (3.10)$$

Note that in Eq. (3.9) q^2 is not a monotonic function with respect to z, therefore at fixed q^2 there are different $(z, \vec{\Delta}_\perp)$ combinations related to different frames. Among them, two special frames are most favored:

- Drell-Yan frame: $q^+ = 0$ ($z = 0$). This frame is widely adopted in light-front dynamics, especially working in combination with the "good current" J^+. This combination has the advantage of suppressing the vacuum pair production/annihilation shown in Fig. 3.1b [121–123]. However, by choosing the Drell-Yan frame, one can only access the spacelike region. While in the case of the semileptonic decay of hadrons, the physically allowed region of q^2 is timelike. For this reason, authors often apply analytical continuation by replacing $\vec{q}_\perp$ with $i\vec{q}_\perp$, or use factorization to access timelike region.

- Longitudinal frame: $\vec{\Delta}_\perp = 0$. This frame covers both timelike and spacelike regions. Furthermore, it is the only frame that can access the zero recoil point, i.e. $q_{\max}^2 = (M_1 - M_2)^2$ (see Fig. 3.2). Only at this point is $z = 1 - M_2/M_1$ unique. Unlike the Drell-Yan frame
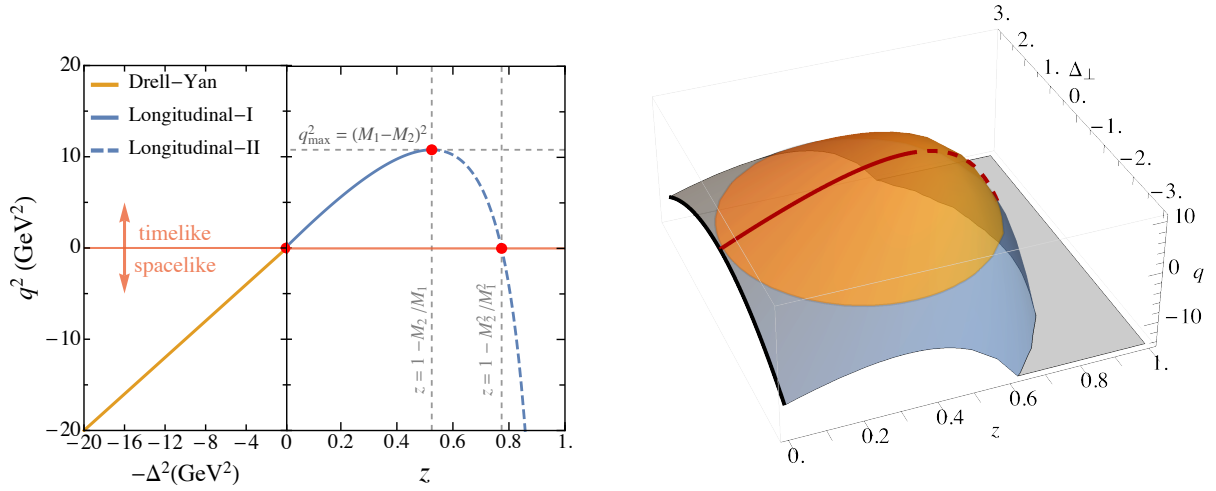
Figure 3.2: **left panel:** We present the Lorentz invariant q^2 as a function of z or $\Delta_\perp^2$ in two special frames. In the Drell-Yan frame ($z = 0$), momentum transfer $q^2 = -\Delta_\perp^2$. In the longitudinal frame ($\Delta_\perp = 0$), $q^2 = z[M_1^2 - M_2^2/(1-z)]$. Note that in this 2D plot we put the two regions with different frames together only for the sake of visualization, they have different variables and scales on the horizontal axis.

right panel: The 3D plot of q^2 in terms of z and $\Delta_\perp$. All q^2 values that are in the physically allowed region are situated on the convex surface and correspond to a pair of $(z, \Delta_\perp)$. The yellow area shows the timelike region, while the blue area is spacelike. The black curve corresponds to the Drell-Yan frame, the solid red curve represents the longitudinal-I frame, and the dashed red curve (which drops out of sight over the peak of the convex surface) traces the longitudinal-II frame.

where q^2 is monotonic on $\Delta_\perp^2$, the longitudinal frame has two branches that suggests two z values contributing to the same q^2 (except $q_{\max}^2$) in the timelike region: $z = [M_1^2 - m_2^2 + q^2 \pm \sqrt{(M_1^2 - M_2^2 + q^2)^2 - 4M_1^2 q^2}]/(2M_1^2)$. Thus we treat them as two different frames. The branch connected to the Drell-Yan frame at $q^2 = 0$ is named longitudinal-I frame, through which one can only access the timelike region. The other branch, named the longitudinal-II frame, starts at the limit $q_{\max}^2$ and continues through the entire spacelike region.

Aside from these special frames, all other combinations of z and $\Delta_\perp$ on the convex surface compose the general frames. In the following section, we will discuss the variations in the form factors arising from the Fock space truncation in our model that are visible by different frame choices.

3.4   Numerical Results

3.4.1 $B_c \to \eta_c \ell \bar{\nu}_\ell$

In Eq. (3.2), the hadron matrix element of the vector current is associated with two independent form factors. We therefore employ two current components, $\mu = +$ and $\mu = R$, for practical calculation. The R component of a vector is defined by $x^R \triangleq x^1 + \mathrm{i}x^2$; similarly the L component is $x^L \triangleq x^1 - \mathrm{i}x^2$. We do not use the $\mu = -$ component as it violates charge conservation. Then the two form factors can be written in terms of the matrix elements and the two boost invariants:

$$
\begin{aligned}
f_+(q^2) &= \frac{(\Delta^R + zP_1^R)\mathcal{M}^+ - zP_1^+ \mathcal{M}^R}{2\Delta^R P_1^+}, \\
f_-(q^2) &= \frac{\left[\Delta^R - (2-z)P_1^R\right]\mathcal{M}^+ + (2-z)P_1^+ \mathcal{M}^R}{2\Delta^R P_1^+}.
\end{aligned}
\tag{3.11}
$$

The matrix element $\mathcal{M}^{+(R)} \triangleq \langle P_2|\bar{c}\gamma^{+(R)}b|P_1\rangle$ can then be calculated according to

$$
\begin{aligned}
\mathcal{M}^\mu = \sum_{s\bar{s}} \int \frac{\mathrm{d}x}{2x(1-x)} \int \frac{\mathrm{d}\vec{k}_\perp}{(2\pi)^3} \sum_{s'} \frac{1-z}{x-z} \bar{u}_{s'}\left(p'\right) \gamma^\mu u_s(p) \\
\times \psi_{s'\bar{s}/\eta_c}^{*(m_j=0)}\left(\frac{x-z}{1-z}, \vec{k}_\perp - \frac{1-x}{1-z}\vec{\Delta}_\perp\right) \psi_{s\bar{s}/B_c}^{(m_j=0)}(x, \vec{k}_\perp),
\end{aligned}
\tag{3.12}
$$

where $p = \left(xP_1^+, \vec{k}_\perp + x\vec{P}_{1\perp}\right)$ and $p' = \left((x-z)P_1^+, \vec{k}_\perp + (x-z)\vec{P}_{1\perp} - \vec{\Delta}_\perp\right)$ are the 3-momentum of the initial quark (b) and final antiquark ($\bar{c}$) associated with the spinor $u_s/\bar{u}_{s'}$. Details of the LFWFs $\psi(x, \vec{k}_\perp)$ expanded within the BLFQ basis representation are given in Eq. (2.11), and tables of the spinor matrix components for our applications are provided in Appendix A.2.

We present the results of f_+ and f_0 obtained with different frames in Fig. 3.3, where we sample the q^2 with respect to multiple $\Delta_\perp$ and z pairs. The constraint $z = 0$ selects the Drell-Yan frame which exists only for $q^2 \leq 0$. It is connected with the longitudinal-I frame (lower branch of the longitudinal frame curve) at $q^2 = 0$. However the "kink" at the connecting point (visible if one looks closely at that connecting point) suggests that the derivative is not continuous at the boundary of the two frames, indicating the need of caution when applying the analytical continuation from spacelike to timelike region. The difference of the form factors between different frames is referred to as the frame dependence. Noticeably, the special frames (Drell-Yan, longitudinal-I, and
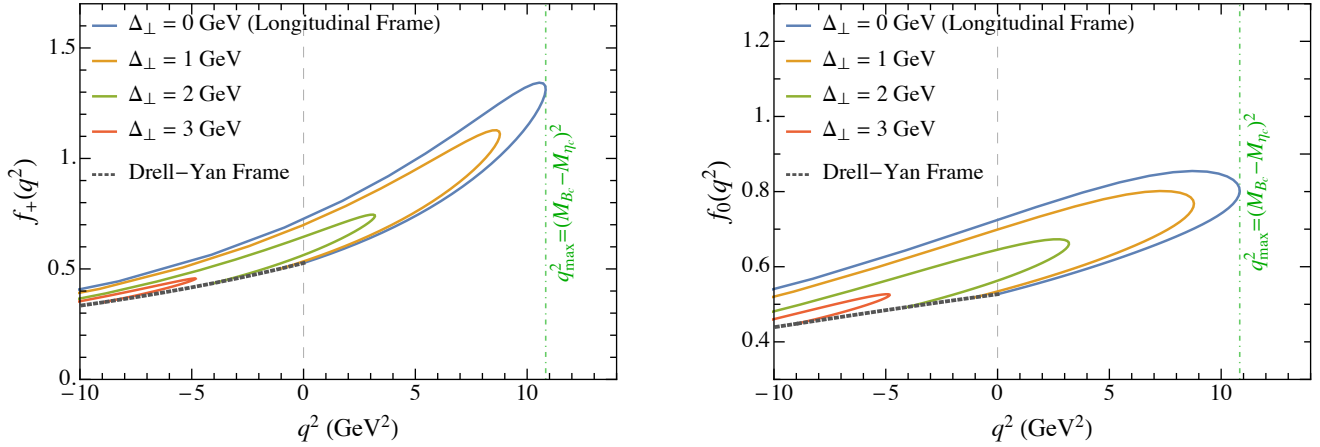
Figure 3.3: The frame dependence of the form factors for $B_c \to \eta_c \ell \nu_\ell$ decay at the basis size $N_{\max} = L_{\max} = 8$. The black dots indicate the form factors obtained with the Drell-Yan frame, the solid blue curve is from the longitudinal frame, and the other curves are obtained with both non-zero z and $\Delta_\perp$ which we call the general frames. For $f_+(q^2)$ and $f_-(q^2)$, the two special frames form a boundary enclosing form factors obtained from the general frames.

longitudinal-II) form a boundary surrounding the other points in the equal-q^2 contour in the general frame (combination of nonzero z and $\Delta_\perp$). This statement is more firm in the timelike region, however it does not hold in the spacelike region, since we have observed scenarios where the results from the Drell-Yan frame intersect those of longitudinal-II frame at a specific q^2.

Next we check the basis cutoff dependence of the form factors. We estimate that the infrared (IR) and ultra-violet (UV) regulators correspond to the basis cutoffs as $\lambda_{\mathrm{IR}} \approx \kappa/\sqrt{N_{\max}}$ and $\lambda_{\mathrm{UV}} \approx \kappa\sqrt{N_{\max}}$. Here $N_{\max}$ sets the cutoffs of the transverse basis functions, and κ is the confining strength, the value of which is given in Refs. [49, 53]. While the cutoff of the longitudinal basis $L_{\max}$ is taken to be the same as $N_{\max}$ for all the LFWFs we employ in this paper. The hadron matrix elements as the overlaps of LFWFs are affected by these cutoffs. Aside from electroweak form factors, other observables such as the decay constant, elastic form factor, and radiative transition form factors that also show dependence on basis cutoff as we have shown previously [53, 54, 74, 115, 116]. In order to have a clear impression on how basis size affects the form factors, we only include the special frames with basis cutoffs $N_{\max} = L_{\max} = 8$, 16, 24, 32 in Fig. 3.4. In general the frame dependence becomes stronger with a larger basis size arising primarily from a more
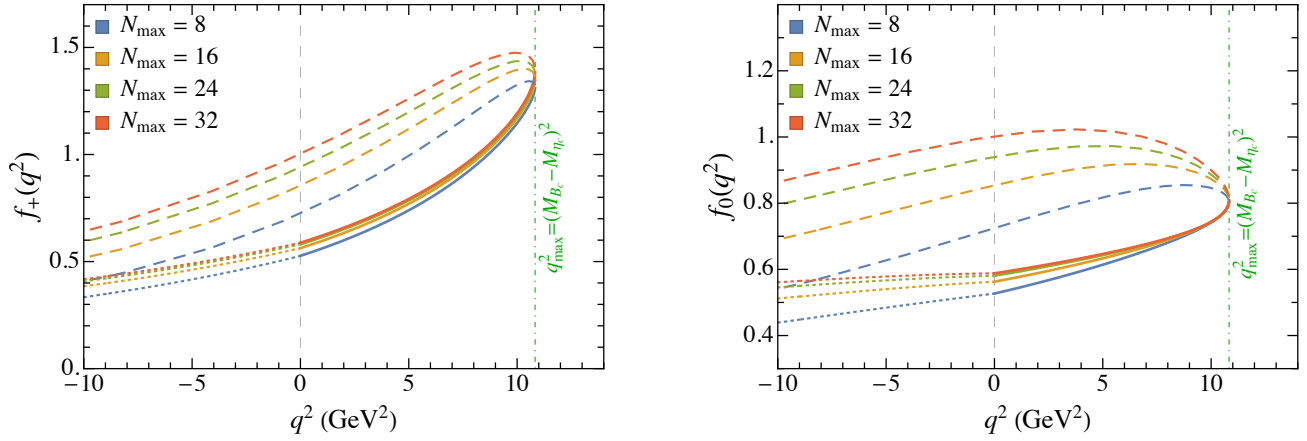
Figure 3.4: The dependence of the form factors on the basis size. We present the form factors calculated in the Drell-Yan frame with the dots; results in the longitudinal-I and longitudinal-II frames are shown with solid and dashed curves, respectively.

significant increase in the results of the longitudinal-II branch compared with the Drell-Yan and longitudinal-I branches. The overall tendency appears to be counterintuitive since larger basis size usually reduces the frame dependence in other applications [115, 116]. We recall that the role of the omitted Z-diagram is suppressed by keeping to low z. Hence, it is natural to expect that, in our application, the Drell-Yan and longitudinal-I frames which have minimal z values are preferred since they would suppress the contribution from the Z-diagram [116]. It is therefore appealing that the smaller sensitivity to basis space cutoff of these two frames implies that they may be the preferred frames for calculations with the currently available LFWFs.

In Table 3.1, we list the numerical values of the form factors at the kinematical limits, namely $q^2 = 0$ and $q^2_{\max}$ at $N_{\max} = L_{\max} = 32$. We also provide results from other approaches for comparison. In general, the result with longitudinal-I frame shows better agreement with other approaches. This is encouraging in light of our discussion above concerning the minimization of effects of the neglected Z-diagram with the longitudinal-I frame.

In Fig. 3.5, we provide the result of the differential decay width based on Eq. (3.4), specifically with the $B_c \to \eta_c e \bar{\nu}$ channel. Values of the lepton mass and the Fermi constant are taken from the

Table 3.1: Form factors calculated in this work within different frames (first two rows of the table) and with other methods. BLFQ - 1 and BLFQ - 2 at $q^2 = 0$ correspond to longitudinal-I and longitudinal-II frames, respectively. The central value is quoted using the LFWFs at the basis limits $N_{\max} = L_{\max} = 32$, while the uncertainties are quoted as $\varepsilon_f = 2|f_{N_{\max}=32} - f_{N_{\max}=24}|$ to show the basis sensitivity. Other methods listed in the table include perturbative QCD (pQCD), covariant confined quark model (CCQM), relativistic quark model (RQM), light-front quark model (LFQM), and Lattice QCD. For the LFQM, we quote the results with both linear potential and harmonic oscillator potential (in the bracket) from their model.

	$f_+(0) = f_0(0)$	$f_+(q^2_{\max})$	$f_0(q^2_{\max})$
BLFQ - 1	0.588(15)	1.391(41)	0.811(6)
BLFQ - 2	1.003(125)		
pQCD [110]	0.48	1.03	0.78
CCQM [111]	0.75	1.13	0.92
RQM [124]	0.47	1.07	0.92
LFQM [79]	0.482 [0.546]	1.084 [1.035]	0.876 [0.872]
Lattice [125]	0.59		

particle data group (PDG) [64],

$$m_e = 0.5109989461 \text{ MeV}; \qquad G_{\text{F}} = 1.1663787 \times 10^{-5} \text{ GeV}^{-2}. \tag{3.13}$$

The decay width also shows the same trend as in the form factors. To be specific, results with the longitudinal-I frame are less sensitive to basis sizes than those in longitudinal-II. In addition, the difference between two frames is most significant at low q^2. Thus, the tendency towards convergence of the decay width with increasing basis size using the longitudinal-I basis as shown in Fig. 3.5 over a wide range of q^2 provides additional support for the adoption of the longitudinal-I frame for all the observables we consider in this work.

3.4.2 $B_c \to J/\psi \ell \bar{\nu}_\ell$

The hadron matrices describing the semileptonic decay from B_c to the vector meson J/ψ have more intricate structures. For the vector current matrix element in Eq. (3.6), it takes a similar form as in the radiative decay between pseudoscalar and vector states. Based on a former study [74], a combination of the current component $\mu = R$ and the magnetic projection $m_j = 0$ of the LFWF
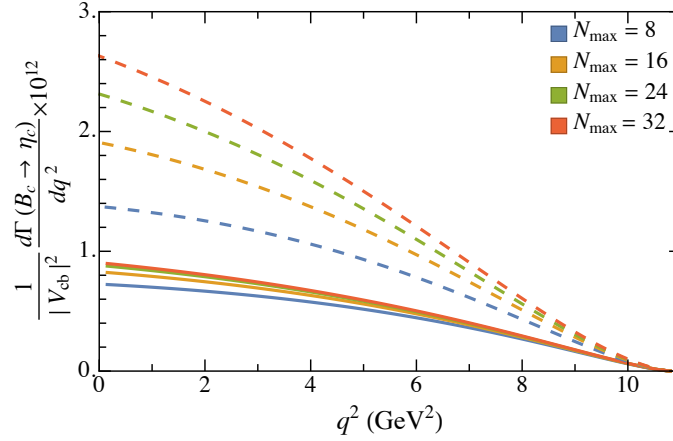
Figure 3.5: The differential decay width of semileptonic decay of $B_c \to \eta_c e\bar{\nu}$. Results are presented with longitudinal-I (solid) and longitudinal-II (dashed) frames at different basis cutoffs.

is favored for calculating the form factor $g(q^2)$ on the light front. Since this choice employs the dominant spin component of the LFWFs and ties in with the nonrelativistic limit of the heavy systems. Therefore we define the right component of the hadron matrix element

$$\mathcal{V}_0^R \triangleq \langle P_2, m_j = 0 | \bar{c}\gamma^R b | P_1 \rangle = -2\mathrm{i}M_2 \frac{\Delta^R}{1-z} g(q^2). \tag{3.14}$$

For the other three form factors corresponding to the axial current matrix, we employee $\mathcal{A}_0^+$, $\mathcal{A}_1^+$, and $\mathcal{A}_1^L$ for the calculation, where $\mathcal{A}_{m_j}^\mu \triangleq \langle P_2, m_j | \bar{c}\gamma^\mu\gamma_5 b | P_1 \rangle$. Again, we avoid using the "bad current" ($\mu = -$), which leads to a violation of the charge conservation in the leading Fock space. Then those form factors can be expressed as follows:

$$
\begin{aligned}
f(q^2) &= \frac{M_2}{(1-z)P_1^+}\mathcal{A}_0^+ + \frac{\Delta_\perp^2 - M_2^2 + (1-z)^2 M_1^2}{\sqrt{2}(1-z)P_1^+\Delta^L}\mathcal{A}_1^+, \\
a_+(q^2) &= (1-z)\frac{zP_1^+\mathcal{A}_1^L - \left(zP_1^L + \Delta^L\right)\mathcal{A}_1^+}{\sqrt{2}\left(\Delta^L\right)^2 P_1^+}, \\
a_-(q^2) &= (1-z)\frac{(z-2)P_1^+\mathcal{A}_1^L - \left[(z-2)P_1^L + \Delta^L\right]\mathcal{A}_1^+}{\sqrt{2}\left(\Delta^L\right)^2 P_1^+}.
\end{aligned}
\tag{3.15}
$$

We first use the hadron matrices to calculate the form factors by the relations above, then convert them into the BSW conventions. Note that the form factor $f(q^2)$ contains the LFWFs of J/ψ with both $m_j = 0$ and $m_j = 1$ as in $\mathcal{A}_0^+$ and $\mathcal{A}_1^+$. However in BLFQ we derive the LFWFs with fixed m_j independently, leaving the relative phase undetermined between any two different states. Thus we

Table 3.2: Form factors by this work (rows labeled BLFQ - 1 and BLFQ - 2) and other methods at selected values of q^2. The center values of BLFQ listed here are calculated with $N_{\max} = 32$, while the uncertainties are given by $\varepsilon_f = 2|f_{N_{\max}=32} - f_{N_{\max}=24}|$ to show the sensitivity to basis cutoffs.

	$V(0)$	$V(q_{\max}^2)$	$A_1(0)$	$A_1(q_{\max}^2)$	$A_2(0)$	$A_2(q_{\max}^2)$	$A_0(0)$	$A_0(q_{\max}^2)$
BLFQ - 1	0.956(10)	2.166(39)	0.224(6)	0.773(4)	0.345(17)	1.020(59)	0.162(17)	1.017(14)
BLFQ - 2	1.082(67)		0.540(3)		0.724(68)		0.445(31)	
pQCD [110]	0.42	0.94	0.46	0.79	0.64	1.86	0.52	0.99
CCQM [111]	0.78	1.32	0.56	0.79	0.55	0.89	0.56	0.82
RQM [124]	0.49	1.34	0.50	0.88	0.73	1.33	0.40	1.06
Lattice [125]	0.70		0.48					

determine the relative sign between $\psi_{J/\psi}^{(m_j=0)}$ and $\psi_{J/\psi}^{(m_j=1)}$ by checking the non-relativistic component of the LFWFs, and insure that the light-front eigenstates satisfy $\mathcal{J}_+ |m_j = 0\rangle = C |m_j = 1\rangle$, where the total angular momentum projection m_j is related with the orbital angular momentum projection m as $m_j = m + s + \bar{s}$.

Results of form factors as functions of q^2 are shown in Fig. 3.6. The numerical results at $q^2 = 0$ and $q_{\max}^2$ listed in Table 3.2 in comparison with other approaches. We notice that the frame dependence of $V(q^2)$ is much smaller compared to that of the form factors involving two hadron matrices. It shows about 10% deviation at $q^2 = 0$ which agrees with Ref. [116]. We also note that the two special frames in this case do not form a boundary that encloses the general frames. The other three form factors show behavior similar to $f_+(q^2)$ and $f_-(q^2)$ except they pose stronger frame dependence than $V(q^2)$. When we further examine the basis dependence of form factors in Fig. 3.7, they show modest sensitivity to the basis truncation. A similar insensitivity to basis space cutoff is found for the differential decay width of $B_c \to J/\psi$ as shown in Fig. 3.8. Unlike the decay width for $B_c \to \eta_c$ where the longitudinal-I results varies by as much as 100%, this decay width to vector meson does not change substantially with basis size, though the difference between results in different frames is still a major issue. We refer to our discussions above on why the results from the longitudinal-I frame are preferred.
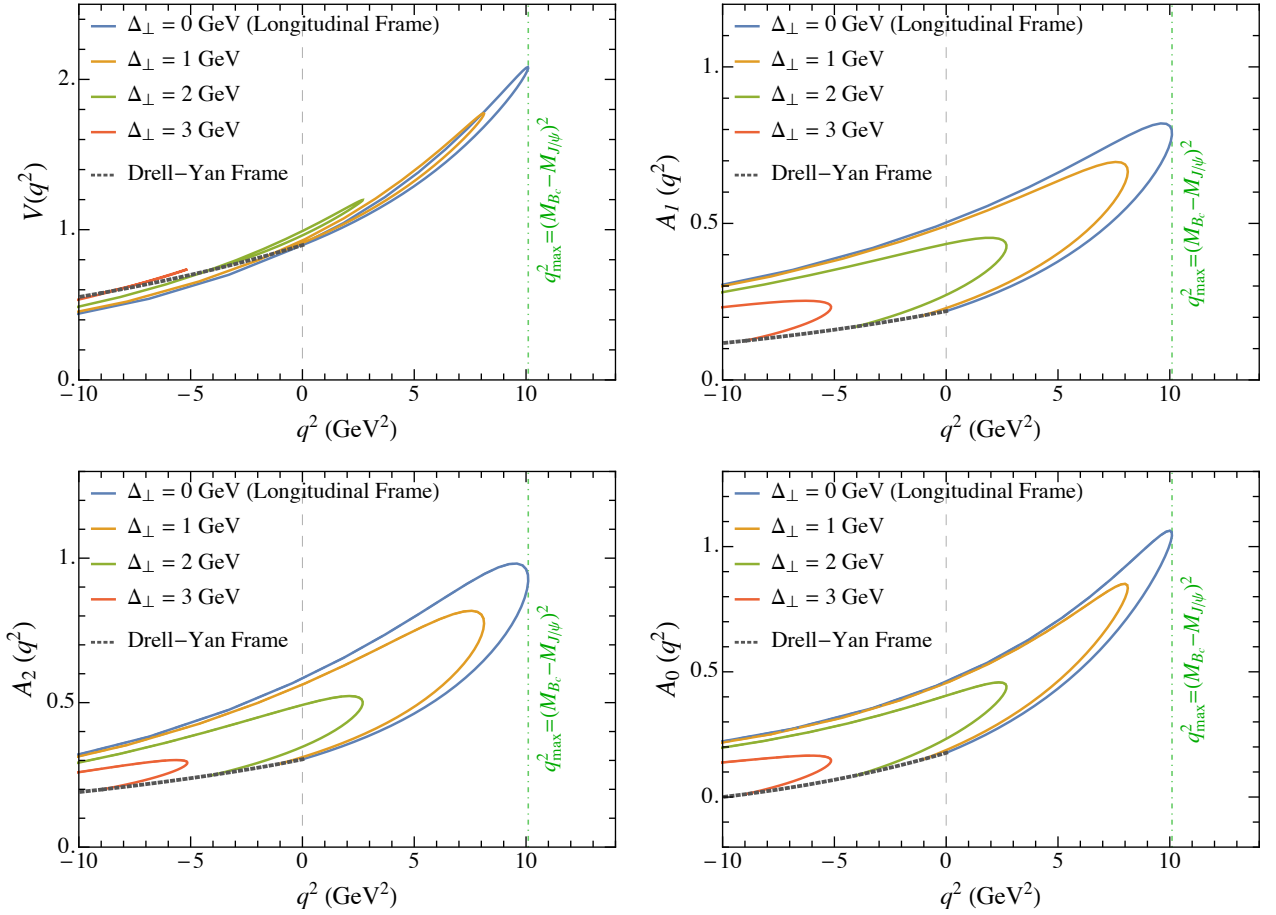
Figure 3.6: The frame dependence of form factors for $B_c \to J/\psi \ell \nu_\ell$ decay at the basis size $N_{\max} = L_{\max} = 8$. Among the four form factors displayed here, $V(q^2)$ is only associated with one hadron matrix and it shows a smaller frame dependence than the others.
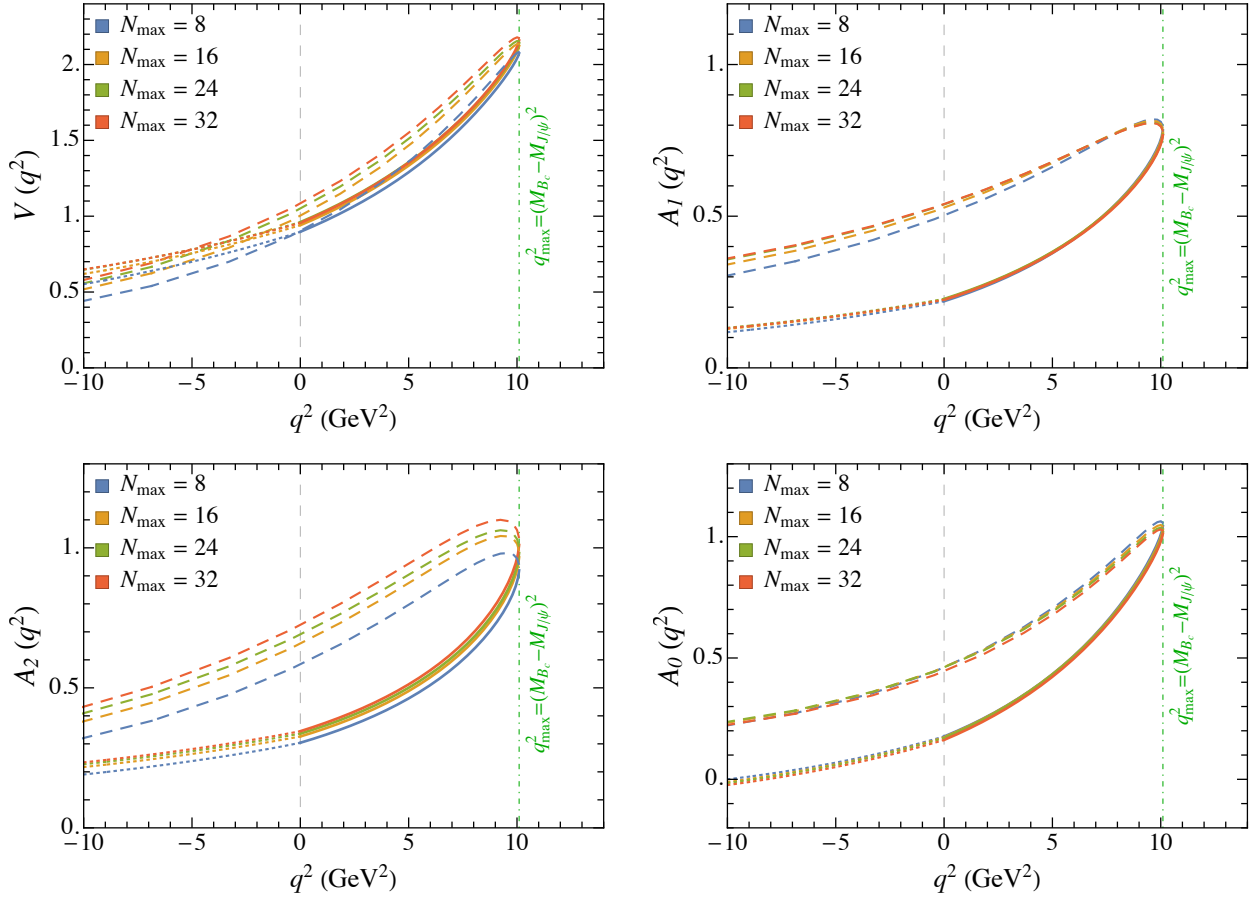
Figure 3.7: The dependence of the form factors on basis size as a function of q^2. Dotted lines are the results from Drell-Yan frame, solid curves are from the longitudinal-I frame while dashed curves are with the longitudinal-II frame.
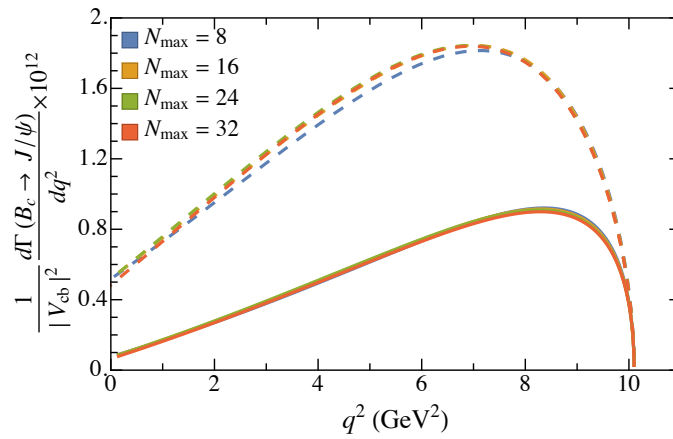
Figure 3.8: The differential decay width for the semileptonic decay of $B_c \to J/\psi e \bar{\nu}$. Results are presented with longitudinal-I (solid) and longitudinal-II (dashed) frames at different basis cutoffs.

3.5 Numerical Calculation Methods

In the era of high-performance computing (HPC), theoretical physics can make advances through powerful numerical calculations. The two most often used parallel computing schemes, which are also adopted in our work, are (MPI) and Open Multi-Processing (OpenMP) [126, 127].

MPI is a standardized and portable message-passing standard which is often used in the distributed memory environment for HPC. In MPI, data are passed among processors (or MPI ranks) which have independent addresses. The standard of MPI includes communication and sync schemes, which is now a default standard for the communications in a distributed computing environment. OpenMP is known as the other commonly used programming standard in HPC. One feature of OpenMP that differs from MPI is that all the parallel computing threads in OpenMP have access to the same shared memory. Due to this reason, OpenMP is widely used in the scenario where memory is shared among multiple cores.

One needs to choose MPI or OpenMP, or even MPI/OpenMP hybrid programming based on the specific situation in order to achieve optimal HPC performance. In this work, we employ MPI/OpenMP hybrid programming that takes advantage of both techniques: it uses MPI to pass messages efficiently among different nodes, while it uses OpenMP threads in each node that has shared memory. In a pure MPI approach to the current application, the increasing number of ranks would cost more memory and eventually exhaust the available resources on the node, which results in inefficient computation. The total memory consumed in hybrid programming for the current application is less than that in pure MPI when OpenMP is introduced. Meanwhile, the scalability in hybrid programming is enhanced since less MPI communication is needed between the nodes. Note that the communication between OpenMP threads occurs with less overhead compared to the traditional MPI. Now we take the calculation of the semileptonic decay form factors as an example.

For each form factor, we compute its value at different q^2; and at each q^2, we have to calculate the current matrix element defined in terms of the overlaps of LFWFs. In order to calculate Eq. (3.12), we carry out the longitudinal integration numerically by using Gauss quadrature for which we apply OpenMP. While we employ MPI for different q^2's since each point is independent

(a) OpenMP

(b) MPI
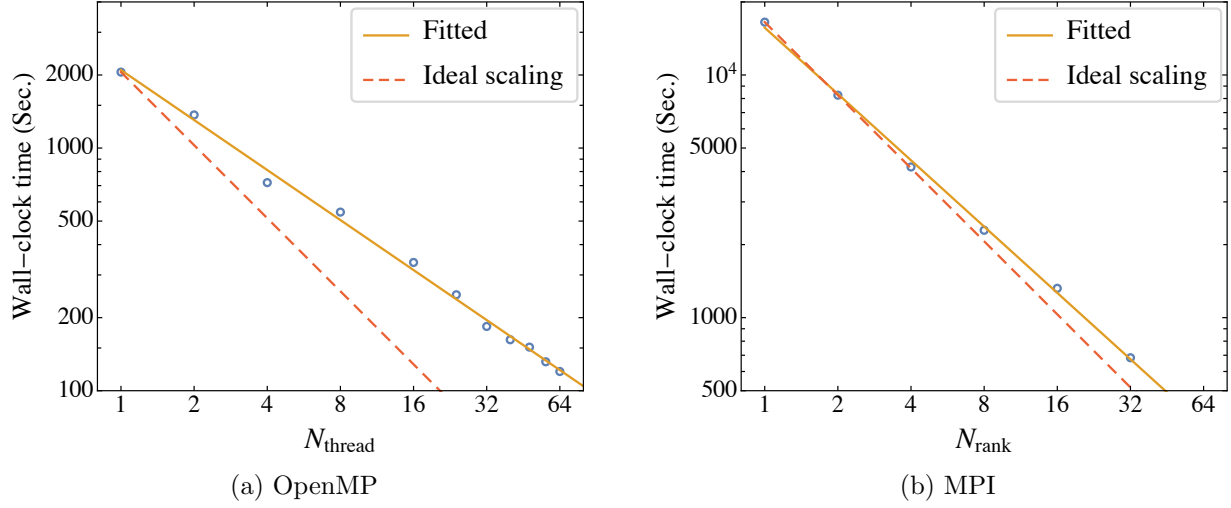
Figure 3.9: The log-log plots of wall-clock time to accomplish the same workload with different number of threads (ranks) using pure OpenMP (MPI). Specifically, we compute the form factors using LFWFs at $N_{\max} = L_{\max} = 24$ for 4 different q^2 points in OpenMP, while compute 32 points in MPI. The exact time at certain numbers of threads (ranks) is indicated by the blue circle, and fitted with the yellow lines. The dashed red line indicate the ideal scaling. In MPI, when all ranks have balanced workload, the parallelization is close to the ideal scaling. However in OpenMP, since the program contains a serial part, it cannot reach the ideal scaling.

of others. In Fig. 3.9 we present the efficiency of using pure OpenMP and MPI. The program is executed on Cori Haswell at NERSC, which has a maximum of 32 cores on each node, while each core supports 2 hyper-threads. We use only one node for this test to avoid the uncontrollable time of communication between different nodes (that depends on other users of the system).

3.6   Summary

We investigated the semileptonic decay of the B_c meson to the pseudoscalar state η_c and vector state J/ψ with the BLFQ approach. LFWFs that include the valence Fock sector $|q\bar{q}\rangle$ were implemented to evaluate the current matrix elements and subsequently the electroweak form factors. Due to the Fock space truncation, the contribution from particle-number-changing diagrams was omitted. In order to access the electroweak from factors in the timelike region, we introduced two boost invariants z and $\vec{\Delta}_\perp$ that specify the choice of reference frame. The frame dependence of form factors arises due to our Fock space truncation when one chooses different combinations of

two variables for the same q^2. However we prefer the results in the Drell-Yan and longitudinal-I frames since within them the contribution from the particle-number-changing diagrams, which are not available in our basis, is suppressed.

We employ the LFWFs obtained in our previous work which are available within certain basis sizes. Within the range of basis sizes available, we observed that the influence on the form factors due to the basis truncations is smaller than the frame dependence, especially in the Drell-Yan and longitudinal-I frames.

In general, when comparing the form factors we obtained in this work to others in the literature, we find reasonable overall agreement but some differences are noticeable. For BLFQ, even though we select specific frames to achieve a more reliable result, we see a need to develop our model by incorporating higher Fock sectors that more completely encompass the dynamics of QCD.

CHAPTER 4. ELECTRON FORM FACTORS IN BASIS LIGHT-FRONT QUANTIZATION

A paper to be published

Shuo Tang, Xingbo Zhao, Yang Li, and James P. Vary

4.1 Abstract

In this paper, we evaluate the electromagnetic and gravitational form factors and the corresponding generalized parton distributions of the electron using the basis light-front quantization approach to QED. We compare our results with those from light-front perturbation theory. We also adopt another basis which results in faster convergence of the form factors with increasing basis dimension. These results both validate the BLFQ approach and provide guidance for its efficient implementation in solving light-front Hamiltonian mass eigenstates for more complex systems in QED and QCD.

4.2 Introduction

Describing the structure of relativistic bound states is one of the fundamental challenges of nuclear and hadronic physics. Among various approaches, the basis light-front quantization (BLFQ) approach has emerged as a promising framework to tackle the nonperturbative dynamics of quantum chromodynamics (QCD) [43]. The applications of BLFQ in quantum electrodynamics (QED) [17, 52, 128, 129] and QCD [48, 49, 53, 91, 130] have shown considerable success. This approach takes advantage of the light-front dynamics and the Hamiltonian formalism, offering intuitive insights into bound state structure. Nevertheless, further efforts are needed to both validate the approach with applications solvable by other means as well as to provide avenues for improved efficiency. These are the dual goals of the present work.

In recent years, the study of gravitational form factors of hadrons has received renewed interest [131–134]. Even though it is impractical to measure the gravitational form factors directly through the coupling of hadrons with a graviton, it is possible to determine them via the corresponding generalized parton distributions (GPDs) which are measured through deeply virtual Compton scattering [135–137]. Such measurement is one of the key goals of the upcoming electron-ion colliders [138, 139].

As support for applying BLFQ to problems in QCD, we investigate here the electron system in QED. The structure of the physical electron serves as a benchmark for GPDs [128, 140, 141], transverse momentum distributions (TMDs) [142] and spin decomposition[143–145], etc, for bound states in QCD. Therefore, we study the electromagnetic and gravitational form factors and their corresponding GPDs of the electron with BLFQ in this work, and compare our results with the results from the light-front perturbation theory [16]. In addition, we use an improved choice of the basis and compare the results with a conventional choice at the end of this paper and demonstrate improved convergence with the improved basis.

The paper is organized as follows. We begin with introducing the theoretical framework, including the choice of naive basis and the corresponding truncation in Sec. 4.3. Then we study the electromagnetic and gravitational form factors and GPDs within the light-front wave function (LFWF) representation in Sec. 4.4. Then in Sec. 4.5, we present the numerical results and compare them with light-front perturbation theory. We introduce another choice of the basis and compare the resulting form factors with those evaluated in the original basis in Sec. 4.5.2. Finally we conclude in Sec.4.6.

4.3   Basis Light-Front Quantization

BLFQ is based on the Hamiltonian formalism, and it aims to solve the light-front eigenvalue equation

$$P^\mu P_\mu \left|\Psi\right\rangle = M^2 \left|\Psi\right\rangle , \tag{4.1}$$

where $P^\mu = (P^+, P^-, \vec{P}^\perp) = (P^0 + P^3, P^0 - P^3, P^1, P^2)$ is the four-momentum operator on the light front, P^- is the light-front Hamiltonian, and M is the mass of the bound state. With the eigenvector $|\Psi\rangle$, one can investigate the observable of interest by computing its matrix element: $\langle \mathcal{O} \rangle = \langle \Psi|\mathcal{O}|\Psi \rangle$. In this work, we study the physical electron which can be expanded schematically in the Fock space as,

$$|e_{\text{phys}}\rangle = c_1 |e\rangle + c_2 |e\gamma\rangle + c_3 |e\gamma\gamma\rangle + c_4 |ee\bar{e}\rangle + ... \tag{4.2}$$

In this work, we truncate the Fock sector up to the first two sectors, namely $|e_{\text{phys}}\rangle = c_1 |e\rangle + c_2 |e\gamma\rangle$. The light-front QED Hamiltonian P^- within the light-cone gauge (i.e. $A^+ = 0$) takes the following form, omitting the instantaneous-photon/fermion interaction since it does not contribute in the current Fock sector truncation [129]:

$$P^- = \int \mathrm{d}^2\vec{x}^\perp \mathrm{d}x^- \left[\frac{1}{2}\bar{\psi}\gamma^+ \frac{m_e^2 + (\mathrm{i}\partial^\perp)^2}{\mathrm{i}\partial^+}\psi + \frac{1}{2}A^j(\mathrm{i}\partial^\perp)^2 A^j + ej^\mu A_\mu \right], \tag{4.3}$$

where x^- is the longitudinal coordinate and $\vec{x}^\perp$ is the transverse coordinate. Here ψ and A_μ are the field operators of the fermion and gauge boson, respectively; m_e and e are the mass and charge of a bare electron.

In BLFQ, a basis representation is employed for the quantized field. For each constituent particle within the Fock sector labeled by i, its longitudinal motion is described by a plane wave, $e^{-\mathrm{i}p_i^+ x_i^-/2}$, where p_i^+ is the longitudinal momentum. We confine the system in a box with width $2L$ so that $-L \leq x_i^- \leq L$; then we impose the (anti-) periodic boundary conditions for (fermions) bosons. Thus the longitudinal momentum of each Fock particle is discretized as $p_i^+ = (2\pi/L)k_i$, with k_i being (half-) integers for (fermions) bosons. Note that for bosons, k_i takes values from 1 instead of 0 since we omit the zero mode. The total longitudinal momentum, a good quantum number for the QED Hamiltonian, is summed over all the momenta of all particles $P^+ = \sum_i p_i^+ = (2\pi/L)K_{\text{tot}}$. Due to the longitudinal boost invariance, the LFWFs only depend on the longitudinal momentum fraction $x_i = p_i^+/P^+ = k_i/K_{\text{tot}}$.

The transverse motion is represented by a 2-dimensional (2D) harmonic oscillator (HO) basis function,

$$\phi_{nm}(\vec{p}_\perp) = \frac{1}{b}\sqrt{\frac{4\pi n!}{(n+|m|)!}}\left(\frac{p_\perp}{b}\right)^{|m|}e^{-\frac{1}{2}p_\perp^2/b^2}L_n^{|m|}(p_\perp^2/b^2)e^{im\theta_p}, \tag{4.4}$$

where n and m are the principal and angular quantum numbers, respectively. b sets the momentum scale of the basis, $L_n^{|m|}$ is the associated Laguerre polynomial, and $\theta_p = \arg \vec{p}_\perp$. We truncate the infinite basis in transverse directions by the truncation parameter N_{max}, so that the retained basis states satisfy

$$\sum_i 2n_i + |m_i| + 1 \leq N_{\text{max}}, \tag{4.5}$$

where the summation runs over all the Fock particles. Then the fermion and gauge boson field operators can be expressed in terms of creation and annihilation operators, together with the basis function,

$$
\begin{aligned}
\psi(\boldsymbol{x}) &= \sum_{\bar{\beta}} \frac{1}{\sqrt{2L}} \int \frac{\mathrm{d}^2\vec{p}_\perp}{(2\pi)^2}\Big[b_{\bar{\beta}}\phi_{nm}(\vec{p}_\perp)\tilde{u}(\boldsymbol{p},\lambda)e^{-\mathrm{i}\boldsymbol{p}\cdot\boldsymbol{x}} + d_{\bar{\beta}}^\dagger\phi_{nm}^*(\vec{p}_\perp)\tilde{v}(\boldsymbol{p},\lambda)e^{\mathrm{i}\boldsymbol{p}\cdot\boldsymbol{x}}\Big], \\
A_\mu(\boldsymbol{x}) &= \sum_{\bar{\beta}} \frac{1}{\sqrt{2Lp^+}} \int \frac{\mathrm{d}^2\vec{p}_\perp}{(2\pi)^2}\Big[a_{\bar{\beta}}\phi_{nm}(\vec{p}_\perp)\epsilon_\mu(\boldsymbol{p},\lambda)e^{-\mathrm{i}\boldsymbol{p}\cdot\boldsymbol{x}} + a_{\bar{\beta}}^\dagger\phi_{nm}^*(\vec{p}_\perp)\epsilon_\mu^*(\boldsymbol{p},\lambda)e^{\mathrm{i}\boldsymbol{p}\cdot\boldsymbol{x}}\Big].
\end{aligned}
\tag{4.6}
$$

Here $\tilde{u}(\boldsymbol{p},\lambda) = u(\boldsymbol{p},\lambda)/\sqrt{p^+}$ ($\tilde{v}(\boldsymbol{p},\lambda) = v(\boldsymbol{p},\lambda)/\sqrt{p^+}$) is the reduced Dirac spinors for (anti-) fermions and $\epsilon_\mu(\boldsymbol{p},\lambda)$ is the photon polarization vector, with the bold font $\boldsymbol{x}$ and $\boldsymbol{p}$ being the 3-coordinate and momentum vector, respectively. λ stands for the helicity. $\bar{\beta} \equiv \{k, n, m, \lambda\}$ denotes the complete single-particle quanta and the creation and annihilation operators satisfy the (anti-) commutation relation as,

$$[a_{\bar{\beta}}, a_{\bar{\beta}'}^\dagger] = \{b_{\bar{\beta}}, b_{\bar{\beta}'}^\dagger\} = \{d_{\bar{\beta}}, d_{\bar{\beta}'}^\dagger\} = \delta_{\bar{\beta}\bar{\beta}'}. \tag{4.7}$$

With the provided relations, one can write down the matrix of the light-front QED Hamiltonian in the basis representation with regularization achieved at the scales defined by N_{max}, b, and K_{tot}. Upon diagonalization of the Hamiltonian, the lowest mass eigenstate is identified as the physical electron state, $|e_{\text{phys}}\rangle$ [17, 146].

Before we evaluate the observables using the obtained LFWF, we need to perform two renormalization procedures. First, we perform mass renormalization. In our current Fock sector truncation,

due to the absence of the $|ee\bar{e}\rangle$ sector, a bare photon cannot fluctuate into an electron-positron pair. Thus one only needs to consider the electron mass renormalization. According to the sector-dependent renormalization approach [21, 23], when numerically diagonalizing the Hamiltonian matrix, we adjust the bare electron mass m_e only in the $|e\rangle$ sector iteratively so that the resulting ground state mass of state $|e_{\text{phys}}\rangle$ is $M_e = 0.511$ MeV. We introduce the mass counter-term ΔM to denote the difference between physical electron mass and bare mass, that is, $\Delta M = M_e - m_e$. It compensates for the mass correction due to the quantum fluctuations to higher Fock sectors, namely to the basis states in $|e\rangle$ sector couple to those in $|e\gamma\rangle$ sector, which generates the conventional one-loop self-energy correction. The dependence of the mass counter-term ΔM on the basis truncation parameters is shown in the upper panel of Fig. 4.1.

Second, we perform wave function renormalization. In BLFQ, the Ward identity $Z_1 = Z_2$ is no longer held due to the Fock sector truncation [147]. Here Z_1 is the renormalization factor for the vertex that couples the $|e\rangle$ and $|e\gamma\rangle$ sectors, which remains unity in the infinite basis limit with our truncated Fock space truncation. Z_2 is the electron wave function renormalization, which can be interpreted as the probability of finding a bare electron in a physical electron system in light-front dynamics, i.e., $Z_2 = |\langle e|e_{\text{phys}}\rangle|^2$. In order to remedy the artifacts from the violation of the Ward identity caused by the Fock sector truncation, following the previous works [128, 129], we rescale our naive results according to Z_2. Specifically, the rescaled observable is

$$\langle \mathcal{O}^{\text{re}} \rangle = \frac{2Z_2 - 1}{Z_2} \left\langle P_e^{-1} \mathcal{O} P_e \right\rangle + \left\langle P_{e\gamma}^{-1} \mathcal{O} P_{e\gamma} \right\rangle. \tag{4.8}$$

Here $\mathcal{O}$ denotes the operators for the forms factors and the GPDs. P_e and $P_{e\gamma}$ are the projection operators onto the $|e\rangle$ and $|e\gamma\rangle$ sectors, respectively. The dependence of the wave function renormalization Z_2 on the basis truncation parameters is shown in the lower panel of Fig. 4.1. Z_2 tends to zero in the infinite basis limit.

4.4 Form Factors and GPDs

After diagonalizing the Hamiltonian within the $|e\rangle$ and $|e\gamma\rangle$ Fock sectors and performing the renormalization procedures, we obtain the renormalized eigenvectors from which we evaluate the
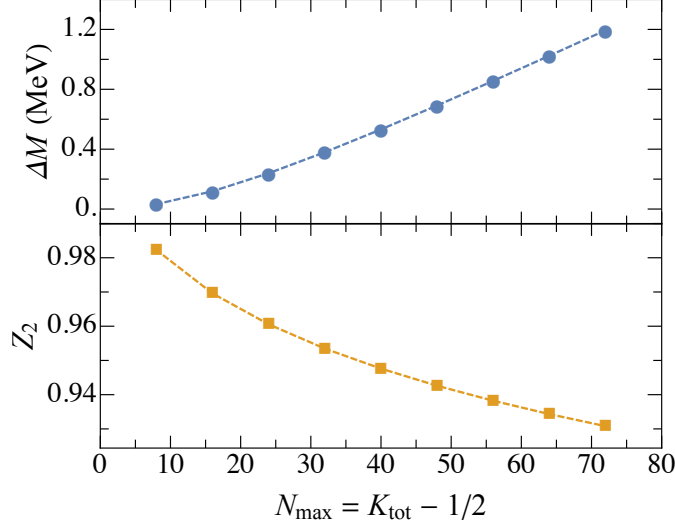
Figure 4.1: Upper and lower panels are the electron mass counter-term ΔM and the wave function renormalization Z_2 as functions of N_{max}, respectively. The basis scale parameter is chosen to be the physical electron mass, namely, $b = M_e = 0.511$ MeV.

LFWFs in momentum space. Having the access to the LFWFs is a major advantage for BLFQ formalism, as they provide direct information on the light-cone distributions or other hadron observables of interest. In this work, we particularly focus on the form factors and GPDs, which can be obtained in terms of the overlap of the LFWFs [16, 123, 148].

We first study the matrix element of the current operator $J^\mu = \overline{\psi}\gamma^\mu\psi$ at $x^\mu = 0$, which is related to the electromagnetic form factors $F_1(q^2)$ and $F_2(q^2)$, also known as Dirac and Pauli form factor, respectively:

$$\left\langle e_{\text{phys}}^{\lambda'}(P')\Big| J^\mu(0) \Big| e_{\text{phys}}^{\lambda}(P) \right\rangle = \bar{u}(\boldsymbol{P}',\lambda')\Big[F_1(q^2)\gamma^\mu + F_2(q^2)\frac{\mathrm{i}}{2M_e}\sigma^{\mu\alpha}q_\alpha \Big] u(\boldsymbol{P},\lambda), \qquad (4.9)$$

where $q^2 = q^\mu q_\mu$, with $q^\mu = (P'-P)^\mu$ being the 4-momentum transfer. The state vector $\left| e_{\text{phys}}^{\uparrow(\downarrow)}(\vec{q}_\perp) \right\rangle$ stands for a physical electron state with helicity (anti-) parallel to the direction of P^+ and the center of mass momentum $\hat{q}_\perp$. The following relations result from adopting the "good current" $(\mu = +)$ in the Drell-Yan frame, where the probe photon is carrying the longitudinal momentum $q^+ = 0$.

The electromagnetic form factors can then be separated as,

$$
\begin{aligned}
\left\langle e^{\uparrow}_{\text{phys}}(\vec{q}_{\perp}) \Big| \frac{J^{+}(0)}{2P^{+}} \Big| e^{\uparrow}_{\text{phys}}(\vec{0}_{\perp}) \right\rangle &= F_1(q^2), \\
\left\langle e^{\uparrow}_{\text{phys}}(\vec{q}_{\perp}) \Big| \frac{J^{+}(0)}{2P^{+}} \Big| e^{\downarrow}_{\text{phys}}(\vec{0}_{\perp}) \right\rangle &= -(q_1 - \mathrm{i}q_2)\frac{F_2(q^2)}{2M_e}.
\end{aligned}
\tag{4.10}
$$

The equations above indicate that $F_1(q^2)$ and $F_2(q^2)$ correspond to the helicity-preserving and helicity-flip matrix elements of J^{+}. Due to the boost invariance of LFWFs, the state with nonzero transverse momentum could be related to that with zero transverse momentum. For the helicity-flip state, one can also represent it with the helicity-preserving state by exploiting the transverse parity symmetry [10, 149].

Similar to the current operator J^{μ}, the matrix element of the energy-momentum tensor $T^{\mu\nu}$ for the electron defines the gravitational form factors [150]. Specifically, the energy-momentum tensor of QED is given by [16],

$$
T^{\mu\nu} = \frac{\mathrm{i}}{4} \left(\left[\overline{\psi}\gamma^{\mu}(\overrightarrow{\partial}^{\nu} + \mathrm{i}eA^{\nu})\psi - \overline{\psi}\gamma^{\mu}(\overleftarrow{\partial}^{\nu} - \mathrm{i}eA^{\nu})\psi \right] + [\mu \leftrightarrow \nu] \right) + F^{\mu\rho}F^{\nu}_{\rho} + \frac{1}{4}g^{\mu\nu}F^{\rho\lambda}F_{\rho\lambda}, \tag{4.11}
$$

where $F^{\mu\nu} \equiv \partial^{\mu}A^{\nu} - \partial^{\nu}A^{\mu}$ is the electromagnetic field tensor. Compared with J^{μ}, the decomposition of $T^{\mu\nu}$ has a more intricate structure, and can be written in terms of fermion (f) and boson (b) separately as,

$$
\begin{aligned}
&\left\langle e^{\lambda'}_{\text{phys}}(P') \Big| T^{\mu\nu}_{\text{f,b}}(0) \Big| e^{\lambda}_{\text{phys}}(P) \right\rangle \\
&= \bar{u}(\boldsymbol{P}', \lambda') \Big[A_{\text{f,b}}(q^2)\gamma^{(\mu}\overline{P}^{\nu)} + B_{\text{f,b}}(q^2)\frac{\mathrm{i}}{2M_e}\overline{P}^{(\mu}\sigma^{\nu)\alpha}q_{\alpha} + C_{\text{f,b}}(q^2)\frac{1}{M_e}(q^{\mu}q^{\nu} - g^{\mu\nu}q^2) \Big] u(\boldsymbol{P}, \lambda),
\end{aligned}
\tag{4.12}
$$

where $\overline{P}^{\mu} = (P'^{\mu} + P^{\mu})/2$, $a^{(\mu}b^{\nu)} = (a^{\mu}b^{\nu} + a^{\nu}b^{\mu})/2$. Analogous to $F_1(q^2)$ and $F_2(q^2)$, we have the light-cone representation of form factors $A_{\text{f,b}}(q^2)$ and $B_{\text{f,b}}(q^2)$. In this work we take the component $\mu\nu = ++$ and obtain:

$$
\begin{aligned}
\left\langle e^{\uparrow}_{\text{phys}}(\vec{q}_{\perp}) \Big| \frac{T^{++}_{\text{f,b}}(0)}{2(P^{+})^2} \Big| e^{\uparrow}_{\text{phys}}(\vec{0}_{\perp}) \right\rangle &= A_{\text{f,b}}(q^2), \\
\left\langle e^{\uparrow}_{\text{phys}}(\vec{q}_{\perp}) \Big| \frac{T^{++}_{\text{f,b}}(0)}{2(P^{+})^2} \Big| e^{\downarrow}_{\text{phys}}(\vec{0}_{\perp}) \right\rangle &= -(q_1 - \mathrm{i}q_2)\frac{B_{\text{f,b}}(q^2)}{2M_e}.
\end{aligned}
\tag{4.13}
$$

By choosing the $\mu\nu = ++$ component and the Drell-Yan frame, the term associated with form factor $C_{\text{f,b}}(q^2)$ in Eq. (4.12) vanishes. $A(q^2) = A_{\text{f}}(q^2) + A_{\text{b}}(q^2)$ and $B(q^2) = B_{\text{f}}(q^2) + B_{\text{b}}(q^2)$ are

the total gravitational form factors consist of the constituent fermion and boson. Also notice that the form factors receive the contribution from all the Fock sectors, which in our current truncation scheme includes only the $|e\rangle$ and $|e\gamma\rangle$ sectors.

As the 2D Fourier transform (F.T.) of Dirac and Pauli form factors are associated with charge and magnetization density distribution in the transverse plane [151], the 2D F.T. of $A(q^2)$ gives the longitudinal momentum density in the transverse impact parameter space [152, 153]. The spin-flip form factor $B(q^2)$ is an analog of the Pauli form factor $F_2(q^2)$. The F.T. of $B(q^2)$ gives the density of the gravitational magnetic moment in the transverse plane [154, 155].

In order to provide a more detailed view of the charge and matter distribution inside the physical electron, we also investigate the GPDs of the electron, which are universal nonperturbative objects used to describe hard exclusive processes. $H_{\mathrm{f,b}}$ and E_{fb} are the leading twist (twist-2) off-forward parton distributions defined through the following light-cone functions for fermion and boson, respectively [136, 148, 156]:

$$
\begin{aligned}
&\int \frac{\mathrm{d}z^-}{8\pi} \exp\!\big(\mathrm{i}xP^+z^-/2\big) \left\langle e^{\lambda'}_{\mathrm{phys}}(P')\Big|\overline{\psi}(0)\gamma^+\psi(z)\Big|e^{\lambda}_{\mathrm{phys}}(P)\right\rangle\Big|_{z^+=0,z^\perp=0} \\
&=\frac{1}{2\overline{P}^+}\bar{u}(\boldsymbol{P}',\lambda')\Big[H_{\mathrm{f}}(x,\zeta,t)\gamma^+ + E_{\mathrm{f}}(x,\zeta,t)\frac{\mathrm{i}\sigma^{+j}(-\Delta_j)}{2M}\Big]u(\boldsymbol{P},\lambda),
\end{aligned}
\tag{4.14}
$$

and

$$
\begin{aligned}
&\frac{1}{2P^+}\int \frac{\mathrm{d}z^-}{2\pi} \exp\!\big(\mathrm{i}xP^+z^-/2\big) \left\langle e^{\lambda'}_{\mathrm{phys}}(P')\Big|A^+(0)A^+(z)\Big|e^{\lambda}_{\mathrm{phys}}(P)\right\rangle\Big|_{z^+=0,z^\perp=0} \\
&=\frac{1}{2\overline{P}^+}\bar{u}(\boldsymbol{P}',\lambda')\Big[H_{\mathrm{b}}(x,\zeta,t)\gamma^+ + E_{\mathrm{b}}(x,\zeta,t)\frac{\mathrm{i}\sigma^{+j}(-\Delta_j)}{2M}\Big]u(\boldsymbol{P},\lambda).
\end{aligned}
\tag{4.15}
$$

Here $\Delta^\mu = (P - P')^\mu = \big(\zeta P^+, \vec{\Delta}_\perp, (t+\Delta_\perp^2)/(\zeta P^+)\big)$, $t = \Delta^2$, and $\overline{P}^+ = (P'^+ + P^+)/2 = (1 - \zeta/2)P^+$ with ζ labeling the skewness. From the definition, H is associated with the helicity-conserving amplitude, while E is with helicity-flipping amplitude. In this work, we calculate the GPDs of the $|e\gamma\rangle$ sector at the zero skewness limit $\zeta = 0$ by choosing the Drell-Yan frame. Therefore, only the diagonal process contributes for the interval $0 \leq x \leq 1$. In addition, from the first moment of the GPDs at zero skewness, one gets the following sum rules for F_1 and F_2,

$$
F_{1\ \mathrm{f,b}}(t) = \int_0^1 H_{\mathrm{f,b}}(x,\zeta=0,t)\mathrm{d}x, \qquad F_{2\ \mathrm{f,b}}(t) = \int_0^1 E_{\mathrm{f,b}}(x,\zeta=0,t)\mathrm{d}x;
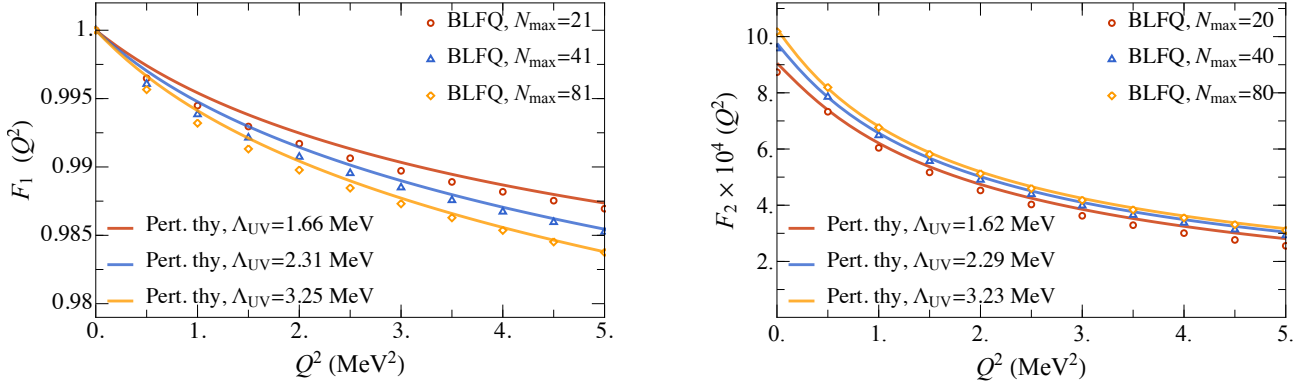\tag{4.16}
$$

Figure 4.2: The electromagnetic form factors F_1 and F_2 calculated with BLFQ and with light-front perturbation theory. The BLFQ results of F_1 are given as the average of adjacent $N_{\max}$, e.g. $N_{\max} = 20$ (22) denotes the results are the average of $N_{\max} = 20$ and $N_{\max} = 22$, to smooth over the "odd-even" effect, see text. For F_2, we only adopt the results with even $N_{\max}/2$ for faster convergence.

and the gravitational form factors are related to the second moment of the GPDs,

$$A_{\mathrm{f,b}}(t) = \int_0^1 x H_{\mathrm{f,b}}(x, \zeta = 0, t)\mathrm{d}x, \qquad B_{\mathrm{f,b}}(t) = \int_0^1 x E_{\mathrm{f,b}}(x, \zeta = 0, t)\mathrm{d}x. \qquad (4.17)$$

4.5   Numerical Results

4.5.1   Form Factors and GPDs

We perform our calculations in truncated bases with truncation parameters K_{tot} and $N_{\max}$, where K_{tot} represents the longitudinal resolution, and $N_{\max}$ specifies the ultraviolet (UV) and inferred (IR) regulators in the transverse plane. For simplicity, we set $N_{\max} = K_{\mathrm{tot}} - 1/2$ throughout this paper. We set the coupling strength $\alpha = 1/137.036$ and the scale parameter in transverse basis function to the physical electron mass, i.e. $b = M_e = 0.511$ MeV, according to Ref. [129].

In this work we only access the space-like kinematic region, $q^2 < 0$, for convenience. Fig. 4.2 illustrates the electromagnetic form factors as functions of Q^2 for different basis truncations. We use open markers for the BLFQ results, and compare with the light-front perturbation theory for the two-particle Fock state of the electron (solid curves) [16]. In BLFQ, the truncation up to the one-fermion one-gauge boson Fock state component is expected to contain the equivalent

physics as the Schwinger one-loop radiative correction. The light-front perturbation theory is expected to give identical results with BLFQ at infinite basis size in the case of the physical electron. However, since the Dirac form factor is divergent at nonzero Q^2, regulators are needed for the comparison. In BLFQ, $N_{\max}$ works as the underlying regulator; while for perturbation theory, we implement the integral cutoffs in momentum space as the corresponding regulators. In the transverse directions, the UV and IR cutoffs are chosen to match those in BLFQ which are estimated as $\Lambda_{\mathrm{UV}} \approx b\sqrt{N_{\max}/2}$ and $\lambda_{\mathrm{IR}} \approx b/\sqrt{8N_{\max}}$ [52, 128]. In the longitudinal direction, we integrate from $x=1/K_{\mathrm{tot}}$ to $1 - 1/K_{\mathrm{tot}}$. For example, $N_{\max} = 20$ in BLFQ corresponds to $\Lambda_{\mathrm{UV}} = 1.62$ MeV and $\lambda_{\mathrm{IR}} = 0.04$ MeV in the perturbation theory calculations. Since the UV and IR cutoffs in BLFQ and perturbation theory are implemented in different manners, we cannot expect the results from these two methods to match exactly. Nevertheless, the differences between the two methods are expected to decrease with the increase of $N_{\max}$, as we show in Fig. 4.2.

We also observe an "odd-even effect" in BLFQ where the results fall into two groups with even and odd $N_{\max}/2$ (see Ref. [129]). This effect is due to the oscillatory behavior of the transverse basis functions. Thus for $F_1(Q^2)$, we average over results obtained at two adjacent $N_{\max}$ values (we quote the lower $N_{\max}$ out of the two being averaged in the legend) to smooth this "odd-even" effect. For the corresponding perturbation theory results, we adopt the averaged $N_{\max}$ value to match the UV and IR cutoffs. See Fig. 4.2. Unlike the Dirac form factor, the Pauli form factor is convergent in the entire momentum space. However, we still apply the cutoffs to the perturbation theory to keep consistency with BLFQ. Without taking the average between adjacent $N_{\max}$, we obtain reasonable agreement between two approaches. In particular, $F_2(Q^2 \to 0)$ corresponds to the anomalous magnetic moment a_e. In our previous work [129], upon extrapolating $N_{\max}$ and K_{tot} to infinity, the resulting a_e agrees with Schwinger result to an accuracy of 0.06%, which was consistent with the expected numerical precision. Both the electromagnetic form factors decrease as the momentum transfer increases. F_2 will fall to zero at infinite Q^2, while F_1 will end up with $(2Z_2 - 1)/Z_2$ (c.f. Eq. (4.8)), the contribution from the single electron sector which is independent on Q^2 [151].

The evaluation of gravitational form factors is similar to that for electromagnetic form factors albeit with some additional complexity: both the constituent fermion and boson couple to the graviton and thus contribute to the gravitational form factors. The matrix elements of T^{++} allow us to calculate the fermion and boson contributions to the gravitational form factors $A_{f,b}(Q^2)$ and $B_{f,b}(Q^2)$ separately. Note that the contribution from the constituent boson to the gravitational form factor, $B_b(Q^2)$ is negative.

According to Ji's sum rule [150, 157], we have

$$A(0) = A_f(0) + A_b(0) = (P_f + P_b)/P_{tot} = 1,$$
$$\frac{1}{2}\big[A_f(0) + B_f(0) + A_b(0) + B_b(0)\big] = J_f + J_b = \frac{1}{2}, \tag{4.18}$$

at zero momentum transfer. These are consequences of conservation of momentum and angular momentum, and lead to $B(0) = B_f(0) + B_b(0) = 0$. This last result is known as the vanishing anomalous gravito-magnetic moment which is closely connected with the Einstein equivalence principle [158, 159]. In BLFQ we obtain this result at all basis sizes as shown in Fig. 4.3.

In order to obtain a better understanding of the differences between results from BLFQ and light-front perturbation theory, we turn to the GPDs of the physical electron. It has been shown in a previous work that GPDs $H(x, \zeta = 0, t)$ and $E(x, \zeta = 0, t)$ agree reasonably well with light-front perturbation theory [128]. Here $x \equiv p_e^+/P^+ = p_e^+/(p_e^+ + p_\gamma^+)$ stands for the longitudinal momentum fraction of the constituent electron. As an example, we present results of GPDs in Fig. 4.4 and compare with perturbation theory at $t = -2 \text{ MeV}^2$. We can see that the main difference between BLFQ and light-front perturbation theory is in the $x \sim 1$ region, where the constituent photon takes a small longitudinal momentum fraction. Due to the divergent behavior of H at $x \sim 1$, the results are sensitive to the details of the cutoff. Hence, the differences between two light-front approaches are larger in $F_1(Q^2)$ and $A(Q^2)$ than those in $F_2(Q^2)$ and $B(Q^2)$. However, in all cases, these differences are decreasing systematically as the cutoffs are lifted indicating the utility of our adopted relationship between cutoffs in the two different methods. In Fig. 4.5, the GPDs are shown as 3-dimensional (3D) plots with respect to both x and t in order to provide a visual overview of the general structure in both the transverse and longitudinal direction.
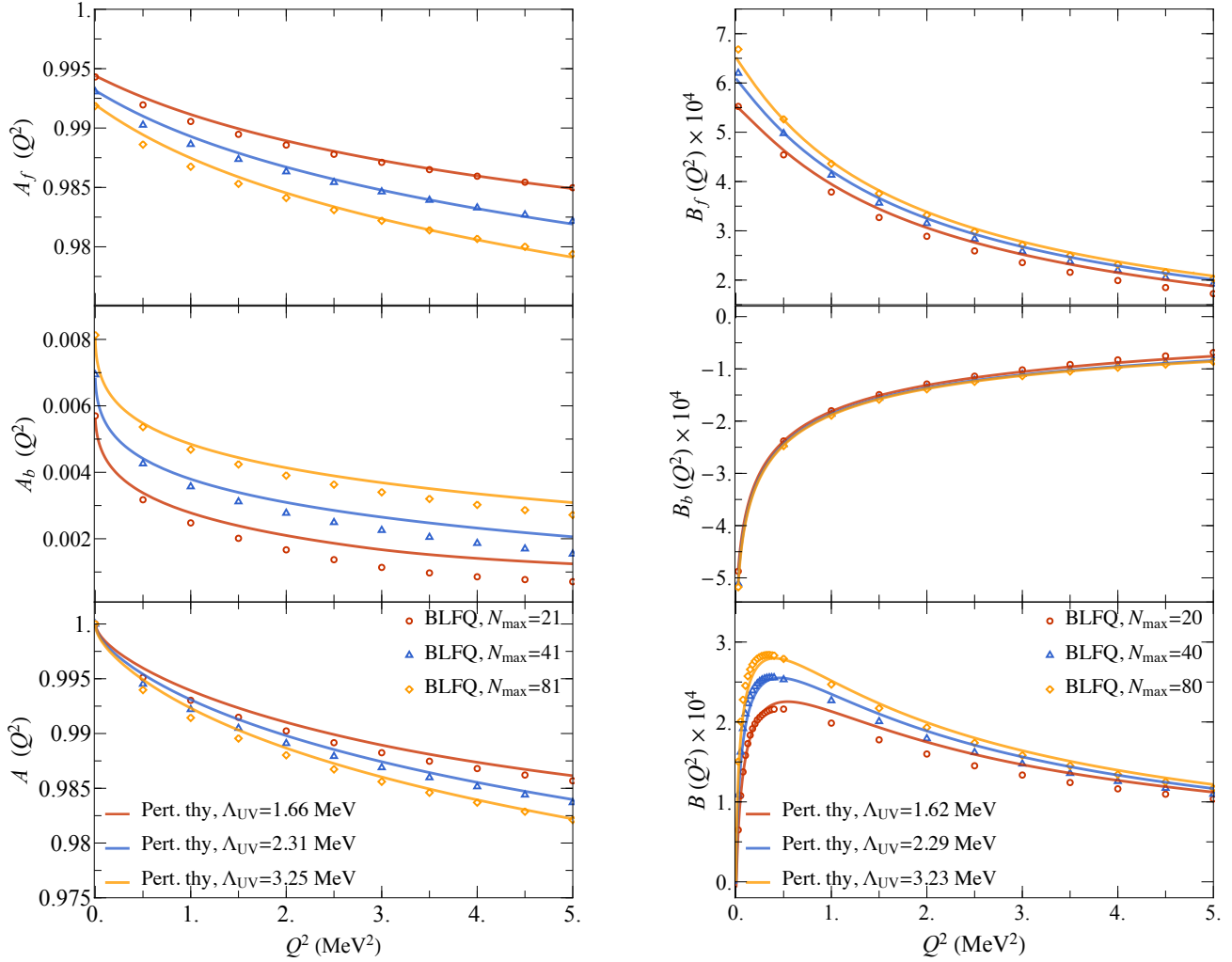
Figure 4.3: We show the constituent gravitational form factors distributed by the constituent electron and photon respectively, then followed by the total gravitational form factors. Remarkably, $B(Q^2 \to 0)$ from BLFQ is always zero independent of $N_{\max}$. Similar to F_1 and F_2, the discrepancy between BLFQ and light-front perturbation theory decreases as the basis size increases.
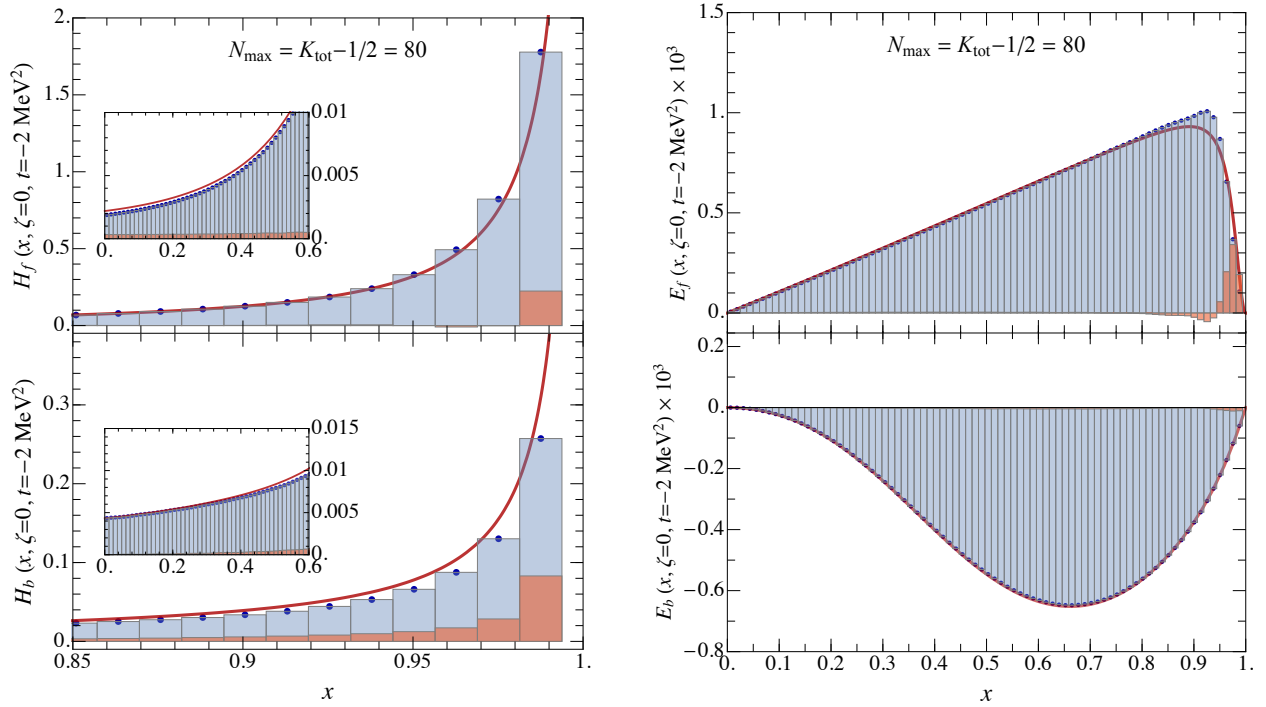
Figure 4.4: The GPDs of electron and photon in a physical electron, labeled as "$H_{\rm f}$ ($E_{\rm f}$)" and "$H_{\rm b}$ ($E_{\rm b}$)", respectively. We present the GPDs calculated at $t = -2$ MeV^2. Blue dots show the value obtained by BLFQ and are compared with the light-front perturbation theory results, which are shown with red solid curves. We also use the vertical bars to present the contribution from each discrete longitudinal bin. Blue bars are for BLFQ, whereas the red bars represent the difference from perturbation theory.
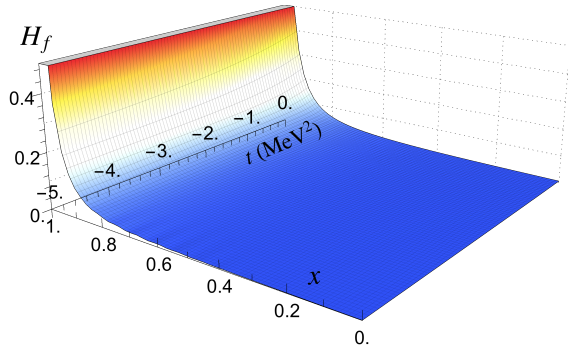
(a) GPD H of the constituent fermion (electron) in $|e\gamma\rangle$ sector.
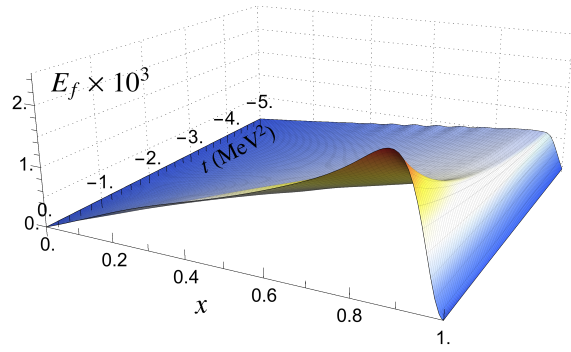
(b) GPD E of the constituent fermion (electron) in $|e\gamma\rangle$ sector.
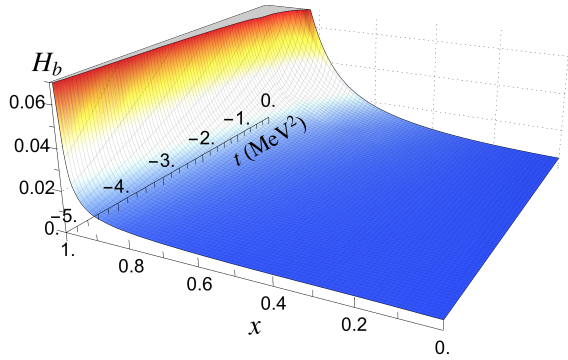
(c) GPD H of the constituent boson (photon) in $|e\gamma\rangle$ sector.
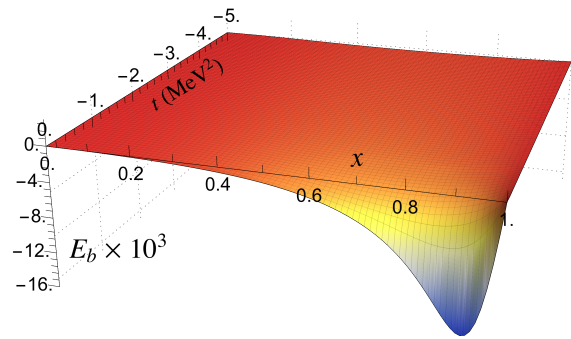
(d) GPD E of the constituent boson (photon) in $|e\gamma\rangle$ sector.

Figure 4.5: 3D plots of GPDs of gravitational form factors calculated by BLFQ at basis $N_{\max} = K_{\text{tot}} - 1/2 = 80$ with respect to x and t.

4.5.2 The x-dependent b Basis

In all the calculations above, the scale parameter b that appears in the HO basis function is a constant over x. However in this section, we adopt a basis where b depends on the longitudinal momentum fraction of the i-th particle, i.e. $b'_i = b\sqrt{x_i}$. Here b is an x-independent dimensional constant. For this x-dependent b basis, we match it with the conjugate HO basis where the momentum $\vec{q}_{i\perp}$ is associated with our momentum $\vec{p}_{i\perp}$ by $\vec{q}_{i\perp} = \vec{p}_{i\perp}/\sqrt{x_i}$ [17, 47, 130]. Essentially, this basis and the conjugate basis are equivalent since one extracts the dependence of longitudinal momentum fraction from transverse momentum $\vec{p}_\perp$ to the scale parameter b (c.f. Eq. (4.4)). This basis allows for the exact factorization between the center-of-mass motion and the intrinsic motion [17].

In order to study the convergence behavior of the x-dependent b basis and make comparison with the x-independent b basis, we calculate the two non-divergent form factors $F_2(Q^2)$ and $B(Q^2)$ with both bases at $N_{\max} = K_{\text{tot}} - 1/2 = 40$, and compare with the perturbative results, where no cutoffs in the momentum space integration are applied. At infinite $N_{\max}$ and K_{tot}, the BLFQ results with both basis are expected to converge to the perturbative results at infinite $N_{\max}$. In the truncated bases, one can see from Fig. 4.6 that for both $F_2(Q^2)$ and $B(Q^2)$, the x-dependent b basis leads to values much closer to the perturbation theory than the fixed-b basis. Meanwhile, one should be aware that the advantage of the x-dependent b basis is more pronounced in the low Q^2 region. When Q^2 increases, the difference among three methods diminishes. Thus the x-dependent b basis is more suitable to calculate the observables associated with lower Q^2, such as the charge and mass radius.

The advantage of adopting the x-dependent b basis is that it supports a faster convergence of the observables than fixed-b, thus the former is expected to save substantial computational resources. In order to further test this idea, we compare the results of the electron anomalous magnetic moment a_e calculated with two bases at different $N_{\max}$ in Fig. 4.7. We notice that the comparable values can be achieved with the x-dependent b basis at a much smaller $N_{\max}$ compared the fixed-b basis, which translates to a much smaller basis dimensionality and thus much reduced computational resources. Again, in the complete basis limit, both methods provide the results consistent with the
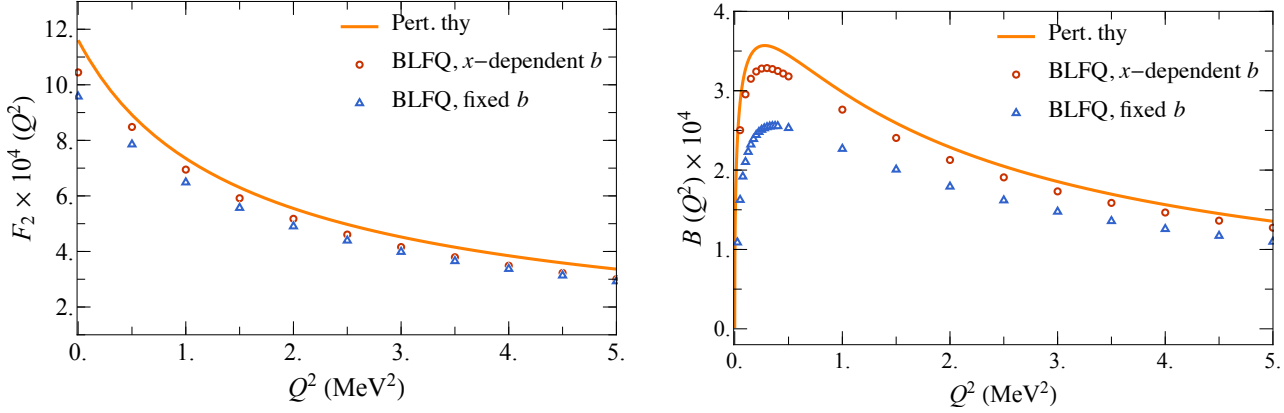
Figure 4.6: Two non-divergent form factors, the Pauli form factor F_2 and the gravitational form factor B, calculated with x-dependent b and fixed-b basis in BLFQ at $N_{\max} = K_{\text{tot}} - 1/2 = 40$, and compared with perturbation theory. The x-dependent b basis shows a faster convergence compared to the fixed-b basis in the lower Q^2 region.

Schwinger result. It is one of the future tasks to see whether for other observables the x-dependent b basis also shows the advantage of improved convergence rates.

4.6 Summary

In this work, we investigated the physical electron system in the BLFQ approach, where two leading Fock sectors were considered in the basis. Based on the resulting LFWFs we calculated both the electromagnetic and the gravitational form factors and their corresponding GPDs. We performed nonperturbative renormalization both on the light-front Hamiltonian and on the resulting LFWFs. All these results show reasonable agreement with light-front perturbation theory when implemented with a proper regularization. As the basis size increases, the agreement between the perturbative and BLFQ results improves. We also evaluated the form factors in an x-dependent b basis, and found that it provided faster convergence to the anticipated perturbative results for the electromagnetic and gravitational form factors. These results both validate the BLFQ approach and provide guidance for efficient implementation of computational approaches to light-front Hamiltonian treatments of QED and QCD for more complex systems such as those, as in this example, involve dynamical gauge bosons.
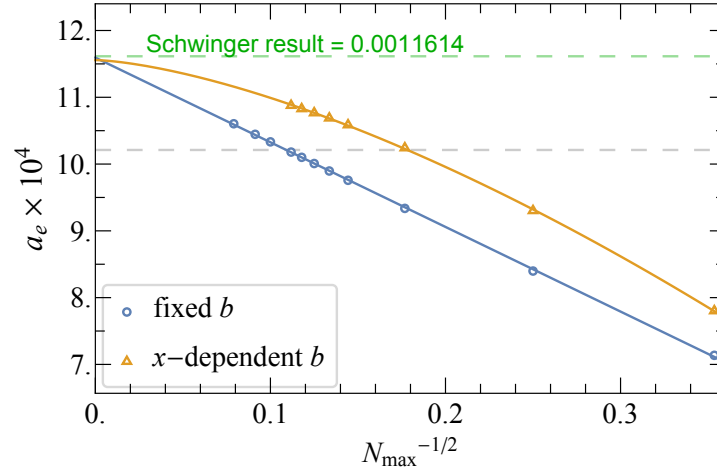
Figure 4.7: The convergence of two methods as $N_{\max}$ approaches infinity. A faster convergence of $a_e \equiv F_2(Q^2 \to 0)$ is achieved with the x-dependent b basis. For instance, to achieve $a_e \approx 0.00102$ (gray dashed line), which is about 88% of the Schwinger value, one needs $N_{\max} = 80$ (with the basis dimension 5182401) in the fixed-b basis, whereas one needs only $N_{\max} = 32$ (with the basis dimension 134913) in the x-dependent b basis. We apply linear extrapolation for the fixed-b, and the function $a(1/\sqrt{N_{\max}})^{3/2} + b$ to fit x-dependent b. The extrapolation of the results performed in both bases to infinite $N_{\max} = K_{\text{tot}} - 1/2$ agrees reasonably well with the Schwinger result.

The agreement with perturbation theory on the form factors of the electron constitutes a comprehensive test of the LFWF obtained from the BLFQ approach. It is also an important test of the viability of the nonperturbative renormalization procedure carried out in BLFQ. This application of BLFQ to the physical electron system provides us with the guidance to study the bound states in QCD with BLFQ where Fock sectors beyond the valence sector are included in the basis. As a next step, we plan to investigate the gravitational form factors of hadrons, the pion for instance, and compare the results with those from existing experiments [160] and other theoretical approaches, and make predictions for future experiments. Another line of future development is to include an even higher Fock sector, eg. $|ee\bar{e}\rangle$, in the basis to further test the approach. By doing so, we need to further develop the nonperturbative renormalization procedure to handle the possible divergences arising from the quantum fluctuation of a photon to an electron-positron pair. If this is successful, we will be able to obtain a finer and more realistic description of the relativistic bound state structure in the BLFQ approach.

CHAPTER 5.   CONCLUSION AND OUTLOOK

In this thesis, we apply the basis light-front quantization approach to investigate the unequal-mass heavy mesons, a QCD bound state problem, and the physical electron system, a QED bound state problem.

For the unequal-mass mesons, we have extended the effective Hamiltonian from the heavy quarkonium to the mixed flavor heavy-heavy mesons without adjusting any parameter. In general, the obtained mass spectrum of heavy mesons have reasonable agreement with experiments. The asymmetry of LFWFs were noticed, which also results in the asymmetric distribution of other observables, such as the parton distribution function and distribution amplitude.

Since we did not consider the chiral symmetry in our model, one may be concerned about the symmetry breaking brought in by the light quark in the heavy-light meson. This particular question is not answered with our current results since our model breaks chiral symmetry and uses light quark masses fitted to data. When we look at the spectra, there is no colossal discrepancy form experimental spectra when considering both the ground state pseudoscalar and the first excited vector states. However, when we calculate the observables, the decay constant for instance, the results we get show considerable difference from other theories. Furthermore, the ratio of decay constant of the vector to that of the pseudoscalar is much smaller than other approaches, which could be a signal of the omission of chiral symmetry in the model.

We also study the semileptonic decays in BLFQ for the first time. Specifically, we focus on the transition diagram where the initial and final constituent particle number is conserved. Because the semileptonic decay requires a timelike character of the exchanged boson, we implemented an unconventional kinematic frames and noticed a frame-dependence of the form factors. This dependence indicates the violation of the Lorentz symmetry of our model, which is due to the truncation of the Fock space to just the quark-antiquark sector. The significant difference between

the results from various frames suggests we need go further to explore the higher Fock sector contributions, especially the Z-diagram which has been shown to provide important contributions in other works.

As an example of expanding Fock space to higher sectors, we study the physical electron with two Fock sectors, one of which involves a dynamical photon. In this part we calculated the electromagnetic form factors and the gravitational form factors with BLFQ, which agree well with light-front perturbation theory. Another conjugate basis implemented there also provides us a valuable tool for improving convergence. The success in the QED application indicates a potential pathway to investigate the QCD bound-state problems. For example, it would be appealing to include a dynamical gluon in the Fock space of the mesons and to eliminate the effective interaction for one-gluon exchange between the quark and the antiquark.

With continually increasing computational capacity, we identify opportunities to carry out larger scale calculations to achieve further improvements in our understanding of nonperturbative quantum field theory on the light front.

BIBLIOGRAPHY

[1] G. Aad, T. Abajyan, B. Abbott, J. Abdallah, S. Abdel Khalek, A.A. Abdelalim, O. Abdinov, R. Aben, B. Abi, M. Abolins, and et al. Observation of a new particle in the search for the standard model higgs boson with the atlas detector at the LHC. *Physics Letters B*, 716(1):1 – 29, 2012.

[2] S. Chatrchyan, V. Khachatryan, A.M. Sirunyan, A. Tumasyan, W. Adam, E. Aguilo, T. Bergauer, M. Dragicevic, J. Er, C. Fabjan, and et al. Observation of a new boson at a mass of 125 GeV with the CMS experiment at the LHC. *Physics Letters B*, 716(1):30 – 61, 2012.

[3] Michael Peskin. *An introduction to quantum field theory*. CRC press, 2018.

[4] Kenneth G. Wilson. Confinement of quarks. *Phys. Rev. D*, 10:2445–2459, Oct 1974.

[5] Craig D. Roberts and Anthony G. Williams. Dyson-Schwinger equations and their application to hadronic physics. *Progress in Particle and Nuclear Physics*, 33:477 – 575, 1994.

[6] P. Maris and P.C. Tandy. QCD modeling of hadron physics. *Nuclear Physics B - Proceedings Supplements*, 161:136 – 152, 2006. Proceedings of the Cairns Topical Workshop on Light-Cone QCD and Nonperturbative Hadron Physics.

[7] R. Machleidt and D.R. Entem. Chiral effective field theory and nuclear forces. *Physics Reports*, 503(1):1 – 75, 2011.

[8] Estia Eichten and Brian Hill. An effective field theory for the calculation of matrix elements involving heavy quarks. *Physics Letters B*, 234(4):511 – 516, 1990.

[9] Mikhail Shifman. Snapshots of Hadrons: Or the Story of How the Vacuum Medium Determines the Properties of the Classical Mesons which are Produced, Live and Die in the QCD Vacuum. *Progress of Theoretical Physics Supplement*, 131:1–71, 02 1998.

[10] Stanley J. Brodsky, Hans-Christian Pauli, and Stephen S. Pinsky. Quantum chromodynamics and other field theories on the light cone. *Physics Reports*, 301(4):299 – 486, 1998.

[11] B. L. G. Bakker et al. Light-Front Quantum Chromodynamics: A framework for the analysis of hadron physics. *Nucl. Phys. Proc. Suppl.*, 251-252:165–174, 2014.

[12] P. A. M. Dirac. Forms of relativistic dynamics. *Rev. Mod. Phys.*, 21:392–399, Jul 1949.

[13] H. Leutwyler and J. Stern. Relativistic dynamics on a null plane. *Annals of Physics*, 112(1):94–164, 1978.

[14] Matthias Burkardt. Light front quantization. In *Advances in Nuclear Physics*, pages 1–74. Springer, 2002.

[15] H. Honkanen, P. Maris, J. P. Vary, and S. J. Brodsky. Electron in a transverse harmonic cavity. *Phys. Rev. Lett.*, 106:061603, Feb 2011.

[16] Stanley J. Brodsky, Dae Sung Hwang, Bo-Qiang Ma, and Ivan Schmidt. Light-cone representation of the spin and orbital angular momentum of relativistic composite systems. *Nuclear Physics B*, 593(1):311 – 335, 2001.

[17] Paul Wiecki, Yang Li, Xingbo Zhao, Pieter Maris, and James P. Vary. Basis light-front quantization approach to positronium. *Phys. Rev. D*, 91:105009, May 2015.

[18] George Leibbrandt. Light-cone gauge in Yang-Mills theory. *Phys. Rev. D*, 29:1699–1708, Apr 1984.

[19] Robert J. Perry, Avaroth Harindranath, and Kenneth G. Wilson. Light-front Tamm-Dancoff field theory. *Phys. Rev. Lett.*, 65:2959–2962, Dec 1990.

[20] John R. Hiller and Stanley J. Brodsky. Nonperturbative renormalization and the electron's anomalous moment in large-α QED. *Phys. Rev. D*, 59:016006, Dec 1998.

[21] V. A. Karmanov, J.-F. Mathiot, and A. V. Smirnov. Systematic renormalization scheme in light-front dynamics with Fock space truncation. *Phys. Rev. D*, 77:085028, Apr 2008.

[22] V. A. Karmanov, J.-F. Mathiot, and A. V. Smirnov. Nonperturbative calculation of the anomalous magnetic moment in the Yukawa model within truncated Fock space. *Phys. Rev. D*, 82:056010, Sep 2010.

[23] V. A. Karmanov, J.-F. Mathiot, and A. V. Smirnov. Ab initio nonperturbative calculation of physical observables in light-front dynamics: Application to the Yukawa model. *Phys. Rev. D*, 86:085006, Oct 2012.

[24] Yang Li, V.A. Karmanov, P. Maris, and J.P. Vary. Ab initio approach to the non-perturbative scalar Yukawa model. *Physics Letters B*, 748:278 – 283, 2015.

[25] Vladimir A. Karmanov, Yang Li, Alexander V. Smirnov, and James P. Vary. Nonperturbative solution of scalar Yukawa model in two- and three-body Fock space truncations. *Phys. Rev. D*, 94:096008, Nov 2016.

[26] Yang Li, V. A. Karmanov, P. Maris, and J. P. Vary. Non-perturbative calculation of the scalar Yukawa theory in four-body truncation. *Few-Body Systems*, 56(6):495–501, 2015.

[27] W. Zimmermann. Convergence of Bogolyubov's method of renormalization in momentum space. *Commun. Math. Phys.*, 15:217–243, 1969.

[28] Th. Heinzl, St. Krusche, and E. Werner. Spontaneous symmetry breaking in light cone quantum field theory. *Physics Letters B*, 272(1):54 – 60, 1991.

[29] Carl M. Bender, Stephen Pinsky, and Brett van de Sande. Spontaneous symmetry breaking of (1+1)-dimensional φ^4 theory in light-front field theory. *Phys. Rev. D*, 48:816–821, Jul 1993.

[30] A. C. Kalloniatis and H. C. Pauli. On zero modes and gauge fixing in light-cone quantized gauge theories. *Zeitschrift für Physik C Particles and Fields*, 63(1):161–168, 1994.

[31] Stephen S. Pinsky and Alex C. Kalloniatis. Light-front QCD (1+1) coupled to adjoint scalar matter. *Physics Letters B*, 365(1):225 – 232, 1996.

[32] Alex C. Kalloniatis, Hans-Christian Pauli, and Stephen Pinsky. Dynamical zero modes and pure glue (1+1)-dimensional QCD in light-cone field theory. *Phys. Rev. D*, 50:6633–6639, Nov 1994.

[33] Toshihide Maskawa and Koichi Yamawaki. The Problem of $P^+ = 0$ Mode in the Null-Plane Field Theory and Dirac's Method of Quantization. *Progress of Theoretical Physics*, 56(1):270–283, 07 1976.

[34] F. Lenz, M. Thies, S. Levit, and K. Yazaki. Hamiltonian formulation of two-dimensional gauge theories on the light cone. *Annals of Physics*, 208(1):1 – 89, 1991.

[35] Kent Hornbostel. Nontrivial vacua from equal time to the light cone. *Phys. Rev. D*, 45:3781–3801, May 1992.

[36] A. Harindranath and J. P. Vary. Stability of the vacuum in scalar field models in 1+1 dimensions. *Phys. Rev. D*, 37:1076–1078, Feb 1988.

[37] A. Harindranath and J. P. Vary. Light-front hamiltonian approach to relativistic two- and three-body bound-state problems in 1+1 dimensions. *Phys. Rev. D*, 37:1064–1069, Feb 1988.

[38] David G. Robertson. Spontaneous symmetry breaking in discretized light-cone field theory. *Phys. Rev. D*, 47:2549–2553, Mar 1993.

[39] Stephen S. Pinsky and Brett van de Sande. Spontaneous symmetry breaking of (1+1)-dimensional φ^4 theory in light-front field theory. ii. *Phys. Rev. D*, 49:2001–2013, Feb 1994.

84

[40] Stephen S. Pinsky, Brett van de Sande, and John R. Hiller. Spontaneous symmetry breaking of (1+1)-dimensional φ^4 theory in light-front field theory. iii. *Phys. Rev. D*, 51:726–733, Jan 1995.

[41] Hans-Christian Pauli and Stanley J. Brodsky. Solving field theory in one space and one time dimension. *Phys. Rev. D*, 32:1993–2000, Oct 1985.

[42] Hans-Christian Pauli and Stanley J. Brodsky. Discretized light-cone quantization: Solution to a field theory in one space and one time dimension. *Phys. Rev. D*, 32:2001–2013, Oct 1985.

[43] J. P. Vary, H. Honkanen, Jun Li, P. Maris, S. J. Brodsky, A. Harindranath, G. F. de Téramond, P. Sternberg, E. G. Ng, and C. Yang. Hamiltonian light-front field theory in a basis function approach. *Phys. Rev. C*, 81:035205, Mar 2010.

[44] J.P. Vary, H. Honkanen, Jun Li, P. Maris, S.J. Brodsky, A. Harindranath, G.F. de Téramond, P. Sternberg, E.G. Ng, and C. Yang. Hamiltonian light-front field theory within an AdS/QCD basis. *Nuclear Physics B - Proceedings Supplements*, 199(1):64 – 73, 2010.

[45] Andreas Karch, Emanuel Katz, Dam T. Son, and Mikhail A. Stephanov. Linear confinement and AdS/QCD. *Phys. Rev. D*, 74:015005, Jul 2006.

[46] Joshua Erlich, Emanuel Katz, Dam T. Son, and Mikhail A. Stephanov. QCD and a holographic model of hadrons. *Phys. Rev. Lett.*, 95:261602, Dec 2005.

[47] Pieter Maris, Paul Wiecki, Yang Li, Xingbo Zhao, and James P Vary. Bound state calculations in QED and QCD using basis light-front quantization. *Acta Phys. Polon. Supp*, 6:321, 2013.

[48] Yang Li, Pieter Maris, Xingbo Zhao, and James P. Vary. Heavy quarkonium in a holographic basis. *Physics Letters B*, 758:118 – 124, 2016.

[49] Yang Li, Pieter Maris, and James P. Vary. Quarkonium as a relativistic bound state on the light front. *Phys. Rev. D*, 96:016022, Jul 2017.

[50] Meijian Li, Xingbo Zhao, Pieter Maris, Guangyao Chen, Yang Li, Kirill Tuchin, and James P. Vary. Ultrarelativistic quark-nucleus scattering in a light-front Hamiltonian approach. *arXiv*, 2002.09757, 2020.

[51] Non-perturbative quantum time evolution on the light-front. *Physics Letters B*, 726(4):856 – 860, 2013.

[52] Xingbo Zhao, Anton Ilderton, Pieter Maris, and James P. Vary. Scattering in time-dependent basis light-front quantization. *Phys. Rev. D*, 88:065014, Sep 2013.

[53] Shuo Tang, Yang Li, Pieter Maris, and James P. Vary. B_c mesons and their properties on the light front. *Phys. Rev. D*, 98:114038, Dec 2018.

[54] Shuo Tang, Yang Li, Pieter Maris, and James P. Vary. Heavy-light mesons on the light front. *arXiv*, 1912.02088, 2019.

[55] N. Brambilla, S. Eidelman, B. K. Heltsley, R. Vogt, G. T. Bodwin, E. Eichten, A. D. Frawley, A. B. Meyer, R. E. Mitchell, V. Papadimitriou, and et al. Heavy quarkonium: progress, puzzles, and opportunities. *The European Physical Journal C*, 71(2):1534, 2011.

[56] Z. Q. Liu, C. P. Shen, C. Z. Yuan, I. Adachi, H. Aihara, D. M. Asner, V. Aulchenko, T. Aushev, T. Aziz, A. M. Bakich, and et al. Study of $e^+e^- \to \pi^+\pi^- J/\psi$ and observation of a charged charmoniumlike state at Belle. *Phys. Rev. Lett.*, 110:252002, Jun 2013.

[57] R. Aaij, B. Adeva, M. Adinolfi, A. Affolder, Z. Ajaltouni, S. Akar, J. Albrecht, F. Alessio, M. Alexander, S. Ali, and et al. Observation of $J/\psi p$ resonances consistent with pentaquark states in $\Lambda_b^0 \to J/\psi K^- p$ decays. *Phys. Rev. Lett.*, 115:072001, Aug 2015.

[58] W. Altmannshofer et al. The Belle II Physics Book. *PTEP*, 2019(12):123C01, 2019. [Erratum: PTEP2020, no.2, 029201(2020)].

[59] Stanley J. Brodsky, Guy F. de Téramond, Hans Gnter Dosch, and Joshua Erlich. Light-front holographic QCD and emerging confinement. *Physics Reports*, 584:1 – 105, 2015.

[60] Guy F. de Téramond and Stanley J. Brodsky. Light-front holography: A first approximation to QCD. *Phys. Rev. Lett.*, 102:081601, Feb 2009.

[61] George Sterman, John Smith, John C. Collins, James Whitmore, Raymond Brock, Joey Huston, Jon Pumplin, Wu-Ki Tung, Hendrik Weerts, Chien-Peng Yuan, Stephen Kuhlmann, Sanjib Mishra, Jorge G. Morfín, Fredrick Olness, Joseph Owens, Jianwei Qiu, and Davison E. Soper. Handbook of perturbative QCD. *Rev. Mod. Phys.*, 67:157–248, Jan 1995.

[62] S. A. Coon, M. I. Avetian, M. K. G. Kruse, U. van Kolck, P. Maris, and J. P. Vary. Convergence properties of ab initio calculations of light nuclei in a harmonic oscillator basis. *Phys. Rev. C*, 86:054002, Nov 2012.

[63] Hans Günter Dosch, Guy F. de Téramond, and Stanley J. Brodsky. Supersymmetry across the light and heavy-light hadronic spectrum. ii. *Phys. Rev. D*, 95:034016, Feb 2017.

[64] Particle Data Group. Review of particle physics. *Phys. Rev. D*, 98:030001, Aug 2018.

[65] Ian F. Allison, Christine T. H. Davies, Alan Gray, Andreas S. Kronfeld, Paul B. Mackenzie, and James N. Simone. Mass of the B_c meson in three-flavor lattice QCD. *Phys. Rev. Lett.*, 94:172001, May 2005.

[66] E. B. Gregory, C. T. H. Davies, E. Follana, E. Gamiz, I. D. Kendall, G. P. Lepage, H. Na, J. Shigemitsu, and K. Y. Wong. Prediction of the B_c^* mass in full lattice QCD. *Phys. Rev. Lett.*, 104:022001, Jan 2010.

[67] C.T.H. Davies, K. Hornbostel, G.P. Lepage, A.J. Lidsey, J. Shigemitsu, and J. Sloan. B_c spectroscopy from lattice QCD. *Phys. Lett. B*, 382(1):131 – 137, 1996.

[68] Eric B. Gregory, Christine T. H. Davies, Iain D. Kendall, Jonna Koponen, Kit Wong, Eduardo Follana, Elvira Gámiz, G. Peter Lepage, Eike H. Müller, Heechang Na, and Junko Shigemitsu. Precise B, B_s, and B_c meson spectroscopy from full lattice QCD. *Phys. Rev. D*, 83:014506, Jan 2011.

[69] R. J. Dowdall, C. T. H. Davies, T. C. Hammant, and R. R. Horgan. Precise heavy-light meson masses and hyperfine splittings from lattice QCD including charm quarks in the sea. *Phys. Rev. D*, 86:094510, Nov 2012.

[70] C.B. Lang, Daniel Mohler, Sasa Prelovsek, and R.M. Woloshyn. Predicting positive parity B_s mesons from lattice QCD. *Physics Letters B*, 750:17 – 21, 2015.

[71] Martin Kalinowski and Marc Wagner. Masses of D mesons, D_s mesons, and charmonium states from twisted-mass lattice QCD. *Phys. Rev. D*, 92:094508, Nov 2015.

[72] Shaoyang Jia and James P. Vary. Parton distribution functions from scalar light front parton gas model. *arXiv*, 1812.09340, 2018.

[73] Pieter Maris, Shaoyang Jia, Meijian Li, Yang Li, Shuo Tang, and James P. Vary. On the light-front wave functions of quarkonia. In *Light Cone 2019*, Feb 2020.

[74] Meijian Li, Yang Li, Pieter Maris, and James P. Vary. Radiative transitions between 0^{-+} and 1^{--} heavy quarkonia on the light front. *Phys. Rev. D*, 98:034024, Aug 2018.

[75] J. Koponen, A. C. Zimermmane-Santos, C. T. H. Davies, G. P. Lepage, and A. T. Lytle. Pseudoscalar meson electromagnetic form factor at high Q^2 from full lattice QCD. *Phys. Rev. D*, 96:054501, Sep 2017.

[76] B. Colquhoun, C. T. H. Davies, J. Kettle, J. Koponen, A. T. Lytle, R. J. Dowdall, and G. P. Lepage. B-meson decay constants: A more complete picture from full lattice QCD. *Phys. Rev. D*, 91:114509, Jun 2015.

[77] M. J. Baker, J. Bordes, C. A. Dominguez, J. Peñarrocha, and K. Schilcher. B meson decay constants f_{B_c}, f_{B_s} and f_B from QCD sum rules. *Journal of High Energy Physics*, 2014(7):32, Jul 2014.

[78] Zhi-Gang Wang. Analysis of the vector and axialvector B_c mesons with QCD sum rules. *The European Physical Journal A*, 49(10):131, Oct 2013.

[79] Ho-Meoyng Choi and Chueng-Ryong Ji. Semileptonic and radiative decays of the B_c meson in the light-front quark model. *Phys. Rev. D*, 80:054016, Sep 2009.

[80] A. Zupanc, I. Adachi, H. Aihara, K. Arinstein, D. M. Asner, T. Aushev, A. M. Bakich, A. Bala, B. Bhuyan, G. Bonvicini, and et al. Measurements of branching fractions of leptonic and hadronic D_s^+ meson decays and extraction of the D_s^+ meson decay constant. *Journal of High Energy Physics*, 2013(9):139, Sep 2013.

[81] B. I. Eisenstein, I. Karliner, S. Mehrabyan, N. Lowrey, M. Selen, E. J. White, J. Wiss, R. E. Mitchell, M. R. Shepherd, D. Besson, and et al. Precision measurement of $\mathcal{B}(D^+ \to \mu^+\nu)$ and the pseudoscalar decay constant f_{D^+}. *Phys. Rev. D*, 78:052003, Sep 2008.

[82] Zhi-Gang Wang. Analysis of the masses and decay constants of the heavy-light mesons with QCD sum rules. *The European Physical Journal C*, 75(9):427, Sep 2015.

[83] S. Aoki et al. FLAG Review 2019. *arXiv*, 1902.08191, 2019.

[84] V. Lubicz, A. Melis, and S. Simula. Masses and decay constants of $D_{(s)}^*$ and $B_{(s)}^*$ mesons with $N_f = 2 + 1 + 1$ twisted mass fermions. *Phys. Rev. D*, 96:034524, Aug 2017.

[85] Hao-Kai Sun and Mao-Zhi Yang. Wave functions and leptonic decays of bottom mesons in the relativistic potential model. *Phys. Rev. D*, 99:093002, May 2019.

[86] Chien-Wen Hwang. SU(3) symmetry breaking in decay constants and electromagnetic properties of pseudoscalar heavy mesons. *Phys. Rev. D*, 81:054022, Mar 2010.

[87] Mao-Zhi Yang. Wave functions and decay constants of B and D mesons in the relativistic potential model. *The European Physical Journal C*, 72(2):1880, Feb 2012.

[88] Damir Becirevic, Alain Le Yaouanc, Arantza Oyanguren, Patrick Roudeau, and Francesco Sanfilippo. Insight into $D/B \to \pi\ell\nu_\ell$ decay using the pole models. 2014.

[89] Wolfgang Lucha, Dmitri Melikhov, and Silvano Simula. QCD sum-rule results for heavy-light meson decay constants and comparison with lattice QCD. In *8th International Workshop on the CKM Unitarity Triangle (CKM 2014) Vienna, Austria, September 8-12, 2014*, 2014.

[90] Stephan Narison. Decay constants of heavy-light mesons from QCD. *Nuclear and Particle Physics Proceedings*, 270-272:143 – 153, 2016. 18th Montpellier International Conference on Quantum Chromodynamics (QCD 15).

[91] Shaoyang Jia and James P. Vary. Basis light front quantization for the charged light mesons with color singlet nambu–jona-lasinio interactions. *Phys. Rev. C*, 99:035206, Mar 2019.

[92] Jiangshan Lan, Chandan Mondal, Shaoyang Jia, Xingbo Zhao, and James P. Vary. Parton distribution functions from a light front hamiltonian and QCD evolution for light mesons. *Phys. Rev. Lett.*, 122:172001, May 2019.

[93] G. Peter Lepage and Stanley J. Brodsky. Exclusive processes in perturbative quantum chromodynamics. *Phys. Rev. D*, 22:2157–2198, Nov 1980.

[94] Daniele Binosi, Lei Chang, Minghui Ding, Fei Gao, Joannis Papavassiliou, and Craig D. Roberts. Distribution amplitudes of heavy-light mesons. *Physics Letters B*, 790:257 – 262, 2019.

[95] Matthias Burkardt. Impact parameter space interpretation for generalized parton distributions. *International Journal of Modern Physics A*, 18(02):173–207, 2003.

[96] Gerald A. Miller. Charge densities of the neutron and proton. *Phys. Rev. Lett.*, 99:112001, Sep 2007.

[97] Matthias Burkardt. Impact parameter dependent parton distributions and off-forward parton distributions for $\overrightarrow{\zeta}$ 0. *Phys. Rev. D*, 62:071503, Sep 2000.

[98] J. P. Lees, V. Poireau, V. Tisserand, J. Garra Tico, E. Grauges, A. Palano, G. Eigen, B. Stugu, D. N. Brown, and et al. Evidence for an excess of $\overline{B} \to D^{(*)}\tau^-\overline{\nu}_\tau$ decays. *Phys. Rev. Lett.*, 109:101802, Sep 2012.

[99] M. Huschle, T. Kuhr, M. Heck, P. Goldenzweig, A. Abdesselam, I. Adachi, K. Adamczyk, H. Aihara, S. Al Said, K. Arinstein, and et al. Measurement of the branching ratio of $\overline{B} \to D^{(*)}\tau^-\overline{\nu}_\tau$ relative to $\overline{B} \to D^{(*)}\ell^-\overline{\nu}_\ell$ decays with hadronic tagging at Belle. *Phys. Rev. D*, 92:072014, Oct 2015.

[100] Y. Sato, T. Iijima, K. Adamczyk, H. Aihara, D. M. Asner, H. Atmacan, T. Aushev, R. Ayad, T. Aziz, V. Babu, and et al. Measurement of the branching ratio of $\overline{B}^0 \to D^{*+}\tau^-\overline{\nu}_\tau$ relative to $\overline{B}^0 \to D^{*+}\ell^-\overline{\nu}_\ell$ decays with a semileptonic tagging method.

[101] S. Hirose, T. Iijima, I. Adachi, K. Adamczyk, H. Aihara, S. Al Said, D. M. Asner, H. Atmacan, V. Aulchenko, T. Aushev, and et al. Measurement of the τ lepton polarization and $R(D^*)$ in the decay $\overline{B} \to D^*\tau^-\overline{\nu}_\tau$. *Phys. Rev. Lett.*, 118:211801, May 2017.

[102] R. Aaij, B. Adeva, M. Adinolfi, A. Affolder, Z. Ajaltouni, S. Akar, J. Albrecht, F. Alessio, M. Alexander, S. Ali, and et al. Measurement of the ratio of branching fractions $\mathcal{B}(\overline{B}^0 \to D^{*+}\tau^-\overline{\nu}_\tau)/\mathcal{B}(\overline{B}^0 \to D^{*+}\mu^-\overline{\nu}_\mu)$. *Phys. Rev. Lett.*, 115:111803, Sep 2015.

[103] R. Aaij, B. Adeva, M. Adinolfi, Z. Ajaltouni, S. Akar, J. Albrecht, F. Alessio, M. Alexander, A. Alfonso Albero, S. Ali, and et al. Measurement of the ratio of the $B^0 \to D^{*-}\tau^+\nu_\tau$ and $B^0 \to D^{*-}\mu^+\nu_\mu$ branching fractions using three-prong τ-lepton decays. *Phys. Rev. Lett.*, 120:171802, Apr 2018.

[104] R. Aaij, B. Adeva, M. Adinolfi, Z. Ajaltouni, S. Akar, J. Albrecht, F. Alessio, M. Alexander, A. Alfonso Albero, S. Ali, and et al. Measurement of the ratio of branching fractions $\mathcal{B}(B_c^+ \to J/\psi\tau^+\nu_\tau)/\mathcal{B}(B_c^+ \to J/\psi\mu^+\nu_\mu)$. *Phys. Rev. Lett.*, 120:121801, Mar 2018.

[105] Bernard L. G. Bakker, Ho-Meoyng Choi, and Chueng-Ryong Ji. Transition form factors between pseudoscalar and vector mesons in light-front dynamics. *Phys. Rev. D*, 67:113007, Jun 2003.

[106] Wolfgang Jaus. Semileptonic, radiative, and pionic decays of B, B^* and D, D^* mesons. *Phys. Rev. D*, 53:1349–1365, Feb 1996.

[107] Wei Wang, Yue-Long Shen, and Cai-Dian Lü. Covariant light-front approach for B_c transition form factors. *Phys. Rev. D*, 79:054012, Mar 2009.

[108] C. T. Tran, M. A. Ivanov, J. G. Körner, and P. Santorelli. Implications of new physics in the decays $B_c \to (J/\psi, \eta_c)\tau\nu$. *Phys. Rev. D*, 97:054014, Mar 2018.

[109] V.V. Kiselev, A.K. Likhoded, and A.I. Onishchenko. Semileptonic B_c meson decays in sum rules of QCD and NRQCD. *Nuclear Physics B*, 569(1):473 – 504, 2000.

[110] Wen-Fei Wang, Ying-Ying Fan, and Zhen-Jun Xiao. Semileptonic decays $B_c \to (\eta_c, J/\psi)\nu$ in the perturbative QCD approach. *Chinese Physics C*, 37(9):093102, sep 2013.

[111] Aidos Issadykov and Mikhail A. Ivanov. The decays $B_c \to J/\psi + \bar{l}\nu_l$ and $B_c \to J/\psi + \pi(K)l$ in covariant confined quark model. *Physics Letters B*, 783:178 – 182, 2018.

[112] Rohit Dhir and R. C. Verma. B_c meson form factors and $B_c \to PV$ decays involving flavor dependence of transverse quark momentum. *Phys. Rev. D*, 79:034004, Feb 2009.

[113] Zhou Rui, Hong Li, Guang-xin Wang, and Ying Xiao. Semileptonic decays of B_c meson to S-wave charmonium states in the perturbative QCD approach. *The European Physical Journal C*, 76(10):564, 2016.

[114] E. Hernández, J. Nieves, and J. M. Verde-Velasco. Study of exclusive semileptonic and nonleptonic decays of B_c^- in a nonrelativistic quark model. *Phys. Rev. D*, 74:074008, Oct 2006.

[115] Yang Li, Pieter Maris, and James P. Vary. Frame dependence of form factors in light-front dynamics. *Phys. Rev. D*, 97:054034, Mar 2018.

[116] Meijian Li, Yang Li, Pieter Maris, and James P. Vary. Frame dependence of transition form factors in light-front dynamics. *Phys. Rev. D*, 100:036006, Aug 2019.

[117] Timothy Altomari and Lincoln Wolfenstein. Constraints on semileptonic B decays from the measurement of the D^* polarization in $B \to D^* e\bar{\nu}$. *Phys. Rev. D*, 37:681–687, Feb 1988.

[118] Ho-Meoyng Choi and Chueng-Ryong Ji. Kaon electroweak form factors in the light-front quark model. *Phys. Rev. D*, 59:034001, Dec 1998.

[119] M. Wirbel, B. Stech, and M. Bauer. Exclusive semileptonic decays of heavy mesons. *Zeitschrift für Physik C Particles and Fields*, 29(4):637–642, 1985.

[120] M. Bauer and M. Wirbel. Formfactor effects in exclusive D and B decays. *Zeitschrift für Physik C Particles and Fields*, 42(4):671–678, 1989.

[121] Stanley J. Brodsky, Ralph Roskies, and Roberto Suaya. Quantum electrodynamics and renormalization theory in the infinite-momentum frame. *Phys. Rev. D*, 8:4574–4594, Dec 1973.

[122] Stanley J. Brodsky and Sidney D. Drell. Anomalous magnetic moment and limits on fermion substructure. *Phys. Rev. D*, 22:2236–2243, Nov 1980.

[123] Stanley J. Brodsky and Dae Sung Hwang. Exact light-cone wavefunction representation of matrix elements of electroweak currents. *Nuclear Physics B*, 543(1):239 – 252, 1999.

[124] D. Ebert, R. N. Faustov, and V. O. Galkin. Weak decays of the B_c meson to charmonium and D mesons in the relativistic quark model. *Phys. Rev. D*, 68:094020, Nov 2003.

[125] Brian Colquhoun, Christine Davies, Jonna Koponen, Andrew Lytle, and Craig McNeile. B_c decays from highly improved staggered quarks and NRQCD. *PoS*, LATTICE2016:281, 2016.

[126] William Gropp, William D Gropp, Ewing Lusk, Argonne Distinguished Fellow Emeritus Ewing Lusk, and Anthony Skjellum. *Using MPI: portable parallel programming with the message-passing interface*, volume 1. MIT press, 1999.

[127] A. Basumallik, S. Min, and R. Eigenmann. Programming distributed memory systems using openmp. In *2007 IEEE International Parallel and Distributed Processing Symposium*, pages 1–8, 2007.

[128] D. Chakrabarti, X. Zhao, H. Honkanen, R. Manohar, P. Maris, and J. P. Vary. Generalized parton distributions in a light-front nonperturbative approach. *Phys. Rev. D*, 89:116004, Jun 2014.

[129] Xingbo Zhao, Heli Honkanen, Pieter Maris, James P. Vary, and Stanley J. Brodsky. Electron g-2 in light-front quantization. *Physics Letters B*, 737(Supplement C):65 – 69, 2014.

[130] Yang Li, Paul W. Wiecki, Xingbo Zhao, Pieter Maris, and James P. Vary. Introduction to Basis Light-Front Quantization Approach to QCD Bound State Problems. In *Proceedings, International Conference on Nuclear Theory in the Supercomputing Era (NTSE-2013)*, page 136, May 2013.

[131] P. E. Shanahan and W. Detmold. Gluon gravitational form factors of the nucleon and the pion from lattice QCD. *Phys. Rev. D*, 99:014511, Jan 2019.

[132] Maxim V. Polyakov and Peter Schweitzer. Forces inside hadrons: Pressure, surface tension, mechanical radius, and all that. *International Journal of Modern Physics A*, 33(26):1830025, 2018.

[133] V. D. Burkert, L. Elouadrhiri, and F. X. Girod. The pressure distribution inside the proton. *Nature*, 557(7705):396–399, 2018.

[134] Kazuhiro Tanaka. Operator relations for gravitational form factors of a spin-0 hadron. *Phys. Rev. D*, 98:034009, Aug 2018.

[135] Xiangdong Ji. Deeply virtual compton scattering. *Phys. Rev. D*, 55:7114–7125, Jun 1997.

[136] M. Diehl. Generalized parton distributions. *Physics Reports*, 388(2):41 – 277, 2003.

[137] K. Goeke, M.V. Polyakov, and M. Vanderhaeghen. Hard exclusive reactions and the structure of hadrons. *Progress in Particle and Nuclear Physics*, 47(2):401 – 515, 2001.

[138] A. Accardi, J. L. Albacete, M. Anselmino, N. Armesto, E. C. Aschenauer, A. Bacchetta, D. Boer, W. K. Brooks, T. Burton, N. B. Chang, and title= et al.

[139] N Kalantarians. Tensor polarized deuteron at an electron-ion collider. *Journal of Physics: Conference Series*, 543:012008, Oct 2014.

[140] Paul Hoyer and Samu Kurki. Transverse shape of the electron. *Phys. Rev. D*, 81:013002, Jan 2010.

[141] Gerald A. Miller. Electron structure: Shape, size, and generalized parton distributions in QED. *Phys. Rev. D*, 90:113001, Dec 2014.

[142] L. Mantovani, A. Bacchetta, and B. Pasquini. The Electron in Three-Dimensional Momentum Space. *Few Body Syst.*, 57(7):515–519, 2016.

[143] Matthias Burkardt and Hikmat BC. Angular momentum decomposition for an electron. *Phys. Rev. D*, 79:071501, Apr 2009.

[144] Tianbo Liu and Bo-Qiang Ma. Angular momentum decomposition from a QED example. *Phys. Rev. D*, 91:017501, Jan 2015.

[145] Xiangdong Ji, Andreas Schäfer, Feng Yuan, Jian-Hui Zhang, and Yong Zhao. Spin decomposition of the electron in QED. *Phys. Rev. D*, 93:054013, Mar 2016.

[146] X. Zhao, H. Honkanen, P. Maris, J. P. Vary, and S. J. Brodsky. Electron anomalous magnetic moment in basis light-front quantization approach. *Few-Body Systems*, 52(3):339–344, May 2012.

[147] S.J. Brodsky, V.A. Franke, J.R. Hiller, G. McCartor, S.A. Paston, and E.V. Prokhvatilov. A nonperturbative calculation of the electron's magnetic moment. *Nuclear Physics B*, 703(1):333 – 362, 2004.

[148] Stanley J. Brodsky, Markus Diehl, and Dae Sung Hwang. Light-cone wavefunction representation of deeply virtual compton scattering. *Nuclear Physics B*, 596(1):99 – 124, 2001.

[149] Stanley J. Brodsky, Susan Gardner, and Dae Sung Hwang. Discrete symmetries on the light front and a general relation connecting the nucleon electric dipole and anomalous magnetic moments. *Phys. Rev. D*, 73:036007, Feb 2006.

[150] Xiangdong Ji. Gauge-invariant decomposition of nucleon spin. *Phys. Rev. Lett.*, 78:610–613, Jan 1997.

[151] R. G. Sachs. High-energy behavior of nucleon electromagnetic form factors. *Phys. Rev.*, 126:2256–2260, Jun 1962.

[152] Zainul Abidin and Carl E. Carlson. Hadronic momentum densities in the transverse plane. *Phys. Rev. D*, 78:071502, Oct 2008.

[153] O. V. Selyugin and O. V. Teryaev. Generalized parton distributions and description of electromagnetic and graviton form factors of nucleon. *Phys. Rev. D*, 79:033003, Feb 2009.

[154] Dipankar Chakrabarti, Chandan Mondal, and Asmita Mukherjee. Gravitational form factors and transverse spin sum rule in a light front quark-diquark model in AdS/QCD. *Phys. Rev. D*, 91:114026, Jun 2015.

[155] C. Mondal, N. Kumar, H. Dahiya, and D. Chakrabarti. Charge and longitudinal momentum distributions in transverse coordinate space. *Phys. Rev. D*, 94:074028, Oct 2016.

[156] S. Meißner, A. Metz, and K. Goeke. Relations between generalized and transverse momentum dependent parton distributions. *Phys. Rev. D*, 76:034002, Aug 2007.

[157] Xiangdong Ji. Lorentz symmetry and the internal structure of the nucleon. *Phys. Rev. D*, 58:056003, Jul 1998.

[158] O. V. Teryaev. Equivalence principle and partition of angular momenta in the nucleon. *AIP Conference Proceedings*, 915(1):260–263, 2007.

[159] O. V. Teryaev. Gravitational form factors and nucleon spin structure. *Frontiers of Physics*, 11(5):111207, Apr 2016.

[160] S. Kumano, Qin-Tao Song, and O. V. Teryaev. Hadron tomography by generalized distribution amplitudes in the pion-pair production process $\gamma^*\gamma \to \pi^0\pi^0$ and gravitational form factors for pion. *Phys. Rev. D*, 97:014020, Jan 2018.

APPENDIX A. CONVENTIONS

A.1 Gamma Matrix

In this convention, the 4×4 gamma matrices are defined as (cf. Dirac and chiral representation):

$$\gamma^0 = \begin{pmatrix} 0 & -i \\ i & 0 \end{pmatrix}, \quad \gamma^1 = \begin{pmatrix} -i\sigma^2 & 0 \\ 0 & i\sigma^2 \end{pmatrix}, \quad \gamma^2 = \begin{pmatrix} i\sigma^1 & 0 \\ 0 & -i\sigma^1 \end{pmatrix}, \quad \gamma^3 = \begin{pmatrix} 0 & i \\ i & 0 \end{pmatrix}, \tag{A.1}$$

where $\sigma = (1, \vec{\sigma})$ are the standard Pauli matrices,

$$\sigma^0 = \begin{pmatrix} 1 & 0 \\ 0 & 1 \end{pmatrix}, \quad \sigma^1 = \begin{pmatrix} 0 & 1 \\ 1 & 0 \end{pmatrix}, \quad \sigma^2 = \begin{pmatrix} 0 & -i \\ i & 0 \end{pmatrix}, \quad \sigma^3 = \begin{pmatrix} 1 & 0 \\ 0 & -1 \end{pmatrix} \tag{A.2}$$

It is convenient to introduce the following 4×4 matrices in the front form:

$$\gamma^+ = \gamma^0 + \gamma^3 = \begin{pmatrix} 0 & 0 \\ 2i & 0 \end{pmatrix}, \qquad \gamma^- = \gamma^0 - \gamma^3 = \begin{pmatrix} 0 & -2i \\ 0 & 0 \end{pmatrix},$$

$$\gamma^L = \gamma^1 - i\gamma^2 = \begin{pmatrix} \sigma^L & 0 \\ 0 & -\sigma^L \end{pmatrix}, \qquad \gamma^R = \gamma^1 + i\gamma^2 = \begin{pmatrix} -\sigma^R & 0 \\ 0 & \sigma^R \end{pmatrix}, \tag{A.3}$$

where

$$\sigma^L = \sigma^1 - i\sigma^2 = \begin{pmatrix} 0 & 0 \\ 2 & 0 \end{pmatrix}, \qquad \sigma^R = \sigma^1 + i\sigma^2 = \begin{pmatrix} 0 & 2 \\ 0 & 0 \end{pmatrix}. \tag{A.4}$$

- projections:

$$\Lambda^+ = \Lambda_+ = \frac{1}{2}\gamma^0\gamma^+ = \begin{pmatrix} 1 & 0 \\ 0 & 0 \end{pmatrix}, \quad \Lambda^- = \Lambda_- = \frac{1}{2}\gamma^0\gamma^- = \begin{pmatrix} 0 & 0 \\ 0 & 1 \end{pmatrix}. \tag{A.5}$$

corollaries: $\Lambda_\pm^2 = \Lambda_\pm$, $\Lambda^+\Lambda^- = 0$, $\Lambda_\pm^\dagger = \Lambda_\pm$, $\overline{\Lambda}_\pm = \Lambda_\mp$.

A.2 Dirac Spinors

The Dirac spinor of the fermion (u) and anti-fermion (v) are defined as,

$$u_s(p) = \frac{1}{2\sqrt{p^+}}(\not{p} + m)\gamma^+ \chi_s = \frac{1}{\sqrt{p^+}}(\not{p} + m)\beta\chi_s = \frac{1}{\sqrt{p^+}}(p^+ + \boldsymbol{\alpha}^\perp \cdot \boldsymbol{p}^\perp + \beta m)\chi_s \; ;$$

$$v_s(p) = \frac{1}{2\sqrt{p^+}}(\not{p} - m)\gamma^+ \chi_{-s} = \frac{1}{\sqrt{p^+}}(\not{p} - m)\beta\chi_{-s} = \frac{1}{\sqrt{p^+}}(p^+ + \boldsymbol{\alpha}^\perp \cdot \boldsymbol{p}^\perp - \beta m)\chi_{-s}$$

(A.6)

where $\chi_+ = (1, 0, 0, 0)^\intercal$, $\chi_- = (0, 1, 0, 0)^\intercal$ are the basis of the two-component spinors (the dynamical spinors on the light front). They satisfy

$$\Lambda_+ \chi_s = \chi_s, \quad \Lambda_- \chi_s = 0, \quad \chi_s^\dagger \chi_{s'} = \delta_{ss'}, \quad S_z \chi_\pm = \pm\frac{1}{2}\chi_\pm. \tag{A.7}$$

A.2.1 The spinor identities

- Dirac equation:

$$(\not{p} - m)u_\sigma(p) = 0, \qquad (\not{p} + m)v_\sigma(p) = 0; \tag{A.8}$$

- normalization:

$$\bar{u}_s(p)u_{s'}(p) = 2m\delta_{ss'}, \qquad \bar{v}_s(p)v_{s'}(p) = -2m\delta_{ss'}, \qquad \bar{u}_s(p)v_{s'}(p) = 0;$$

$$\sum_{s=\pm\frac{1}{2}} u_s(p)\bar{u}_s(p) = \not{p} + m, \qquad \sum_{s=\pm\frac{1}{2}} v_s(p)\bar{v}_s(p) = \not{p} - m; \tag{A.9}$$

- crossing symmetry

$$u_s(p) = \mathrm{i}v_{-s}(-p), \quad \bar{u}_s(p) = \mathrm{i}\bar{v}_{-s}(-p), \quad v_s(p) = \mathrm{i}u_{-s}(-p), \quad \bar{v}_s(p) = \mathrm{i}\bar{u}_{-s}(-p)^1; \tag{A.10}$$

---

[1] Note that $p \to -p$ flipsthe signs of all four components of the momentum, including the light-front energy and the longitudinal momentum.

- Gordon identities

$$2m\bar{u}_{s'}(p')\gamma^\mu u_s(p) = \bar{u}_{s'}(p')\left[(p+p')^\mu + 2\mathrm{i}S^{\mu\nu}(p'-p)_\nu\right]u_s(p);$$

$$2m\bar{v}_{s'}(p')\gamma^\mu v_s(p) = -\bar{v}_{s'}(p')\left[(p+p')^\mu + 2\mathrm{i}S^{\mu\nu}(p'-p)_\nu\right]v_s(p);$$

$$2m\bar{u}_{s'}(p')\gamma^\mu v_s(p) = \bar{u}_{s'}(p')\left[(p'-p)^\mu + 2\mathrm{i}S^{\mu\nu}(p'+p)_\nu\right]v_s(p);$$

$$2m\bar{u}_{s'}(p')\gamma^\mu\gamma_5 u_s(p) = \bar{u}_{s'}(p')\left[(p-p')^\mu\gamma_5 + 2\mathrm{i}S^{\mu\nu}(p'+p)_\nu\gamma_5\right]u_s(p); \tag{A.11}$$

$$0 = \bar{u}_{s'}(p')\left[(p'-p)^\mu + 2\mathrm{i}S^{\mu\nu}(p'+p)_\nu\right]u_s(p);$$

$$0 = \bar{u}_{s'}(p')\left[(p'-p)^\mu\gamma_5 + 2\mathrm{i}S^{\mu\nu}(p'+p)_\nu\gamma_5\right]u_s(p);$$

- other useful identities

$$\bar{u}_s(p)\gamma^\mu u_{s'}(p) = \bar{v}_s(p)\gamma^\mu v_{s'}(p) = 2p^\mu\delta_{ss'};$$

$$\bar{u}_s(p)\gamma^0 v_{s'}(-p) = 0 \tag{A.12}$$

A.2.2 The spinor vertices

scalar vertex

$$\bar{u}_{s'}(p')u_s(p) = \sqrt{p^+ p'^+} \times \begin{cases} \dfrac{m_1}{p^+} + \dfrac{m_2}{p'^+} & s,s' = +,+ \text{ or } -,- \\[2mm] \dfrac{p^R}{p^+} - \dfrac{p'^P}{p'^+} & s,s' = +,- \\[2mm] \dfrac{p'^L}{p'^+} - \dfrac{p^L}{p^+} & s,s' = -,+ \end{cases} \tag{A.13}$$

pseudo scalar vertex

$$\bar{u}_{s'}(p')\gamma_5 u_s(p) = \sqrt{p^+ p'^+} \times \begin{cases} \dfrac{m_2}{p'^+} - \dfrac{m_1}{p^+} & s,s' = +,+ \\[2mm] \dfrac{m_1}{p^+} - \dfrac{m_2}{p'^+} & s,s' = -,- \\[2mm] \dfrac{p^R}{p^+} - \dfrac{p'^P}{p'^+} & s,s' = +,- \\[2mm] \dfrac{p^L}{p^+} - \dfrac{p'^L}{p'^+} & s,s' = -,+ \end{cases} \tag{A.14}$$

vector vertex

$$\bar{u}_{s'}(p')\gamma^+ u_s(p) = 2\sqrt{p^+ p'^+}\delta_{ss'} \tag{A.15}$$

$$\bar{u}_{s'}(p')\gamma^- u_s(p) = \frac{2}{\sqrt{p^+ p'^+}} \times \begin{cases} m_1 m_2 + p^R p'^L & s, s' = +, + \\ m_1 m_2 + p^L p'^R & s, s' = -, - \\ m_2 p^R - m_1 p'^R & s, s' = +, - \\ m_1 p'^L - m_2 p^L & s, s' = -, + \end{cases} \tag{A.16}$$

$$\bar{u}_{s'}(p')\gamma^L u_s(p) = 2\sqrt{p^+ p'^+} \times \begin{cases} \dfrac{p'^L}{p'^+} & s, s' = +, + \\[2mm] \dfrac{p^L}{p^+} & s, s' = -, - \\[2mm] \dfrac{m_2}{p'^+} - \dfrac{m_1}{p^+} & s, s' = +, - \\[2mm] 0 & s, s' = -, + \end{cases} \tag{A.17}$$

$$\bar{u}_{s'}(p')\gamma^R u_s(p) = 2\sqrt{p^+ p'^+} \times \begin{cases} \dfrac{p^R}{p^+} & s, s' = +, + \\[2mm] \dfrac{p'^R}{p'^+} & s, s' = -, - \\[2mm] 0 & s, s' = +, - \\[2mm] \dfrac{m_1}{p^+} - \dfrac{m_2}{p'^+} & s, s' = -, + \end{cases} \tag{A.18}$$

axial vector vertex

$$\bar{u}_{s'}(p')\gamma^+ \gamma_5 u_s(p) = 2\sqrt{p^+ p'^+}\, \delta_{ss'} \mathrm{sign}(s) \tag{A.19}$$

$$\bar{u}_{s'}(p')\gamma^- \gamma_5 u_s(p) = \frac{2}{\sqrt{p^+ p'^+}} \times \begin{cases} -m_1 m_2 + p^R p'^L & s, s' = +, + \\ m_1 m_2 - p^L p'^R & s, s' = -, - \\ m_2 p^R + m_1 p'^R & s, s' = +, - \\ m_1 p'^L + m_2 p^L & s, s' = -, + \end{cases} \tag{A.20}$$

98

$$\bar{u}_{s'}(p')\gamma^L\gamma_5 u_s(p) = 2\sqrt{p^+p'^+} \times \begin{cases} \dfrac{p'^L}{p'^+} & s,s' = +,+ \\[2mm] -\dfrac{p^L}{p^+} & s,s' = -,- \\[2mm] \dfrac{m_1}{p^+} + \dfrac{m_2}{p'^+} & s,s' = +,- \\[2mm] 0 & s,s' = -,+ \end{cases} \quad (A.21)$$

$$\bar{u}_{s'}(p')\gamma^R\gamma_5 u_s(p) = 2\sqrt{p^+p'^+} \times \begin{cases} \dfrac{p^R}{p^+} & s,s' = +,+ \\[2mm] -\dfrac{p'^R}{p'^+} & s,s' = -,- \\[2mm] 0 & s,s' = +,- \\[2mm] \dfrac{m_1}{p^+} + \dfrac{m_2}{p'^+} & s,s' = -,+ \end{cases} \quad (A.22)$$

A.3 Polarization Vector

Define the polarization vector for the massless bosons:

$$\varepsilon_\lambda^\mu(k) = (\varepsilon_\lambda^+, \vec{\varepsilon}_\lambda^\perp, \varepsilon_\lambda^-) = \left(0, \vec{\epsilon}_\lambda^\perp, \frac{2\vec{\epsilon}_\lambda^\perp \cdot \vec{k}^\perp}{k^+}\right), \qquad (\lambda = \pm 1) \quad (A.23)$$

where $\vec{\epsilon}_\pm^\perp = \frac{1}{\sqrt{2}}(1, \pm i)$, so that $\epsilon_\lambda^L = \sqrt{2}\delta_{\lambda,+}$, $\epsilon_\lambda^R = \sqrt{2}\delta_{\lambda,-}$. This definition satisfies the light-cone gauge $\omega \cdot A = A^+ = 0$ and the Lorentz condition $\partial_\mu A^\mu = 0$, and

$$\omega_\mu \varepsilon_\lambda^\mu(k) = \varepsilon_\lambda^+(k) = 0, \qquad k_\mu \epsilon_\lambda^\mu(k) = 0, \quad (A.24)$$

with $\omega^\mu = (1,0,0,-1)$ the null normal vector of the light front: $\omega \cdot \omega = 0$, and $\omega \cdot v = v^+$.

A.3.1 The polarization identities

- orthogonality

$$\varepsilon_\lambda^\mu(k)\varepsilon_{\lambda'\mu}^*(k) = -\delta_{\lambda\lambda'}; \quad (A.25)$$

- helicity sum

$$\sum_{\lambda=\pm} \varepsilon_\lambda^{i*}(k)\varepsilon_\lambda^j(k) = \delta^{ij}, \qquad \sum_{\lambda=\pm} \varepsilon_\lambda^{\mu*}(k)\varepsilon_\lambda^\nu(k) = -g^{\mu\nu} + \frac{\omega^\mu k^\nu + \omega^\nu k^\mu}{\omega \cdot k} - \omega^\mu\omega^\nu\frac{k^2}{(\omega \cdot k)^2}. \quad (A.26)$$

In particular, if the particle is on shell (i.e. $k^2 = 0$), the second identity reduced to

$$\sum_{\lambda=\pm} \varepsilon_\lambda^{\mu,*}(k)\varepsilon_\lambda^\nu(k) = -g^{\mu\nu} + \frac{\omega^\mu k^\nu + \omega^\nu k^\mu}{\omega \cdot k}; \tag{A.27}$$

- crossing symmetry

$$\varepsilon_\lambda^{\mu*}(k) = \varepsilon_{-\lambda}^\mu(k). \tag{A.28}$$

A.4   Spinor Vector

Define the spin vector for the massive vector bosons:

$$e_\lambda(k) = \left(e_\lambda^+(k), \vec{e}_\lambda^\perp(k), e_\lambda^-(k)\right) = \begin{cases} \left(\dfrac{k^+}{m}, \dfrac{\vec{k}^\perp}{m}, \dfrac{\vec{k}_\perp^2 - m^2}{mk^+}\right) & \lambda = 0 \\[3mm] \left(0, \vec{\epsilon}_\lambda^\perp, \dfrac{2\vec{\epsilon}_\lambda^\perp \cdot \vec{k}^\perp}{k^+}\right) & \lambda = \pm \end{cases}, \tag{A.29}$$

where $m^2 = k^2$ is the mass of the particle.

A.4.1   The spin identities

- Proca equation

$$k_\mu e_\lambda^\mu(k) = 0 \tag{A.30}$$

- orthogonality

$$e_\lambda^\mu(k)e_{\lambda'\mu}^*(k) = -\delta_{\lambda\lambda'}; \tag{A.31}$$

- spin sum

$$K^{\mu\nu} \triangleq \sum_{\lambda=\pm} e_\lambda^{\mu*}(k)e_\lambda^\nu(k) = -g^{\mu\nu} + \frac{k^\mu k^\nu}{k^2},$$

$$k^\mu k^\nu K_{\mu\nu}(k) = 0 \tag{A.32}$$

- crossing symmetry

$$e_\lambda^{\mu*}(k) = e_{-\lambda}^\mu(k), \qquad e_\lambda^\mu(-k) = (-1)^{\lambda+1}e_\lambda^\mu(k). \tag{A.33}$$

APPENDIX B.   ONE-GLUON EXCHANGE

The one-gluon exchange matrix element in the basis space can be expresses as,

$$\langle n', m', l', s', \bar{s}' | V_g | n, m, l, s, \bar{s} \rangle$$

$$= - \frac{N_c^2 - 1}{2 N_c} \int_0^1 \frac{dx}{2x(1-x)} \chi_l(x) \int \frac{d^2 p_\perp}{(2\pi)^3} \phi_{nm} \left(\vec{p}_\perp / \sqrt{x(1-x)} \right)$$

$$\times \int_0^1 \frac{dx'}{2x'(1-x')} \chi_{l'}(x') \int \frac{d^2 p'_\perp}{(2\pi)^3} \phi^*_{n'm'} \left(\vec{p}'_\perp / \sqrt{x'(1-x')} \right) \frac{4\pi\alpha_s}{Q^2} \left[\bar{u}_{s'}(p'_1) \gamma_\mu u_s(p_1) \right] \left[\bar{v}_{\bar{s}}(p_2) \gamma^\mu v_{\bar{s}'}(p'_2) \right]$$

$$= - \frac{N_c^2 - 1}{2 N_c} \int_0^1 \frac{dx}{4\pi} \chi_l(x) \int_0^1 \frac{dx'}{4\pi} \chi_{l'}(x') \int \frac{d^2 q_\perp}{(2\pi)^2} \phi_{nm}(\vec{q}_\perp) \int \frac{d^2 q'_\perp}{(2\pi)^2} \phi^*_{n'm'}(\vec{q}'_\perp) \times$$

$$\times \frac{4\pi\alpha_s}{Q^2} \left[\bar{u}_{s'}(p'_1) \gamma_\mu u_s(p_1) \right] \left[\bar{v}_{\bar{s}}(p_2) \gamma^\mu v_{\bar{s}'}(p'_2) \right],$$

$$(B.1)$$

where $\vec{q}_\perp = \frac{\vec{p}_\perp}{\sqrt{x(1-x)}}, \vec{q}'_\perp = \frac{\vec{p}'_\perp}{\sqrt{x'(1-x')}}$ and

$$Q^2 = \frac{1}{2} \left(\sqrt{x'(1-x)} - \sqrt{x(1-x')} \right)^2 \vec{q}_\perp^2 + \frac{1}{2} \left(\sqrt{x'(1-x)} + \sqrt{x(1-x')} \right)^2 \vec{q}'^2_\perp$$

$$+ \frac{1}{2}(x - x')^2 \left(\frac{m_q^2}{xx'} + \frac{m_a^2}{(1-x)(1-x')} + 2\mu_g^2 \right).$$

$$(B.2)$$

The strategy is that, we first calculate the integral of transverse direction, by sorting the integrands with different $q_\perp (q'_\perp)$ contributing by the spinor part. Then take care of the integral over x, i.e. the longitudinal direction. The reason why we do so is to take advantage of the HO basis in the transverse direction:

$$q \phi_n^m(\vec{q}_\perp) = b \begin{cases} \sqrt{n + |m| + 1} \phi_n^{m+1}(\vec{q}_\perp) - \sqrt{n} \phi_{n-1}^{m+1}(\vec{q}_\perp) & m \geq 0 \\ \sqrt{n + |m|} \phi_n^{m+1}(\vec{q}_\perp) - \sqrt{n+1} \phi_{n+1}^{m+1}(\vec{q}_\perp) & m < 0, \end{cases} \quad (B.3)$$

$$q^* \phi_n^m(\vec{q}_\perp) = b \begin{cases} \sqrt{n + |m| + 1} \phi_n^{m-1}(\vec{q}_\perp) - \sqrt{n} \phi_{n-1}^{m-1}(\vec{q}_\perp) & m \leq 0 \\ \sqrt{n + |m|} \phi_n^{m-1}(\vec{q}_\perp) - \sqrt{n+1} \phi_{n+1}^{m-1}(\vec{q}_\perp) & m > 0, \end{cases} \quad (B.4)$$

$$\vec{q}_\perp^2 \phi_n^m(\vec{q}_\perp) = b^2 \Big[(2n + |m| + 1) \phi_n^{m-1}(\vec{q}_\perp) - \sqrt{n(n + |m|)} \phi_{n-1}^m(\vec{q}_\perp) - \sqrt{(n+1)(n+1+|m|)} \phi_{n+1}^m(\vec{q}_\perp) \Big].$$

$$(B.5)$$

Then the matrix element reads

$$\langle n', m', l', s', \bar{s}'|V_g|n, m, l, s, \bar{s}\rangle =$$

$$- f\frac{\alpha_s}{\pi}\sqrt{\frac{l!l'!\Gamma(l+\alpha+\beta+1)\Gamma(l'+\alpha+\beta+1)}{\Gamma(l+\alpha+1)\Gamma(l+\beta+1)\Gamma(l'+\alpha+1)\Gamma(l'+\beta+1)}}\sqrt{(2l+\alpha+\beta+1)(2l'+\alpha+\beta+1)}$$

$$\times \delta_{m+s_1+s_2,m'+s_1'+s_2'}T\Big[\sim\sum_{n_1,n_2}\mathcal{M}_{NMN'(-M)}^{n_10n_20}\frac{1}{2}S(n,m,n'm')I_{n_1,l_1,n_2,l_2}\Big],$$

$$(B.6)$$

where

$$I_{n_1,l_1,n_2,l_2} = \int_0^1 dx_1\ x_1^{\alpha/2}(1-x_1)^{\beta/2}P_{l_1}^{(\alpha,\beta)}(2x_1-1)\int_0^1 dx_2\ x_2^{\alpha/2}(1-x_2)^{\beta/2}P_{l_2}^{(\alpha,\beta)}(2x_2-1)$$

$$\times N(x_1,x_2)\int_0^\infty d\rho_1 e^{-\rho_1}\int_0^\infty d\rho_2 e^{-\rho_2}\frac{L_{n_1}(2\rho_1)L_{n_2}(2\rho_2)}{c_1\rho_1+c_2\rho_2+\Delta/2}.$$

$$(B.7)$$

Notice that the first line in eqa.(3) is the essential normalization factor from the Jacobi polynomial. c_1, c_2 and Δ is defined as,

$$c_1 = \frac{1}{2}\left(\sqrt{x'(1-x)}-\sqrt{x(1-x')}\right)^2,$$

$$c_2 = \frac{1}{2}\left(\sqrt{x'(1-x)}+\sqrt{x(1-x')}\right)^2 \quad (c_1 < c_2);$$

$$\Delta = (x-x')^2\left(\frac{m_q^2}{xx'}+\frac{m_a^2}{(1-x)(1-x')}\right)/\kappa^2+2\mu_g^2/\kappa^2.$$

$$(B.8)$$

B.0.1 Spinor Part in One Gluon Exchange

There are ten kinds of prefactors, with different combinations of x_1 and x_2, list as follows

Notice that, even for unequal mass cases, we still have

$$I_{n_1,l_1,n_2,l_2}\left[N(x_2,x_1)\right] = I_{n_1,l_2,n_2,l_1}\left[N(x_1,x_2)\right] \tag{B.9}$$

where we have exchanged l_1 and l_2. Then we classify those integrands in terms of $q_\perp(q_\perp')$:

Type 1: transverse part, 1

$$T_1 = \delta_{mm'}\sum_\nu\mathcal{M}_{n,m,n',(-m)}^{\nu,0,\nu',0}\begin{cases}b:I_{\nu,l,\nu',l'}\left[\dfrac{m_q^2x_1x_2+m_a^2(1-x_1)(1-x_2)}{\sqrt{x_1x_2(1-x_1)(1-x_2)}}\right] & \text{①,②,③,④}\\[3ex]c:I_{\nu,l,\nu',l'}\left[\dfrac{m_qm_a(x_1-x_2)^2}{\sqrt{x_1x_2(1-x_1)(1-x_2)}}\right]\times(-1) & \text{⑬,⑭}\end{cases}$$

$$(B.10)$$

	s_1	s_2	s'_1	s'_2	$\frac{1}{2}\bar{u}_{s'_1}(p'_1)\gamma_\mu u_{s_1}(p_1)\bar{v}_{s_2}(p_2)\gamma^\mu v_{s'_2}(p'_2)$
①	$+$	$+$	$+$	$+$	$m_q^2\sqrt{\frac{(1-x)(1-x')}{xx'}} + m_a^2\sqrt{\frac{xx'}{(1-x)(1-x')}} + qq'^*$
②	$-$	$-$	$-$	$-$	$m_q^2\sqrt{\frac{(1-x)(1-x')}{xx'}} + m_a^2\sqrt{\frac{xx'}{(1-x)(1-x')}} + q^*q'$
③	$+$	$-$	$+$	$-$	$m_q^2\sqrt{\frac{(1-x)(1-x')}{xx'}} + m_a^2\sqrt{\frac{xx'}{(1-x)(1-x')}}$ $+qq'^*(1-x)(1-x') + q'q^*xx' + (\vec{q}_\perp^2 + \vec{q}_\perp'^2)\sqrt{xx'(1-x)(1-x')}$
④	$-$	$+$	$-$	$+$	$m_q^2\sqrt{\frac{(1-x)(1-x')}{xx'}} + m_a^2\sqrt{\frac{xx'}{(1-x)(1-x')}}$ $+q^*q'(1-x)(1-x') + qq'^*xx' + (\vec{q}_\perp^2 + \vec{q}_\perp'^2)\sqrt{xx'(1-x)(1-x')}$
⑤	$+$	$+$	$+$	$-$	$m_a x'\left(q'\sqrt{\frac{x}{1-x}} - q\sqrt{\frac{x'}{1-x'}}\right)$
⑥	$-$	$-$	$-$	$+$	$m_a x'\left(q^*\sqrt{\frac{x'}{1-x'}} - q'^*\sqrt{\frac{x}{1-x}}\right)$
⑦	$-$	$+$	$-$	$-$	$m_a x\left(q'\sqrt{\frac{x}{1-x}} - q\sqrt{\frac{x'}{1-x'}}\right)$
⑧	$+$	$-$	$+$	$+$	$m_a x\left(q^*\sqrt{\frac{x'}{1-x'}} - q'^*\sqrt{\frac{x}{1-x}}\right)$
⑨	$+$	$+$	$-$	$+$	$m_q(1-x')\left(q\sqrt{\frac{1-x'}{x'}} - q'\sqrt{\frac{1-x}{x}}\right)$
⑩	$-$	$-$	$+$	$-$	$m_q(1-x')\left(q'^*\sqrt{\frac{1-x}{x}} - q^*\sqrt{\frac{1-x'}{x'}}\right)$
⑪	$+$	$-$	$-$	$-$	$m_q(1-x)\left(q\sqrt{\frac{1-x'}{x'}} - q'\sqrt{\frac{1-x}{x}}\right)$
⑫	$-$	$+$	$+$	$+$	$m_q(1-x)\left(q'^*\sqrt{\frac{1-x}{x}} - q^*\sqrt{\frac{1-x'}{x'}}\right)$
⑬	$+$	$-$	$-$	$+$	$m_q m_a \frac{-(x-x')^2}{\sqrt{x(1-x)x'(1-x')}}$
⑭	$-$	$+$	$+$	$-$	$m_q m_a \frac{-(x-x')^2}{\sqrt{x(1-x)x'(1-x')}}$
⑮	$+$	$+$	$-$	$-$	0
⑯	$-$	$-$	$+$	$+$	0

Table B.1: The spinor part $\bar{u}_{s'}(p'_1)\gamma_\mu u_s(p_1)\bar{v}_{\bar{s}}(p_2)\gamma^\mu v_{\bar{s}'}(p'_2)$, with $m_q^2 = p_1^2 = p_1'^2$ is the mass of quark and $m_a^2 = p_2^2 = p_2'^2$ is the mass of anti-quark. We expressed them in terms of the holographic momentum $q = \vec{p}_\perp/\sqrt{x(1-x)}$. $q = q_x + iq_y$ and $q^* = q_x - iq_y$ are the complex representation of $\vec{q} = q_x\vec{e}_x + q_y\vec{e}_y$.

	$N(x_1, x_2)$	spinor part
(a)	1	①, ②
(b)	$(x_1 x_2 + (1-x_1)(1-x_2))/\sqrt{x_1 x_2 (1-x_1)(1-x_2)}$	①, ②, ③, ④
(c)	$(x_1 - x_2)^2/\sqrt{x_1 x_2 (1-x_1)(1-x_2)}$	⑬, ⑭
(d)	$\sqrt{x_1 x_2 (1-x_1)(1-x_2)}$	③, ④
(e)	$x_1 x_2$	③, ④
(f)	$(1-x_1)(1-x_2)$	③, ④
(g)	$x_1\sqrt{x_1/(1-x_1)}$	⑤ − ⑧
(h)	$x_1\sqrt{x_2/(1-x_2)}$	⑤ − ⑧
(i)	$(1-x_1)\sqrt{(1-x_1)/x_1}$	⑨ − ⑫
(j)	$(1-x_1)\sqrt{(1-x_2)/x_2}$	⑨ − ⑫

Table B.2

Type 2: transverse part, qq'^*

$$T_2 = \kappa^2 \delta_{mm'} \times \sum_{\nu}$$

$$
\begin{cases}
\begin{aligned}
&\sqrt{(n+|m|+1)(n'+|m|+1)}\mathcal{M}^{\nu,0,\nu',0}_{n,m+1,n',-m-1} + \sqrt{nn'}\mathcal{M}^{\nu,0,\nu',0}_{n-1,m+1,n'-1,-m-1}\\
&- \sqrt{(n+|m|+1)n'}\mathcal{M}^{\nu,0,\nu',0}_{n,m+1,n'-1,-m-1} - \sqrt{n(n'+|m|+1)}\mathcal{M}^{\nu,0,\nu',0}_{n-1,m+1,n',-m-1} \quad m \geq 0
\end{aligned}\\[2em]
\begin{aligned}
&\sqrt{(n+|m|)(n'+|m|)}\mathcal{M}^{\nu,0,\nu',0}_{n,m+1,n',-m-1} + \sqrt{(n+1)(n'+1)}\mathcal{M}^{\nu,0,\nu',0}_{n+1,m+1,n'+1,-m-1}\\
&- \sqrt{(n+|m|)(n'+1)}\mathcal{M}^{\nu,0,\nu',0}_{n,m+1,n'+1,-m-1} - \sqrt{(n+1)(n'+|m|)}\mathcal{M}^{\nu,0,\nu',0}_{n+1,m+1,n',-m-1} \quad m < 0
\end{aligned}
\end{cases}
$$

$$
\times
\begin{cases}
a : I_{\nu,l,\nu',l'}[1] & ①\\
f : I_{\nu,l,\nu',l'}[(1-x_1)(1-x_2)] & ③\\
e : I_{\nu,l,\nu',l'}[x_1 x_2] & ④
\end{cases}
$$

$$(B.11)$$

104

Type 3: transverse part, q^*q'

$$T_3 = \kappa^2 \delta_{mm'} \times \sum_\nu$$

$$\left\{ \begin{array}{l} \sqrt{(n+|m|+1)(n'+|m|+1)}\mathcal{M}_{n,m-1,n',1-m}^{\nu,0,\nu',0} + \sqrt{nn'}\mathcal{M}_{n-1,m-1,n'-1,1-m}^{\nu,0,\nu',0} \\[2mm] - \sqrt{(n+|m|+1)n'}\mathcal{M}_{n,m-1,n'-1,1-m}^{\nu,0,\nu',0} - \sqrt{n(n'+|m|+1)}\mathcal{M}_{n-1,m-1,n',1-m}^{\nu,0,\nu',0} \qquad m \leq 0 \\[4mm] \sqrt{(n+|m|)(n'+|m|)}\mathcal{M}_{n,m-1,n',1-m}^{\nu,0,\nu',0} + \sqrt{(n+1)(n'+1)}\mathcal{M}_{n+1,m-1,n'+1,1-m}^{\nu,0,\nu',0} \\[2mm] - \sqrt{(n+|m|)(n'+1)}\mathcal{M}_{n,m-1,n'+1,1-m}^{\nu,0,\nu',0} - \sqrt{(n+1)(n'+|m|)}\mathcal{M}_{n+1,m-1,n',1-m}^{\nu,0,\nu',0} \qquad m > 0 \end{array} \right\}$$

$$\times \begin{cases} a : I_{\nu,l,\nu',l'}[1] & \textcircled{2} \\[2mm] e : I_{\nu,l,\nu',l'}[x_1 x_2] & \textcircled{3} \\[2mm] f : I_{\nu,l,\nu',l'}[(1-x_1)(1-x_2)] & \textcircled{4} \end{cases}$$

$$(B.12)$$

Type 4: transverse part, $\vec{q}_\perp^2 + \vec{q}_\perp'^2$

$$T_4 = \kappa^2 \delta_{mm'} \sum_\nu \left(2(n+n'+|m|+1)\mathcal{M}_{n,m,n',-m}^{\nu,0,\nu',0} - \sqrt{n(n+|m|)}\mathcal{M}_{n-1,m,n',-m}^{\nu,0,\nu',0} - \sqrt{n'(n'+|m|)}\mathcal{M}_{n,m,n'-1,-m}^{\nu,0,\nu',0} \right.$$

$$\left. - \sqrt{(n+1)(n+|m|+1)}\mathcal{M}_{n+1,m,n',-m}^{\nu,0,\nu',0} - \sqrt{(n'+1)(n'+|m|+1)}\mathcal{M}_{n,m,n'+1,-m}^{\nu,0,\nu',0} \right)$$

$$\times I_{\nu,l,\nu',l'}[\sqrt{xx'(1-x)(1-x')}] \qquad \textcircled{3}, \textcircled{4}$$

$$(B.13)$$

Type 5: transverse part, q

$$T_5 = -\kappa\delta_{m+1,m'} \sum_\nu \begin{cases} \sqrt{n+|m|+1}\,\mathcal{M}^{\nu,0,\nu',0}_{n,m+1,n',-m-1} - \sqrt{n}\,\mathcal{M}^{\nu,0,\nu',0}_{n-1,m+1,n',-m-1} & m \geq 0 \\ \sqrt{n+|m|}\,\mathcal{M}^{\nu,0,\nu',0}_{n,m+1,n',-m-1} - \sqrt{n+1}\,\mathcal{M}^{\nu,0,\nu',0}_{n+1,m+1,n'+1,-m-1} & m < 0 \end{cases}$$

$$\times \begin{cases} g: m_a I_{\nu,l',\nu',l}\left[x_1\sqrt{x_1/(1-x_1)}\right] & \text{⑤} \\ h: m_a I_{\nu,l,\nu',l'}\left[x_1\sqrt{x_2/(1-x_2)}\right] & \text{⑦} \\ i: m_q I_{\nu,l',\nu',l}\left[(1-x_1)\sqrt{(1-x_1)/x_1}\right] & \text{⑨} \\ j: m_q I_{\nu,l,\nu',l'}\left[(1-x_1)\sqrt{(1-x_2)/x_2}\right] & \text{⑪} \end{cases}$$

$$(\text{B.14})$$

Type 6: transverse part, q'

$$T_6 = \kappa\delta_{m+1,m'} \sum_\nu \begin{cases} \sqrt{n'+|m|+1}\,\mathcal{M}^{\nu,0,\nu',0}_{n,m,n',-m} - \sqrt{n'+1}\,\mathcal{M}^{\nu,0,\nu',0}_{n,m,n'+1,-m} & m \geq 0 \\ \sqrt{n'+|m|}\,\mathcal{M}^{\nu,0,\nu',0}_{n,m,n',-m} - \sqrt{n'}\,\mathcal{M}^{\nu,0,\nu',0}_{n,m,n'-1,-m} & m < 0 \end{cases}$$

$$\times \begin{cases} h: m_a I_{\nu,l',\nu',l}\left[x_1\sqrt{x_2/(1-x_2)}\right] & \text{⑤} \\ g: m_a I_{\nu,l,\nu',l'}\left[x_1\sqrt{x_1/(1-x_1)}\right] & \text{⑦} \\ j: m_q I_{\nu,l',\nu',l}\left[(1-x_1)\sqrt{(1-x_2)/x_2}\right] & \text{⑨} \\ i: m_q I_{\nu,l,\nu',l'}\left[(1-x_1)\sqrt{(1-x_1)/x_1}\right] & \text{⑪} \end{cases}$$

$$(\text{B.15})$$

Type 7: transverse part, q^*

$$T_7 = \kappa\delta_{m-1,m'} \sum_\nu \begin{cases} \sqrt{n+|m|+1}\,\mathcal{M}^{\nu,0,\nu',0}_{n,m-1,n',1-m} - \sqrt{n}\,\mathcal{M}^{\nu,0,\nu',0}_{n-1,m-1,n',1-m} & m \leq 0 \\ \sqrt{n+|m|}\,\mathcal{M}^{\nu,0,\nu',0}_{n,m-1,n',1-m} - \sqrt{n+1}\,\mathcal{M}^{\nu,0,\nu',0}_{n+1,m-1,n',1-m} & m > 0 \end{cases}$$

$$\times \begin{cases} g: m_a I_{\nu,l',\nu',l}\left[x_1\sqrt{x_1/(1-x_1)}\right] & \text{⑥} \\ h: m_a I_{\nu,l,\nu',l'}\left[x_1\sqrt{x_2/(1-x_2)}\right] & \text{⑧} \\ i: m_q I_{\nu,l',\nu',l}\left[(1-x_1)\sqrt{(1-x_1)/x_1}\right] & \text{⑩} \\ j: m_q I_{\nu,l,\nu',l'}\left[(1-x_1)\sqrt{(1-x_2)/x_2}\right] & \text{⑫} \end{cases}$$

$$(\text{B.16})$$

Type 8: transverse part, q'^*

$$T_8 = -\kappa \delta_{m-1,m'} \sum_\nu \left\{ \begin{array}{ll} \sqrt{n'+|m|+1}\mathcal{M}_{n,m,n',-m}^{\nu,0,\nu',0} - \sqrt{n'+1}\mathcal{M}_{n,m,n'+1,-m}^{\nu,0,\nu',0} & m \leq 0 \\ \sqrt{n'+|m|}\mathcal{M}_{n,m,n',-m}^{\nu,0,\nu',0} - \sqrt{n'}\mathcal{M}_{n,m,n'-1,-m}^{\nu,0,\nu',0} & m > 0 \end{array} \right\}$$

$$\times \left\{ \begin{array}{ll} h : m_a I_{\nu,l',\nu',l}\left[x_1\sqrt{x_2/(1-x_2)}\right] & \text{⑥} \\ g : m_a I_{\nu,l,\nu',l'}\left[x_1\sqrt{x_1/(1-x_1)}\right] & \text{⑧} \\ j : m_q I_{\nu,l',\nu',l}\left[(1-x_1)\sqrt{(1-x_2)/x_2}\right] & \text{⑩} \\ i : m_q I_{\nu,l,\nu',l'}\left[(1-x_1)\sqrt{(1-x_1)/x_1}\right] & \text{⑫} \end{array} \right.$$

$$(B.17)$$

APPENDIX C.   TALMI-MOSHINSKY TRANSFORMATION

When deal with the weak decay problem, one needs to work with different HO basis scale b's, as well as the longitudinal frame integral. Therefore, the Talmi-Moshinsky (TM) transform requires a nontrivial and careful derivation.

Starting with the generic expression of HO basis function,

$$\phi_{nm}(\vec{q}_\perp; b) = \frac{1}{b}\sqrt{\frac{4\pi n!}{(n+|m|)!}}\left(\frac{q_\perp}{b}\right)^{|m|}\exp\left(-q_\perp^2/(2b^2)\right)L_n^{|m|}(q_\perp^2/b^2)\exp(im\theta_q), \tag{C.1}$$

where $b = \sqrt{\hbar M_{\text{HO}}\Omega_{\text{HO}}}$ is the basis energy scale. When integrate the transverse part, we have

$$\int \frac{\mathrm{d}^2[k_\perp/\sqrt{x(1-x)}]}{(2\pi)^2}\phi_{n_1 m_1}\left(\frac{\vec{k}_\perp}{\sqrt{x(1-x)}}; b_1\right)\phi_{n_2 m_2}^*\left(\frac{\vec{k}_\perp + x\vec{q}_\perp}{\sqrt{x(1-x)}}; b_2\right)$$
$$= \int \frac{\mathrm{d}^2[k_\perp/\sqrt{x(1-x)}]}{(2\pi)^2}\sum_{N,M,n,m}\mathcal{M}_{n_1,m_1,n_2,-m_2}^{N,M,n,m}(\delta)\phi_{NM}(Q;B)\phi_{nm}(q;b) \tag{C.2}$$

The relation between the Jacobi variables and the single-particle variables are

$$\begin{pmatrix}\bar{Q}\\ \bar{q}\end{pmatrix} = \begin{pmatrix}\cos\delta & \sin\delta\\ \sin\delta & -\cos\delta\end{pmatrix}\begin{pmatrix}\bar{q}_1\\ \bar{q}_2\end{pmatrix} \tag{C.3}$$

where $\bar{Q} = Q/B, \bar{q} = q/b, \bar{q}_1 = q_1/b_1, \bar{q}_2 = q_2/b_2$. Therefore, $\tan\delta = \frac{b_1}{b_2}$,

$$\bar{Q} = \frac{k_\perp}{\sqrt{x(1-x)}}\frac{\sqrt{b_1^2+b_2^2}}{b_1 \cdot b_2} + \frac{b_1}{b_2\sqrt{b_1^2+b_2^2}}\sqrt{\frac{x}{1-x}}q_\perp, \quad \bar{q} = -\sqrt{\frac{x}{1-x}}q_\perp/\sqrt{b_1^2+b_2^2}, \tag{C.4}$$

with

$$B = \frac{b_1 \cdot b_2}{\sqrt{b_1^2+b_2^2}}, \quad b = \sqrt{b_1^2+b_2^2}. \tag{C.5}$$

Then the integral becomes,

$$= \frac{B}{\sqrt{\pi}}\sum_{N,M,n,m}\mathcal{M}_{n_1,m_1,n_2,-m_2}^{N,M=0,n,m}(\delta)(-1)^N\phi_{nm}\left(\sqrt{\frac{x}{1-x}}q_\perp; \sqrt{b_1^2+b_2^2}\right)$$
$$= \frac{2b_1 b_2}{b_1^2+b_2^2}\sum_{N,M,n,m}\mathcal{M}_{n_1,m_1,n_2,-m_2}^{N,M=0,n,m}(\delta)(-1)^N\sqrt{\frac{n!}{(n+|m|)!}}\bar{q}^{|m|}\exp(-\bar{q}^2/2)L_n^{|m|}(\bar{q}^2)\exp(im\theta). \tag{C.6}$$

C.0.1 Transverse Integral

Type 1: 1

$$\mathbb{I}_1 = \frac{1}{x(1-x)} \int \frac{\mathrm{d}^2 k_\perp}{(2\pi)^2} \phi_{n_2 m_2}^* \left(\frac{\vec{k}_\perp(1-z) - (1-x)\vec{\Delta}_\perp}{\sqrt{(x-z)(1-x)}}; b_2 \right) \phi_{n_1 m_1} \left(\frac{\vec{k}_\perp}{\sqrt{x(1-x)}}; b_1 \right)$$
$$= \int \frac{\mathrm{d}^2 k_\perp}{(2\pi)^2} \phi_{n_1 m_1} \left(\vec{k}_\perp; b_1 \right) \phi_{n_2 m_2}^* \left(\vec{k}_\perp - \sqrt{\frac{1-x}{z}} \frac{\vec{\Delta}_\perp}{1-z}; b_2' \right) \tag{C.7}$$

where $b_2' = b_2 \sqrt{\frac{x-z}{x}}/(1-z)$. Performing the TM transformation, one obtains:

$$\mathbb{I}_1 = \frac{2b_1 b_2'}{b_1^2 + b_2'^2} \sum_{N,M,n,m} \mathcal{M}_{n_1,m_1,n_2,-m_2}^{N,M=0,n,m}(\delta)(-1)^N \sqrt{\frac{n!}{(n+|m|)!}} \bar{q}^{|m|} \exp\left(-\bar{q}^2/2\right) L_n^{|m|}(\bar{q}^2) \exp\left(im\theta\right) \tag{C.8}$$

with $\bar{q} = \sqrt{\frac{1-x}{x}} \frac{\vec{\Delta}_\perp}{1-z}/\sqrt{b_2^2 + b_2'^2}$.

Type 2: k^R

$$\mathbb{I}_2 = \frac{1}{x(1-x)} \int \frac{\mathrm{d}^2 k_\perp}{(2\pi)^2} \phi_{n_2 m_2}^* \left(\frac{\vec{k}_\perp - \left(\frac{1-x}{1-z}\right)\vec{\Delta}_\perp}{\sqrt{(x-z)(1-x)/(1-z)}}; b_2 \right) \phi_{n_1 m_1} \left(\frac{\vec{k}_\perp}{\sqrt{x(1-x)}}; b_1 \right) \cdot k^R$$

$$= \sqrt{x(1-x)} \int \frac{\mathrm{d}^2 k_\perp}{(2\pi)^2} \phi_{n_1 m_1}(\vec{k}_\perp; b_1) \phi_{n_2 m_2}^*(\vec{k}_\perp; b_2') \cdot k^R$$

$$= \sqrt{x(1-x)} \frac{(2b_1 b_2')^2}{(b_1^2 + b_2'^2)^{3/2}} \sum_{N,M,n,m} \mathcal{M}_{n_1,m_1,n_2,-m_2}^{N,M=-1,n,m}(\delta)(-1)^N \sqrt{N+1}$$

$$\times \sqrt{\frac{n!}{(n+|m|)!}} \bar{q}^{|m|} \exp\left(-\bar{q}^2/2\right) L_n^{|m|}(\bar{q}^2) \exp(im\theta) \tag{C.9}$$

APPENDIX D.   GAUSS QUADRATURE RULES

We often encounter numerical integration in our work. Sometimes the complicated integral can be factored into a summation of terms which are multiplication of "weight" and function value. To be more specific, we have

$$\int_a^b w(x)f(x)\mathrm{d}x \approx \sum_{j=1}^N w_j f(t_j). \tag{D.1}$$

We will state the theorem in more detail without giving a proof.

Let nonzero function $w(x) \geq 0$ be a fixed "weight" function defined on the range $[a, b]$. We are able to define a sequence of orthonormal polynomials $p_0(x), p_1(x), \ldots$ with respect to the weight function, whose degrees are coincident with the subscript, in the sense that

$$\int_a^b w(x)p_m(x)p_n(x)\mathrm{d}x = \delta_{mn}. \tag{D.2}$$

The polynomials could be determined degree by degree, and they are uniquely fixed. One could verify that the polynomial $p_n(x) = k_n \prod_{i=1}^n (x - t_i)$ has n real roots $a < t_1 < \cdots < t_n < b$. With those polynomials and the corresponding roots defined, we are able to express the Gaussian quadrature rule: Let $f(x)$ be smooth function in $[a, b]$, then

$$\int_a^b w(x)f(x)\mathrm{d}x = \sum_{j=1}^N w_j f(t_j) + \frac{f^{(2N)}(\xi)}{(2N)!k_N^2}, \ (a < \xi < b), \tag{D.3}$$

where $w_j = -\frac{k_{N+1}}{k_N p_{N+1}(t_j)p_N'(t_j)}$. It follows directly that the Gauss quadrature is exact for all polynomials of degree $\leq 2N - 1$.

Some common weights get their own names, the case $w(x) = 1$ is called Gauss-Legendre quadrature, the case $w(x) = \sqrt{1 - x^2}$ is called Chebyshev-Guess quadrature. They are all special cases of Gauss Jacobi quadrature, in which $w(x) = (1 - x)^\alpha (1 + x)^\beta$.

APPENDIX E.   SPECIAL POLYNOMIALS

In this section we collect some basic properties of the special functions we used in our model. Namely they are generalized Laguerre polynomials and Jacobi polynomials.

The generalized Laguerre polynomials $L_n^{(\alpha)}(x)$ are a class of orthogonal polynomials relative to the weight $x^\alpha e^{-x}$ on the interval $[0, +\infty)$, which satisfy

$$\int_0^\infty x^\alpha e^{-x} L_n^{(\alpha)}(x) L_m^{(\alpha)}(x) \mathrm{d}x = \frac{(n+\alpha)!}{n!} \delta_{mn}, \tag{E.1}$$

where $L_n^{(\alpha)}(x)$ has the close form

$$L_n^{(\alpha)}(x) = \sum_{i=0}^{n} (-1)^i \binom{n+\alpha}{n-i} \frac{x^i}{i!}. \tag{E.2}$$

The generalized Laguerre polynomials are the radial solutions for the transverse of the effective Hamiltonian.

The Jacobi polynomials $J_n^{\alpha,\beta}(x)$ are a class of orthogonal polynomials relative to the weight $(1-x)^\alpha (1+x)^\beta$ on the interval $[-1, 1]$. The Jacobi polynomials $J_n^{\alpha,\beta}(x)$ can be expressed as

$$J_n^{\alpha,\beta}(x) = \frac{1}{2^n} \sum_{k=0}^{n} \binom{n+\alpha}{k} \binom{n+\beta}{n-k} (x-1)^{n-k} (x+1)^k. \tag{E.3}$$

They are the solution of the linear operator

$$\begin{aligned}
L_{\alpha,\beta} &= -(1-x)^\alpha (1+x)^\beta \frac{\mathrm{d}}{\mathrm{d}x} \left((1-x)^{\alpha+1} (1+x)^{\beta+1} \frac{\mathrm{d}}{\mathrm{d}x} \right) \\
&= (x^2-1) \frac{\mathrm{d}^2}{\mathrm{d}x^2} + [(\alpha+\beta+2)x + \alpha-\beta] \frac{\mathrm{d}}{\mathrm{d}x},
\end{aligned} \tag{E.4}$$

with corresponding eigenvalues

$$L_{\alpha,\beta} J_n^{\alpha,\beta}(x) = \lambda_n^{\alpha,\beta} J_n^{\alpha,\beta}(x), \quad \lambda^{\alpha,\beta} = n(n+\alpha+\beta+1). \tag{E.5}$$

The longitudinal basis functions are defined in terms of Jacobi polynomials as $\chi_n^{\alpha,\beta}(x) = C_l(1-x)^{\frac{\alpha}{2}} x^{\frac{\beta}{2}} J_n^{\alpha,\beta}(x)$ where C_l is the normalization factor. The Jacobi polynomials satisfy

$$\begin{aligned}
&-\frac{\mathrm{d}}{\mathrm{d}x} \left(x(1-x) \frac{\mathrm{d}}{\mathrm{d}x} \chi_n^{\alpha,\beta}(x) \right) + \frac{1}{4} \left(\frac{\beta^2}{x} + \frac{\alpha^2}{1-x} \right) \chi_n^{\alpha,\beta}(x) \\
&= \left(n + \frac{1}{2}(\alpha+\beta) \right) \left(n + \frac{1}{2}(\alpha+\beta) + 1 \right) \chi_n^{\alpha,\beta}(x).
\end{aligned} \tag{E.6}$$

To find the eigenfunctions of the operator $-\gamma^2 \frac{\mathrm{d}}{\mathrm{d}x}\left(x\left(1-x\right)\frac{\mathrm{d}}{\mathrm{d}x}\right) + \left(\beta^2/x + \alpha^2/(1-x)\right)$, a change of variable will do and the solutions are

$$\left(x^{\frac{\beta}{\gamma}}\left(1-x\right)^{\frac{\alpha}{\gamma}}\right) J_n^{\frac{2\alpha}{\gamma},\frac{2\beta}{\gamma}}\left(2x-1\right), \tag{E.7}$$

with corresponding eigenvalues $(n\gamma + \alpha + \beta)\left((n+1)\gamma + \alpha + \beta\right)$.